A turbulent story:

role of diapycnal mixing in the ocean overturning circulation and tracer distribution



Laura Cimoli

Hertford College

University of Oxford

Trinity 2019

A thesis submitted for the degree of

Doctor of Philosophy

Acknowledgements

Thanks, first of all, to Ali. It has not been an easy journey, and I would have not walked this far it without your help. Thanks for stirring my enthusiasm and helping me finding my way. And thanks for walking next to me, sweetening the road under my steps.

I wish to thank my supervisors, David Marshall and Helen Johnson, for their guidance and support throughout my DPhil. Thanks for allowing me great freedom to explore, and for gently and patiently helping me to stay on track.

Thanks to the many collaborators that enriched my research experience, in particular to Matthew Alford and Lynne Talley for hosting me at SIO over several visits and to Alberto Naveira Garabato for many in depth discussions (and jokes). I'd also like to thank Laure Zanna and Andrew Wells for examining my transfer and confirmation reports.

I would like to thank the Clarendon Fund for providing financial support during my studies.

Thanks to all the friends, both near and far, who have helped me along the way. Thanks for adding fun to this adventure and creating sweet memories.

Finally, I am extremely grateful to my parents, for their support is the sweetest. Thanks for your constant encouragement and love.

A turbulent story: role of diapycnal mixing in the ocean overturning circulation and tracer distribution.

Laura Cimoli
Hertford College

Trinity 2019

A thesis submitted for the degree of *Doctor of Philosophy*

Abstract

Natural and anthropogenic heat and carbon, as well as other climatically and biologically important tracers, enter the deep global overturning circulation mainly during the formation of dense waters at the high latitudes around Antarctica and in the North Atlantic. Through the transport, sequestration and upwelling of tracers, the global overturning circulation contributes to the regulation and variability of our climate system.

This thesis investigates the role of diapycnal (cross-density) mixing in regulating the deep ocean overturning circulation and the distribution of tracers carried within it. Diapycnal mixing is here quantified through a combination of pre-existing estimates inferred from different observational sources, namely Argo floats, CTD casts combined with microstructure profiles, bulk estimates from an inverse model and observation-based theoretical estimates of the mixing generated by internal tides and lee waves. Firstly, it is shown that the upwelling of abyssal waters is the residual of large near-boundary upwelling and interior downwelling, the patterns of which are highly sensitive to the specifics of the energy pathways from tides and geostrophic motions to internal waves and thereafter to mixing and dissipation. Secondly, we focus on the Atlantic Ocean, where we investigate the role of mixing in the closure of the Atlantic meridional overturning circulation. Diapycnal mixing is shown to contribute only marginally to the conversion of the dense waters formed in the North Atlantic into lighter northward-flowing waters within the Atlantic basin, but it plays a crucial role in the distribution of tracers carried from the North Atlantic to the Southern Ocean. The impact of mixing on tracer distributions is analysed both from observational mixing estimates and from pre-existing numerical simulations of a tracer release experiment in a quasi-realistic Atlantic sector model. As a tracer is carried southward by the Atlantic overturning circulation, we quantify its exchange between different water masses. The tracer transport and exchange rates are key in determining in which density classes tracers are going to upwell in the Southern Ocean, therefore determining which pathway they will follow in the global overturning circulation.

Contents

1 Introduction **1**

1.1 The Global Meridional Overturning Circulation 1

1.2 Role of diapycnal mixing in the MOC 6

1.2.1 Lower cell 6

1.2.2 Upper cell 8

1.2.3 Ocean overturning and stratification scaling relations 9

1.3 Thesis questions 14

1.4 Thesis structure 16

2 Diapycnal mixing: definition and sources **17**

2.1 Diapycnal mixing definition 17

2.2 Diapycnal mixing sources 26

2.2.1 Internal tides 27

2.2.2 Geostrophic flow over topography 28

2.2.3 Near-inertial waves 28

2.2.4 Other sources 29

3 Mixing sensitivity to internal wave local breaking and mixing efficiencies **31**

3.1 Internal waves: energy and radiation 36

3.1.1 Internal wave energy 36

3.1.2 Internal wave radiation 37

3.2 From internal wave breaking to irreversible mixing 39

3.2.1 Energy from locally breaking internal waves 39

3.2.2 A parameterisation for the flux coefficient 40

3.2.3 Inferring mixing 43

3.3 Internal wave local breaking efficiency and flux coefficient co-variation: effects on diapycnal mixing 45

3.3.1 Contribution of different mixing-generating processes 54
3.3.2 A brief comment on the contribution of near-inertial waves 58
3.4 Summary and conclusions 61

4 Observation-based estimates of mixing in the Atlantic Ocean 67
4.1 Mixing estimates 71
4.1.1 Estimates of diapycnal mixing based on Argo 72
4.1.2 Estimates of bottom-generated diapycnal mixing 74
4.1.3 Estimates of diapycnal mixing based on CTD data 75
4.1.4 Bulk estimates of basin-scale diapycnal mixing 77
4.2 Diapycnal water mass transformation in the Atlantic Ocean 78
4.3 Diffusive tracer transport in the Atlantic Ocean 83
4.4 Summary and conclusions 86

5 A numerical study of tracer mixing in the Atlantic Ocean 91
5.1 A three-dimensional Atlantic sector model 93
5.2 Tracer mixing in the Atlantic Ocean 96
5.3 Tracer upwelling in the Southern Ocean 111
5.4 Summary and conclusions 113

6 Conclusions 117

References 123

Chapter 1

Introduction

The ocean circulation plays a crucial role in the regulation, variability and anthropogenic change of our climate system through the sequestration, transport and release of heat and other climatically important tracers, such as carbon and oxygen. In particular, it is the formation and subduction of dense waters that determine the capacity of the ocean to store heat, freshwater and carbon: dense waters take up tracers while in contact with the atmosphere in the high latitudes and can store them in the deep ocean with timescales of hundreds of years (Talley *et al.*, 2011; Bullister *et al.*, 2013). A good understanding of the mechanisms that govern the deep ocean overturning circulation is, therefore, crucial to understand the present climate and to have a better prediction of future climate scenarios. This thesis aims to investigate the role of cross-density (diapycnal) mixing in regulating the deep ocean overturning circulation, in particular in the Atlantic Ocean, and the distribution of tracers carried within it.

1.1 The Global Meridional Overturning Circulation

Knowledge of the existence of a global deep ocean circulation goes back to the early days of ocean exploration when it was found that the deep ocean is cold even at tropical latitudes,

indicating that such deep waters had been supplied from polar regions (Stocker, 2013). Indeed, it is now well known that dense water masses, with distinct sea-water properties, form in few, localised areas in the high latitudes (Marshall & Schott, 1999; Talley, 2013). Such water masses form a complex system of circulation cells flowing across the different ocean basins and at various depths, giving birth to the global Meridional Overturning Circulation (MOC). A schematic representation of the global MOC is given in figure 1.1, where the colours of the arrows indicate their buoyancy (lighter waters in red, denser waters in blue).

In particular, there are two primary overturning cells in the global MOC, the so-called "upper" and "lower" cells. The upper cell begins in the North Atlantic, where dense waters are formed in different locations (Labrador and Nordic Seas), and create a southward flow known as North Atlantic Deep Water (NADW). Once in the Southern Ocean, the NADW finds its way back to the surface through wind-driven upwelling: the westerly winds blowing over the Southern Ocean generate a northward Ekman transport, which acts to pull dense water to the surface. Here, NADW upwells mainly in a region of negative buoyancy flux, i.e. an area where water becomes denser due to cooling (negative heat flux) or increase in salinity (negative freshwater flux). Thus, once at the surface, NADW is mainly transformed into denser water: it becomes the source for dense water formation around Antarctica (Talley *et al.*, 2011; Marshall & Speer, 2012; Talley, 2013), while only a minor fraction returns to the North Atlantic to feed the formation of new NADW. The closure of the upper cell requires a description of the pathways of the lower cell and the inter-basin connection between the two cells.

The lower cell consists of the densest water in our oceans: sourced by NADW, waters are transformed at the surface in the marginal seas around Antarctica into fresher but significantly colder water. The resulting water mass, known as Antarctic Bottom Water (AABW), moves northward into the Atlantic, Indian and Pacific Oceans, while being strongly constrained by the bottom topography. In all three ocean basins, AABW upwells into the local deep water through diapycnal mixing with the overlying waters of lighter density (Munk,

1966; Munk & Wunsch, 1998). Given that there is no dense water formation in the Pacific and Indian Oceans, AABW is the primary source of Pacific Deep Water (PDW) and Indian Deep Water (IDW), but it is only a minor source of NADW, which is mainly being formed at the surface in the North Atlantic (Talley *et al.*, 2011; Talley, 2013).

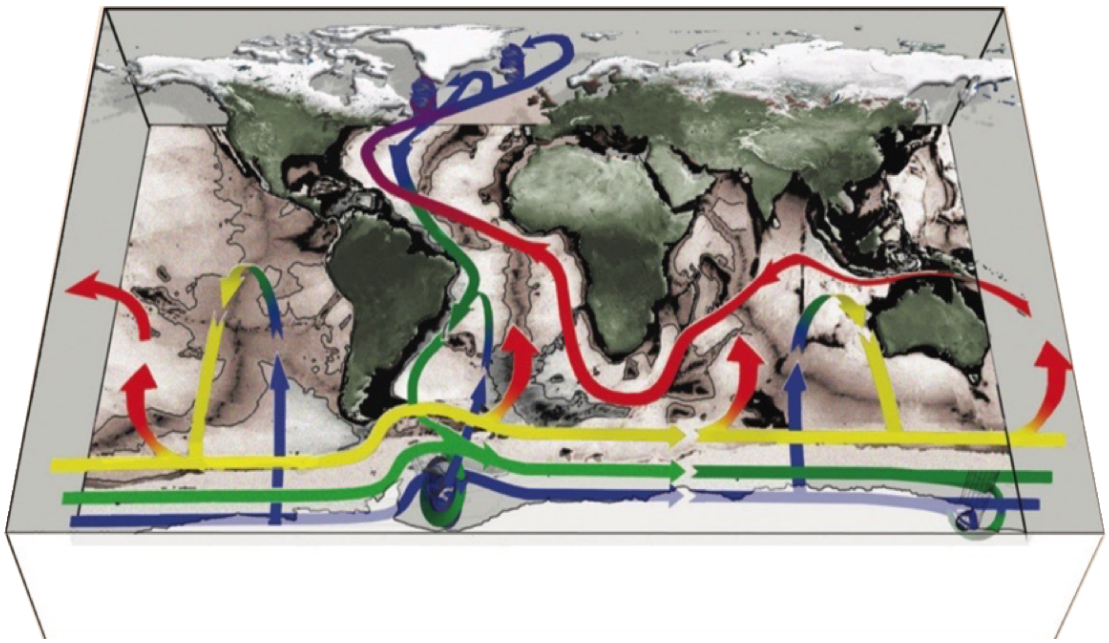


Figure 1.1: *A schematic representation of the global MOC. Colours indicate the density of water masses, ranging from the warmer mode and thermocline waters in red to bottom waters in blue. In the northern North Atlantic, dense water is formed by convection in the polar seas and Labrador Sea (blue arrows). Such dense waters flow southward in the deep branch of the upper cell (green arrow), before re-surfacing in the Southern Ocean. Here, waters are transformed either into the densest Antarctic Bottom Water (blue arrows), flowing northward in all the ocean basins, or into the lighter intermediate waters (yellow-red arrows) that contribute to the closure of the upper cell. Figure from Marshall & Speer (2012).*

The upper and lower cells are connected through direct interaction in the Atlantic Ocean (where the lower cell contributes to feeding the upper cell), and indirectly through PDW and IDW. These two deep water masses, fed by the mixing of AABW with the lighter waters above, flow southward and upwell in the Southern Ocean. Here, being less dense than NADW, they upwell further north in a region of positive buoyancy flux where they are transformed into lighter waters and become the dominant source of upper ocean waters

that leave the Southern Ocean via Ekman transport. Hence, these water masses feed the northward flow of light waters that return to the North Atlantic, closing the loop of the upper cell (Talley *et al.*, 2011; Talley, 2013).

Figure 1.2 shows an estimate of the global overturning streamfunction, i.e. the zonal and vertical integral of the meridional velocity (measured in Sverdrups, where 1 Sv = 10^6 m^3 s^{-1}), from the inverse model of Lumpkin & Speer (2007). The overturning streamfunction clearly shows the two main cells of the MOC: an upper cell (red), with a deep branch flowing from the North Atlantic to the Southern Ocean and a returning northward flow at shallower depths, and a lower cell (blue), flowing northward from the Southern Ocean and returning southward after being transformed into lighter waters through diapycnal mixing. What this figure does not show is the different basin location of the two cells: the upper cell is mainly housed in the Atlantic Ocean (as described above and shown in the schematic of figure 1.1), while the lower cell flows in all the ocean basins, and in particular in the Indian and Pacific Oceans. For plots of the overturning streamfunction in each basin see Lumpkin & Speer (2007).

The deep global circulation described above is regulated by a combination of several processes, of which the primary ones are: (i) wind-stress acting at the surface of the ocean in the Southern Ocean: the northward Ekman transport generated by the westerly winds blowing over the Southern Ocean is balanced by the upwelling of waters from the deep ocean, thus raising dense waters all the way to the surface (Toggweiler & Samuels, 1998); (ii) buoyancy forcing, through the role played by the atmosphere and the ice-shelves in controlling the positive/negative buoyancy fluxes that drive the transformation of water masses into either lighter or denser waters at the surface of the ocean; (iii) diapycnal mixing, which leads to the transformation of water masses in the ocean interior through the turbulence generated by internal waves. Such mechanisms control how dense water masses are formed and how they come back into contact with the atmosphere. Consequently, these mechanisms impact the distribution of tracers carried by dense water masses, determining (i)

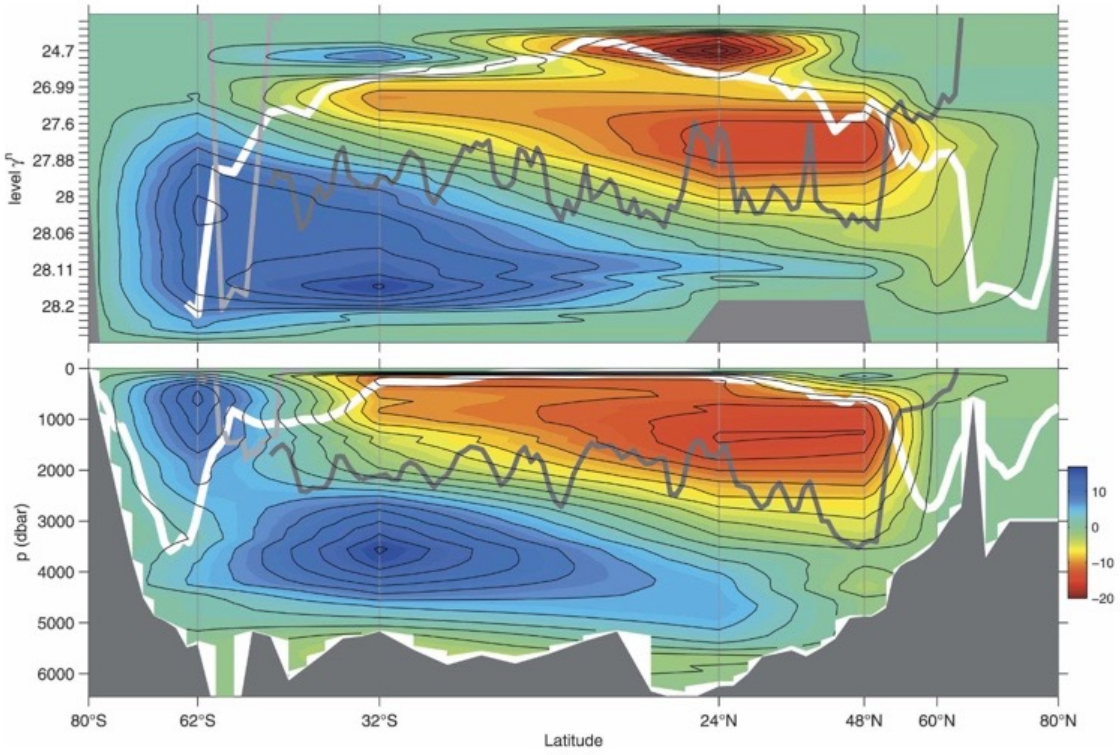


Figure 1.2: *Global overturning streamfunction (contours every 2 Sv) as a function of (top) density and (bottom) depth. The vertical grey lines indicate the position of hydrographic sections. The other lines show the (dark grey) mean depth of the ocean ridge crests, the (light grey) depth of the Scotia Arc (east of Drake Passage), and (white) the typical winter mixed layer density/depth. Figure from Lumpkin & Speer (2007).*

how fast tracers are going to be back into contact with the atmosphere and (ii) the location of tracer upwelling at the surface, with consequences for their global distribution and residence time. Given the climatic and biological importance of several tracers carried by the overturning circulation, it is important to understand how dense waters come back into contact with the atmosphere, at which locations and over which timescale, to have a better knowledge of the ocean's role in climate regulation.

In the deep ocean, far from the atmospheric buoyancy forcing and from the impact of the wind, turbulent diapycnal mixing becomes crucial for the closure of the deep branches of the ocean circulation, i.e. working to raise dense waters back to shallower depths, and so from there to the surface of the ocean (Marshall & Speer, 2012). The next section describes the impact of diapycnal mixing on the closure of the upper and lower cells of the global

MOC.

1.2 Role of diapycnal mixing in the MOC

1.2.1 Lower cell

The bottom limb of the lower cell flows in direct contact with, or in the proximity of, the bottom topography, where diapycnal mixing is enhanced by the breaking of internal waves interacting with topographic features, especially in the presence of rough topography. As a consequence, the dynamics of the lower cell are strongly dependent on diapycnal mixing. Following the logic that "what goes down must come up", it is necessary to provide energy to bring the deep, dense waters back to the surface, balancing the production of dense waters at the surface at high latitudes (St Laurent & Simmons, 2006). In the deep ocean, where neither the impact of the wind nor of the surface buoyancy fluxes penetrates, diapycnal mixing represents the primary source of energy for the lifting of deep waters back to shallower depths. In other words, diapycnal mixing is crucial for the existence of the lower cell of the MOC: in the absence of diapycnal mixing, there would be no mechanism to raise the dense waters back to shallower depths, and so there would be no mechanism to allow the formation of a deep stratification and a deep ocean circulation.

Estimates of the energy required to lift dense water masses and sustain the observed deep ocean circulation go back to Munk (1966), who used large-scale observations of temperature, salinity and tracers to infer a diapycnal diffusivity of $\kappa \sim 10^{-4}$ m^2 s^{-1} in the ocean interior (excluding the top and bottom kilometre). However, observations from tracer release experiments (e.g. Ledwell *et al.* (1993)) and microstructure data (e.g. Toole *et al.* (1994); Polzin *et al.* (1997)) return a different picture: they show that the diffusivity is $\kappa \sim 10^{-5}$ m^2 s^{-1} in the ocean interior (i.e. away from ocean topography), approximately one order of magnitude smaller than Munk's estimate. The disagreement between Munk's estimate and the more recent estimates has led to what is usually referred to as the "missing

mixing" problem, i.e. the estimated mixing does not provide enough energy to raise the dense water of the lower MOC to the surface. This paradox raised the question of what mechanisms could balance the dense water formation, i.e. how to balance the energetics of the lower MOC and sustain the deep stratification, for which around 2 TW of power had been estimated to be needed (Munk, 1966; Munk & Wunsch, 1998).

The missing mixing paradox has been solved by taking into account the role of the wind: winds pull dense waters to the surface, thus creating an adiabatic highway for dense waters to come back into contact with the atmosphere by flowing along density surfaces, which are steepened until they outcrop (i.e. intersect the surface). Thus, diapycnal mixing does not need to raise waters all the way to the surface, but only up to the density surfaces that outcrop at the surface at high latitudes.

In recent years, the role of mixing in setting the deep stratification and regulating the lower cell of the MOC has been further revisited, and vertical variability in mixing has proved to be key in setting the patterns of diapycnal upwelling (De Lavergne *et al.*, 2016; Ferrari *et al.*, 2016). In the deep ocean, mixing increases in the proximity of the ocean bottom (where more internal waves break), but it equals zero at the ocean boundary, in order to satisfy the condition of no buoyancy flux across the boundary. Such a pattern implies a more complex cross-density flow: water parcels are transformed into *denser* waters in the ocean interior, given that they tend to mix more with the denser water below than with the lighter water above, as a consequence of bottom enhanced mixing; on the contrary, water parcels in contact with the boundary transform into *lighter* waters, given that they can mix exclusively with the lighter waters above. While locally waters can either upwell or downwell in density space, dense waters must ultimately be raised to shallower depths, implying that the integrated along-boundary upwelling must compensate for, and overcome, the interior downwelling. Such spatial variability in diapycnal mixing has been previously observed, especially in tracer experiments close to topographic boundaries (e.g. Polzin *et al.* (1997); Ledwell *et al.* (2000)), but the implications of the observed mixing patterns

for the global ocean circulation have only been resonating with the scientific community in recent years, and are currently a topic of intense research.

To summarise, the lower cell of the MOC would not exist in the absence of diapycnal mixing, which is the key mechanism raising dense waters to shallower depths, from which waters can then be adiabatically upwelled following an along-isopycnal flow. Furthermore, diapycnal mixing does not act simply as a lifting process but can create complex patterns of water downwelling in the ocean interior and upwelling along topographic boundaries. Such spatial patterns are important in determining the rate at which different water masses can be mixed and the rate at which the tracers carried within them can be exchanged.

1.2.2 Upper cell

Contrary to the lower cell, which can be sustained only in the presence of diapycnal mixing, the upper cell of the MOC is thought to derive its energy mainly from the westerly winds blowing in the Southern Ocean, and has recently been described as a pole-to-pole overturning cell (Wolfe & Cessi, 2010, 2011; Marshall & Speer, 2012; Nikurashin & Vallis, 2012). Some inverse estimates, e.g. Sloyan & Rintoul (2001), Talley *et al.* (2003) and Lumpkin & Speer (2007), show that the upper cell also contains a diabatic component, even if not of leading-order importance in setting the strength of the upper cell circulation. From inverse models, the upper cell transport, which is approximately 18-20 Sv in the North Atlantic (Talley *et al.*, 2003; Lumpkin & Speer, 2007; Smeed *et al.*, 2014), decreases on its pathway to the Southern Ocean by about 6 ± 2 Sv (Talley *et al.*, 2003; Lumpkin & Speer, 2007), leaving about 12-14 Sv at 32°S to upwell adiabatically along the isopycnals. Indeed, these dense waters flow mainly above the mean depth of the mid-ocean ridge and are thus thought to be less exposed to the mixing generated by the breaking of internal waves in the proximity of the ocean bottom. Consequently, it is generally thought that less of such waters upwell through a mixing-driven process, but they mainly come back into contact with the atmosphere in the Southern Ocean, where the westerly winds allow for adiabatic upwelling

by tilting of the density surfaces (Marshall & Speer, 2012).

Neglecting the role of diapycnal mixing in the upper cell might be reasonable when trying to identify the dominant mechanisms setting the cell into motion, but can impact our ability to correctly estimate the transport and pathways of the upper cell and, even more importantly, it can impact our understanding of the exchange and distribution of tracers carried by such water masses.

1.2.3 Ocean overturning and stratification scaling relations

The relationships between the upper and lower cells and diapycnal mixing presented in the sections above are analysed here in more detail. Indeed, there is an extensive literature of theoretical scaling relations for the strength of the ocean overturning circulation and the depth of the ocean stratification. In particular, scaling relations have been derived for a steady state, zonally averaged ocean circulation and stratification by identifying the dominant terms in the momentum and buoyancy equations. The zonally averaged ocean circulation is best described in the transformed Eulerian-mean framework (Andrews & McIntyre, 1976; Marshall, 1997; Marshall & Radko, 2003), where the residual overturning streamfunction, $\psi = \overline{\psi} + \psi^*$, is the sum of the Eulerian-mean streamfunction, $\overline{\psi}$, namely the overturning streamfunction associated with the large-scale mean flow, and the eddy-induced streamfunction, ψ^*, namely the overturning streamfunction associated with mesoscale eddies. The residual streamfunction is related to the residual velocities through $(v, w) = (-\partial_z\psi, \partial_y\psi)$ (Marshall & Radko, 2003). The zonal mean, steady state momentum and buoyancy equations are

$$\psi = \overline{\psi} + \psi^* = -\frac{\overline{\tau_s}}{f_s\rho_0} + K_e s_b, \tag{1.1}$$

$$w\,\partial_z\overline{b} + v\,\partial_y\overline{b} = \partial_z(\kappa\,\partial_z\overline{b}), \tag{1.2}$$

where $\overline{\tau_s}$ is the zonally averaged surface wind stress in the Southern Ocean, f_s is the Coriolis parameter in the Southern Ocean, K_e is the isopycnal eddy diffusivity, used to represent the meridional eddy buoyancy flux, $s_b = -\partial_y \overline{b}/\partial_z \overline{b}$ is the slope of the zonally averaged isopycnals, $\overline{b}$ is the Eulerian-mean buoyancy, ρ_0 is a reference density, and κ is the diapycnal mixing diffusivity. Equation 1.1 indicates that the overturning streamfunction is set by the action of the wind, pulling dense waters back to the surface and acting to steepening the isopycnals, and mesoscale eddies, whose role in flattening the isopycnals can be represented via an eddy viscosity acting on the slope of the density surfaces, $K_e s_b$, following Gent & McWilliams (1990). Equation 1.2 indicates that diapycnal mixing, represented via a diapycnal diffusivity κ, drives a meridional and vertical velocity in an advective-diffusive balance. Equations 1.1 and 1.2 are subject to boundary conditions of no normal flow through boundaries and no buoyancy flux through side and bottom boundaries.

The above set of equations allows us to derive scaling relations for both the strength of the ocean overturning (ψ) and the depth of stratification (h) in the different dynamical regimes that characterise the upper and lower overturning cells. A summary of the scaling relations for each cell is briefly described below.

Scaling relations for the lower cell

The lower cell is characterised by density surfaces that outcrop in the Southern Ocean only, i.e. density surfaces that identify the dense waters formed exclusively around Antarctica. The denser of these density surfaces intersect the ocean bottom (as shown in observations; see for example World Ocean Circulation Experiment (WOCE) sections (Koltermann *et al.*, 2011)), while the lighter density surfaces above are approximately flat throughout the whole basin.

The strength and depth of the lower cell are controlled by the wind stress and the eddy diffusivity, which set the circulation in the circumpolar channel (namely in the Southern Ocean, where there are no continental barriers), and by the diapycnal diffusivity in the

ocean basin to the north. By comparing typical values for the present day ocean, Ito & Marshall (2008) show that the wind-driven circulation contribution to the lower overturning cell is negligible, indicating that the lower cell is regulated by a balance between the eddy-induced circulation in the circumpolar region and diapycnal diffusivity in the ocean basin:

$$-K_e\frac{h}{l} = -\frac{\kappa L}{h} + \frac{\kappa L}{H_{mix}}, \tag{1.3}$$

where L is the meridional distance over which diapycnal mixing acts, and it corresponds to (i) the meridional extent of the basin for density surfaces that are flat throughout the whole basin and (ii) the distance between the northern edge of the circumpolar channel and the location where isopycnals intersect the ocean floor in the basin for the density surfaces that incrop in the ocean bottom. l is the latitudinal extent of the circumpolar channel and h is the vertical scale of stratification - in this case of the lower cell. H_{mix} is the vertical length over which diapycnal mixing varies with depth.

Mashayek *et al.* (2015) allow diapycnal mixing to increase toward the ocean bottom and show that in the abyssal ocean, where density surfaces intersect the ocean floor, equation 1.3 can be simplified to a balance between the eddy-induced circulation (left-hand side) and the first term on the right-hand side, returning scaling relations for the lower overturning cell and its stratification as

$$\psi_{L1} \approx \sqrt{\frac{L}{l}K_e\kappa_b} \tag{1.4}$$

and

$$h_{L1} \approx -\sqrt{\frac{\kappa_b}{K_e}Ll}. \tag{1.5}$$

These scaling relations are equivalent to the scalings of Ito & Marshall (2008) and Nikurashin & Vallis (2011), with the difference that κ_b is the diapycnal diffusivity at the bottom (and not in the whole domain, as in previous studies where κ was kept constant) and L is not the whole length of the basin, as suggested in those studies, which do not take into account the fact that density surfaces must intersect with the ocean bottom to satisfy the condition of

no buoyancy flux across the boundary.

Above this layer, where density surfaces are approximately flat, the eddy-induced circulation is balanced by the residual between the two terms on the right-hand side of equation 1.3 (Mashayek *et al.*, 2015). Here, ψ and h scale as

$$\psi_{L2} \approx -\frac{K_e H_{mix}}{l} \tag{1.6}$$

and

$$h_{L2} \approx H_{mix}. \tag{1.7}$$

The scaling relations above indicate that diapycnal mixing in the basin and eddies in the circumpolar channel set the strength of the lower overturning cell and the lower stratification. In particular, the strength of the lower cell is proportional to $\kappa^{1/2}$ where isopycnals intersect the ocean bottom (Ito & Marshall, 2008; Nikurashin & Vallis, 2011; Mashayek *et al.*, 2015), while it scales with the vertical structure of diapycnal mixing (H_{mix}) where isopycnals are flat throughout the basin (Mashayek *et al.*, 2015).

Scaling relations for the upper cell

The upper cell is characterised by density surfaces that outcrop both in the Southern Ocean and in the North Atlantic. The strength and depth of the upper cell are set by a balance between the wind stress and mesoscale eddies in the Southern Ocean, diapycnal mixing in the ocean basin and dense water formation in the North Atlantic, as described by Gnanadesikan (1999):

$$-K_e \frac{h}{l} = \frac{\Delta b h^2}{f_n L_x} - \frac{\kappa L_y}{h} + \frac{\overline{\tau}_s}{\rho_0 f_s}. \tag{1.8}$$

Here, h is the vertical scale of the upper cell and L_y is the meridional extent of the basin (i.e. north of the Southern Ocean). f_n is the Coriolis parameter in the high-latitude North Atlantic, where dense waters are formed in a region of latitudinal extent L_x. Δb indicates the range of isopycnals that outcrop both in the Southern Ocean and in the North Atlantic.

In the limit of weak diapycnal mixing, the upper overturning circulation is set by a balance between the formation of dense waters in the North Atlantic and their adiabatic upwelling in the Southern Ocean (Gnanadesikan, 1999; Wolfe & Cessi, 2010; Nikurashin & Vallis, 2012). Nikurashin & Vallis (2012) has also shown that for isopycnals corresponding to the upper cell, the eddy-induced circulation is only 10-20% of the wind-driven circulation, and so equation 1.8 can be simplified to a balance between two terms:

$$\frac{\Delta b h^2}{f_n L_x} \approx \frac{\overline{\tau_s}}{\rho_0 f_s}, \tag{1.9}$$

from which the depth scale for the stratification of the upper cell h is determined as

$$h \approx \sqrt{\frac{\overline{\tau}_s f_n L_x}{\rho_0 f_s \Delta b}}. \tag{1.10}$$

From equation 1.9 and from the definition of h in this limit (equation 1.10), it follows that the strength of the upper cell is primarily determined by the wind-driven circulation in the Southern Ocean (Gnanadesikan, 1999; Wolfe & Cessi, 2010; Nikurashin & Vallis, 2012), i.e the more the wind pulls dense waters to the surface, the stronger the circulation will be:

$$\psi_U \approx \frac{\overline{\tau} L_x}{\rho_0 f_s}. \tag{1.11}$$

In the limit of large diapycnal diffusivity, the dense waters formed in the North Atlantic are returned to the surface via diapycnal upwelling in the basin, while the wind-driven upwelling can be neglected. It follows that equation 1.8 can be simplified as

$$\frac{\kappa L_y}{h} \approx \frac{\Delta b h^2}{f_n L_x}, \tag{1.12}$$

from which the depth and strength of the upper cell are determined as

$$h \approx \sqrt[3]{\frac{\kappa L_x L_y f_n}{\Delta b}} \tag{1.13}$$

and

$$\psi_U \approx \left(\frac{\Delta b}{f_n}\right)^{1/3} \kappa^{2/3} (L_x L_y)^{2/3}, \tag{1.14}$$

indicating that ψ_U scales with $\kappa^{2/3}$ and h scales with $\kappa^{1/3}$, as found in previous thermocline scaling studies (e.g. (Welander, 1971; Marotzke, 1997)).

1.3 Thesis questions

This thesis aims to investigate the impact of diapycnal mixing on the global overturning circulation and its implications for the transport and distribution of tracers carried by dense water masses.

Three main questions are addressed here.

Question 1 *Spatially variable versus constant parameterisations in mixing estimates: how do they shape the patterns of diapycnal upwelling/downwelling in the global ocean?*
To infer mixing from estimates of the more easily measured dissipation rate of turbulent kinetic energy, two parameters are needed: the first describes the fraction of internal wave energy that is dissipated locally, i.e. close to where internal waves are generated, instead of radiating away; the second describes the fractionation between the energy available to irreversible mixing, and the energy lost into heat through viscous dissipation of turbulent kinetic energy. Even if it is common to assume both parameters to be constant, there is extensive evidence that they have significant spatial variability, which can have important implications for the patterns of diapycnal exchange of water masses and tracers. Previous studies provide estimates or parameterisations of spatially variable parameters, but how their co-variations affect the internal wave-driven mixing has not been investigated yet.

Here, we build on previous estimates of spatially variable parameters to examine their individual and joint effect on the patterns of diapycnal mixing and its impact on the lower cell of the global MOC.

Question 2 *How much mixing is there in the Atlantic Ocean and how does it affect the circulation of the upper overturning cell?*

The rest of the thesis focuses on the role of mixing in the Atlantic Ocean. Here, we use several pre-existing estimates of turbulent mixing to build a first basin-wide quantification of mixing in the Atlantic Ocean, hence to quantify the role it plays in the regulation of the upper cell. The different estimates are observation-based and cover a wide range of processes that generate internal waves in the ocean interior. Therefore, a comparison of the results from different estimates also provides insight into which processes dominate in setting the global and basin rates of diapycnal mixing.

Question 3 *How does mixing affect the distribution of tracers carried by the upper overturning cell?*

Diapycnal mixing can exchange tracers between different water masses, strongly affecting their distribution and residence timescale. Here, we first use the observation-based existing estimates mentioned above to calculate a bulk estimate of the mixing-driven displacements that a tracer could experience while carried southward by the upper cell of the MOC, from the North Atlantic to the Southern Ocean. This estimate is then compared with results from pre-existing simulations of a three-dimensional sector model of the Atlantic Ocean. In the simulations, a tracer is released in the North Atlantic and we analyse the way it is mixed along its pathway to the Southern Ocean. In particular, we analyse how diapycnal mixing affects the tracer upwelling in the Southern Ocean, which has important implications for the global redistribution of tracers.

1.4 Thesis structure

This thesis is structured as follows. Chapter 2 provides the theoretical background to clearly define diapycnal mixing and how to estimate it from available measurements. It also presents the primary sources of turbulence that lead to diapycnal mixing in the ocean. Chapter 3 investigates the sensitivity of global mixing to different parameterisations used in estimating mixing from available estimates of the turbulent kinetic energy dissipation, addressing question 1. In Chapter 4 different estimates of diapycnal mixing are used to investigate the role of mixing in the Atlantic Ocean. In particular, they are used to quantify the role of mixing in the closure of the upper cell (question 2) and in modifying the distribution of tracers carried by the upper cell (question 3). Chapter 5 describes the results from tracer release experiments in numerical simulations of the Atlantic Ocean, in particular addressing the pathways of tracers in their southward journey to the Southern Ocean. Conclusions are given in Chapter 6.

Chapter 2

Diapycnal mixing: definition and sources

2.1 Diapycnal mixing definition

While large-scale oceanic flows are directed primarily along density surfaces (isopycnals), a cross-density component of the flow is crucial in generating and sustaining the deep ocean stratification. Using Munk & Wunsch (1998) words, "without deep mixing the ocean would turn, within a few thousand years, into a stagnant pool of cold salty water".

The ocean is a stably stratified environment, formed by layers of water whose density increases from the surface to the bottom. Therefore, it is necessary to provide energy to sustain diapycnal mixing, i.e. to transform waters into lighter or denser density classes by mixing light waters with the denser waters below, or by lifting dense waters above light ones. The necessary energy comes in the form of internal waves and the turbulence created by their breaking. Internal waves are primarily generated by the interaction of tidal flow with topography, wind fluctuations at the sea surface, and the interaction of ocean currents and eddies with the topography leading to lee waves (MacKinnon *et al.*, 2017). Internal waves dissipate their energy through several mechanisms, the most efficient ones being non-linear wave-wave interactions (Nikurashin & Legg, 2011), and scattering by small-

scale topography (Bühler & Holmes-Cerfon, 2011). During the cascade of wave energy down to dissipative scales, instabilities lead to the overturning or breaking of the waves, generating the turbulence that leads to diapycnal mixing.

Turbulent diapycnal mixing is defined as the fraction of energy from the breaking of an internal wave that mixes waters of different densities and irreversibly transforms them into different water masses. Hence, diapycnal mixing is described in terms of the energetics of the system. The rest of this section gives a definition of diapycnal mixing through the balances of kinetic and potential energies, that can be derived from the governing equations of the system.

The governing momentum, continuity and energy conservation equations (in the Boussinesq approximation, i.e. variations in density are sufficiently small compared to some characteristic reference density that they are only significant in the buoyancy force) are:

$$\frac{\partial \mathbf{u}}{\partial t} + \mathbf{u} \cdot \nabla \mathbf{u} = -\frac{1}{\rho_0} \nabla p + \frac{\Delta \rho}{\rho_0} \mathbf{g} + \nu \nabla^2 \mathbf{u}, \tag{2.1}$$

$$\nabla \cdot \mathbf{u} = 0, \tag{2.2}$$

$$\frac{D\rho}{Dt} = \kappa \nabla^2 \rho, \tag{2.3}$$

where $\mathbf{u} = (u, v, w)$ is the velocity vector, $\mathbf{g} = (0, 0, -g)$ represents the buoyancy term and g is the gravitational acceleration. The ratio $\Delta\rho/\rho_0$ in front of the buoyancy term derives from the Boussinesq approximation, in which the fluid density is represented as the sum of a mean reference component and small variations from the mean, $\rho = \rho_0 + \Delta\rho$. ν is the kinematic viscosity, and κ is the density diffusivity, taken here to be the same for temperature and salt.

To identify the relative importance of the different terms, it is useful to write the equations is non-dimensional form, representing each quantity as the product of a typical di-

mensional scale and a dimensionless component, such as:

$$\mathbf{u} = U\hat{\mathbf{u}}, \quad (x, y, z) = d(\hat{x}, \hat{y}, \hat{z}), \quad t = T\hat{t}, \quad p = P\hat{p} = \rho_0 U^2 \hat{p}, \quad \nabla = \frac{1}{d}\hat{\nabla} \quad \Delta\rho = \Delta\rho\hat{\rho}$$

where U, d, T, P and $\Delta\rho$ indicate the characteristic scales of velocity, length, time, pressure and density, and the hat variables are the non-dimensional components. The aspect ratio of the flow investigated here is close to unity, i.e. the variations of the flow in horizontal and vertical directions are similar and so we can use one characteristic length scale only. By using the scaling relations above, it is possible to rewrite the equations as:

$$\frac{U}{T}\frac{\partial\hat{\mathbf{u}}}{\partial\hat{t}} + \frac{U^2}{d}\hat{\mathbf{u}}\cdot\hat{\nabla}\hat{\mathbf{u}} = -\frac{\rho_0 U^2}{\rho_0 d}\nabla\hat{p} + \frac{\Delta\rho}{\rho_0}g\hat{\rho} + \nu\frac{U}{d^2}\hat{\nabla}^2\hat{\mathbf{u}}, \tag{2.4}$$

$$\frac{U}{d}\hat{\nabla}\cdot\hat{\mathbf{u}} = 0, \tag{2.5}$$

$$\frac{\Delta\rho}{T}\frac{D\hat{\rho}}{D\hat{t}} = \frac{\kappa\Delta\rho}{d^2}\hat{\nabla}^2\hat{\rho}. \tag{2.6}$$

By dividing each equation by the appropriate typical scales, it is possible to rewrite the above equations in terms of dimensionless numbers that describe the relative importance of the different terms. In particular, by substituting the scaling of T with $T = d/U$ and by dividing equation 2.4 by U^2/d, equation 2.5 by U/d and equation 2.6 by $\Delta\rho U/d$, we obtain the following set of equations (where the hats have been removed from the dimensionless components for better readability):

$$\frac{\partial\mathbf{u}}{\partial t} + \mathbf{u}\cdot\nabla\mathbf{u} = -\nabla p - Ri_0\rho + \frac{1}{Re}\nabla^2\mathbf{u}, \tag{2.7}$$

$$\nabla\cdot\mathbf{u} = 0, \tag{2.8}$$

$$\frac{D\rho}{Dt} = \frac{1}{RePr}\nabla^2\rho, \tag{2.9}$$

where

$Ri_0 = gd\Delta\rho/\rho_0 U^2$ is the bulk Richardson number, and d is a characteristic shear-layer length scale, (the gradient Richardson number, $Ri(z) = N^2/S^2$, returns the ratio between stratification and shear),

$N^2 = -(g/\rho_0)/(\partial\rho/\partial z)$ is the ocean density stratification,

$S^2 = (dU/dz)^2$ is the vertical shear of horizontal velocity,

$Re = Ud/\nu$ is the Reynolds number, which returns the relative importance of viscous and advective terms, and

$Pr = \nu/\kappa$ is the Prandtl number, which returns the relative importance of viscosity and diffusion of density.

To define diapycnal mixing it is necessary to look at the energetics of the system. Indeed, diapycnal mixing results in a change of density of the water masses involved, consequently changing the ocean stratification. As such, diapycnal mixing changes the potential energy of the system and raises its centre of mass. Moreover, diapycnal mixing is not directly measurable because of its high temporal and spatial heterogeneity and its small spatial scales, from a few tens of metres to centimetres. However, it is possible to relate mixing to other measurable quantities, and in particular, mixing can be inferred from measurements (or estimates) of the turbulent kinetic energy dissipation rate. These points, that diapycnal mixing is linked with changes in the system potential energy and can be inferred from the dissipation rate of turbulent kinetic energy, clearly show the connection between diapycnal mixing and the energetics of the system. The following paragraphs describe the balances for the kinetic, potential and total energy of the system. For further detail, see Drazin & Reid (2004), Caulfield & Peltier (2000), the review of Peltier & Caulfield (2003) and references therein.

The evolution of kinetic energy $\mathcal{K}$ of the flow governed by equations 2.7-2.9 is defined

as

$$\frac{d\mathcal{K}}{dt} = -Ri_0\langle\langle\langle\rho w\rangle_x\rangle_y\rangle_z - \frac{1}{Re}\langle\langle\langle(\nabla u)^2\rangle_x\rangle_y\rangle_z = \mathcal{H} - \epsilon, \tag{2.10}$$

with

$$\mathcal{K} = \langle\langle\langle(u^2 + v^2 + w^2)/2\rangle_x\rangle_y\rangle_z \tag{2.11}$$

and

$$-\mathcal{H} = \mathcal{M} + \mathcal{S}, \tag{2.12}$$

where the angle brackets denote averaging over the subscripted coordinate direction. The terms contributing to changing the kinetic energy are the buoyancy flux, $\mathcal{H}$, which represents the exchange between kinetic and potential energy reservoirs, and viscous dissipation, ϵ, representing the viscous loss of energy into heat.

Note that there are two distinct processes that contribute to $\mathcal{H}$: mixing ($\mathcal{M}$) and stirring ($\mathcal{S}$). Mixing involves irreversible changes in fluid properties that are directly associated with macroscopic fluid motions, whereas stirring involves reversible changes, i.e. changes that take place in a non-diffusive way (Peltier & Caulfield, 2003). If a parcel of dense water is lifted, thus generating a buoyancy flux, the rise in potential energy is irreversible only if there is a change in the parcel's density, i.e. only if mixing acts to change its density irreversibly. However, if gravity restores the parcel to its initial location without any change in density, the rise in potential energy is only temporary or, in other words, is reversible. It follows that values of $\mathcal{H}$ can be misleading as a proxy for mixing, and must, therefore, be averaged over sufficiently long timescales to cancel out the reversible buoyancy flux generated by stirring. Unfortunately, such averaging is not always possible, especially when working with oceanographic data that often have limited time series, and it is thus necessary to use another approach to separate the contribution of reversible and irreversible buoyancy flux. The formalism of Winters *et al.* (1995) distinguishes between the two sources of buoyancy flux by their impact on the potential energy, diapycnal mixing acting to increase the background potential energy, and stirring acting to increase the

available potential energy.

The evolution of the potential energy of the system is defined as

$$\frac{d\mathcal{P}}{dt} = -\mathcal{H} + \mathcal{D}_p, \tag{2.13}$$

with

$$\mathcal{P} = Ri_0\langle\langle\langle\rho z\rangle_x\rangle_y\rangle_z \tag{2.14}$$

and where $\mathcal{D}_p$ is the rate at which the potential energy of a statically stable density distribution would increase in the absence of macroscopic fluid motion, i.e. by molecular diffusion. Molecular diffusion adds a negligible contribution and acts on very long timescales, much longer than mixing or stirring, so that $\mathcal{D}_p << \mathcal{H}$.

Potential energy can be further split into available and background potential energy:

$$\mathcal{P} = \mathcal{P}_A + \mathcal{P}_B. \tag{2.15}$$

$\mathcal{P}_A$ is the fraction of potential energy available to the kinetic energy reservoir for stirring, and its evolution is given by

$$\frac{d\mathcal{P}_A}{dt} = -\mathcal{H} - \mathcal{M} = \mathcal{S}. \tag{2.16}$$

The background potential energy $\mathcal{P}_B$ is defined as

$$\mathcal{P}_B = \langle g\rho_B(z)z\rangle_z, \tag{2.17}$$

where $\rho_B(z)$ is the background density profile, associated with the minimum (background) potential energy of the system, i.e. the density profile generated by the re-arrangement of the actual density profile $\rho(z)$ when the system is statically stable (Peltier & Caulfield, 2003; Mashayek & Peltier, 2013). The energy in $\mathcal{P}_B$ cannot be extracted to drive fluid motions, and so is inaccessible to stirring. $\mathcal{P}_B$ can be increased only through irreversible

mixing processes:

$$\frac{d\mathcal{P}_B}{dt} = \mathcal{M} + \mathcal{D}_P. \tag{2.18}$$

Combining equations 2.10, 2.16, and 2.18, the evolution of the total energy of the system is given by

$$\begin{aligned} &\frac{dE}{dt} = \frac{d\mathcal{K}}{dt} + \frac{d\mathcal{P}}{dt} = \\ &= \frac{d\mathcal{K}}{dt} + \frac{d\mathcal{P}_A}{dt} + \frac{d\mathcal{P}_B}{dt} = \\ &= \mathcal{H} - \epsilon - \mathcal{H} - \mathcal{M} + \mathcal{M} + \mathcal{D}_P = \\ &= -\epsilon + \mathcal{D}_P \approx -\epsilon. \end{aligned} \tag{2.19}$$

Equation 2.19 indicates that the total energy decreases with time because of viscous dissipation, ϵ. How does diapycnal mixing participate in changing E? Diapycnal mixing does not reduce the total amount of energy, but acts as an energy transformer: it transforms kinetic energy into potential energy, and in particular, it increases the background potential energy at the expense of kinetic energy. In other words, if a system is perturbed, i.e. more energy is added to the system, the total energy is increased and the kinetic energy generated is partly dissipated through viscosity (ϵ) and partly exchanged with the potential energy reservoirs through the buoyancy flux $\mathcal{H}$. The fraction lost in dissipation is responsible for the decrease of the total energy with time, while the fraction exchanged with the potential energy reservoir is responsible for an increase of the background potential energy through irreversible mixing.

Given the role of mixing in changing the kinetic energy budget, through the buoyancy flux $\mathcal{H}$, the evolution of the kinetic energy of the system is now described in more detail. First, it is necessary to separate the different phases that characterise the transition to turbulence of a density stratified shear flow (Caulfield & Peltier, 2000). In the first stage, shear instability leads to the formation of a wave, whose characteristics are laterally periodic and so can be described as a two-dimensional system. As the wave grows, and its amplitude saturates, it generates a convectively unstable flow configuration that allows for the for-

mation of a secondary three-dimensional instability. When such unstable convective rolls break, energy is converted into turbulent diapycnal mixing and lost into dissipation.

The total kinetic energy ($\mathcal{K}$) can, therefore, be divided into three distinct terms: (i) mean kinetic energy ($\bar{\mathcal{K}}$), from the mean velocity of the flow $\bar{\mathbf{u}}$; (ii) the kinetic energy associated with the two-dimensional wave perturbation ($\mathcal{K}_{2D}$), from the velocity associated with such perturbations $\mathbf{u}_{2D}$; (iii) the kinetic energy associated with the three-dimensional convective instability ($\mathcal{K}_{3D}$), from the velocity associated with the three-dimensional perturbations $\mathbf{u}_{3D}$. Following Klaassen & Peltier (1985), an equation for the evolution of the three-dimensional kinetic energy can be shown to be of the form:

$$\frac{d\mathcal{K}_{3D}}{dt} = \mathcal{R}_{3D} + \mathcal{S}h_{3D} + \mathcal{A} - \mathcal{H}_{3D} - \epsilon, \tag{2.20}$$

where

$\mathcal{R}_{3D} = -\langle\langle\langle\ u_{3D}w_{3D}\dfrac{d\bar{u}}{dz}\ \rangle_x\rangle_y\rangle_z$

represents the turbulent extraction of energy from the mean shear field,

$\mathcal{S}h_{3D} = -\langle\langle\langle\ u_{3D}w_{3D}\left(\dfrac{\partial w_{2D}}{\partial x} + \dfrac{\partial u_{2D}}{\partial z}\right)\rangle_x\rangle_y\rangle_z$

represents the turbulent extraction of energy from the two-dimensional wave structures,

$\mathcal{A} = -\dfrac{1}{2}\langle\langle\langle\ (u_{3D}^2 - w_{3D}^2)\left(\dfrac{\partial u_{2D}}{\partial x} - \dfrac{\partial w_{2D}}{\partial z}\right)\rangle_x\rangle_y\rangle_z$

is a measure of anisotropy, representing the stretching deformation associated with the three-dimensional perturbations,

$\mathcal{H}_{3D} = Ri_0\langle\langle\langle\ \rho_{3D}w_{3D}\ \rangle_x\rangle_y\rangle_z$

represents the buoyancy flux associated with the three-dimensional perturbations, and

ϵ represents the viscous dissipation associated with the three-dimensional perturbations.

The balance between the terms described above is often simplified on the basis of three assumptions: (1) the vertical diffusivity is dominated by fully developed turbulence; (2) turbulence is in a steady balance between production, dissipation and diapycnal mixing;

(3) turbulence is isotropic. These assumptions eliminate the terms associated with the first phase of transition to turbulence but focus on the mixing and dissipation generated during the second phase only. The simplified balance is usually referred to as the Osborn balance, from Osborn (1980), and it takes the form of:

$$\mathcal{R}_{3D} \approx \mathcal{H}_{3D} + \epsilon. \tag{2.21}$$

The Osborn balance is particularly useful in inferring diapycnal mixing from oceanographic data. Indeed, as mentioned before, diapycnal mixing is not directly measurable, and we rely on inferring it from measurements (or estimates) of the viscous dissipation rate. The Osborn balance can be re-arranged to provide a simple relation between diapycnal mixing and the viscous dissipation. The ratio of the buoyancy flux to the turbulent extraction of energy is defined to be the mixing efficiency:

$$\frac{\mathcal{H}_{3D}}{\mathcal{R}_{3D}} = \eta, \tag{2.22}$$

which we can use to rewrite the turbulent extraction of energy term as

$$\mathcal{R}_{3D} = \frac{\mathcal{H}_{3D}}{\eta}. \tag{2.23}$$

Re-arranging equation 2.21 with 2.23, we can rewrite the buoyancy flux as

$$\mathcal{H}_{3D} \approx \frac{\eta}{1-\eta}\epsilon \approx \Gamma\epsilon, \tag{2.24}$$

where $\Gamma = \eta/(1-\eta)$ is the flux coefficient that describes the partitioning of energy between diapycnal mixing and dissipation. The relation in equation 2.24 is going to be key in the rest of this thesis: it represents the connection between available estimates of the viscous dissipation rate, ϵ, and the unknown diapycnal mixing, $\mathcal{M}$. Equation 2.24 also allows us to

discuss diapycnal mixing in the form of a diffusivity coefficient:

$$\kappa \approx \frac{\mathcal{H}_{3D}}{N^2} \approx \frac{\Gamma \epsilon}{N^2}. \tag{2.25}$$

This definition is widely used and convenient, especially in a modelling context, given that mixing is represented in models by defining a diapycnal diffusivity (κ). On the other hand, the same value of the diffusivity coefficient does not necessarily lead to the same amount of turbulent mixing, given that it takes less energy to mix weakly stratified waters than a strongly stratified flow (see for example Nikurashin & Ferrari (2013)).

Equation 2.24 neglects some terms that the work of Mashayek *et al.* (2013*a*) has shown to be non-negligible. Mashayek *et al.* (2013*a*) compare the full balance (equation 2.20) with the simplified Osborn balance (equation 2.21) and show that the assumptions (1) - (3) break down when the Richardson number is larger than the corresponding mixing efficiency, suggesting that the dependence of mixing efficiency on the Richardson number is non-monotonic. Hence, the terms that are neglected in the simplified balance suggested by Osborn (1980) could be taken into account by formulating a non-constant mixing efficiency i.e. a spatially variable flux coefficient (will be discussed in chapter 3).

Now that diapycnal mixing has been defined, this section continues with a description of its main sources.

2.2 Diapycnal mixing sources

The ocean interior is filled with internal waves that form mainly near the surface and propagate downward, or that form near the bottom and propagate upward. Figure 2.1 shows a schematic representation of the mechanisms generating internal waves throughout the water column. Several processes lead to internal wave generation, and only a fraction of them are included in this thesis. In particular, here the focus is on the processes that generate internal waves in the deep ocean, to investigate their impact on the deep waters of the global

MOC. The primary processes included here are internal tides, lee waves generated by deep currents (or eddies) interacting with topography, and near-inertial waves, which are mainly sourced at the ocean surface but can potentially propagate far into the ocean interior. Internal waves generated in the upper ocean by wind-driven oscillations of the mixed layer and low-mode internal waves that radiate away to break along continental shelves are not the main focus of this study and are mentioned only briefly.

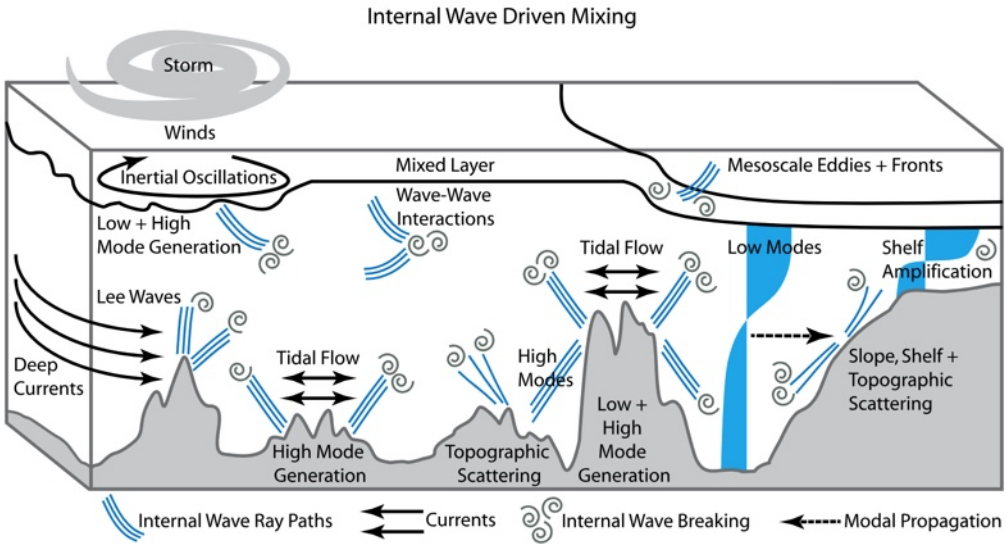


Figure 2.1: *Schematic of the processes that generate internal waves, whose breaking leads to diapycnal mixing. From MacKinnon* et al. *(2017)*

2.2.1 Internal tides

The tidal rise and fall of the ocean surface is mainly associated with barotropic tidal currents, which are uniform in depth apart from a reduction near the seafloor because of bottom friction (Garrett & Kunze, 2007). In stratified water, the interaction of barotropic tidal currents with the ocean's seafloor topography leads to the formation of internal, baroclinic waves at tidal frequency, called internal tides. Under the assumptions of small topographic steepness (topographic slope smaller than internal wave slope) and small tidal excursion compared to topographic scales, the barotropic-to-baroclinic energy conversion, i.e. the

rate of internal-tide energy generation, is well predicted by linear theory (see review in Garrett & Kunze (2007)). It has been estimated that internal tides contribute up to 1 TW of power to the deep ocean (Egbert & Ray, 2000), where they are one of the main sources of turbulent mixing. Indeed, the vertical shear of the horizontal currents associated with internal tides can be strong enough to lead to instability and turbulence, or can feed energy into smaller-scale internal waves which then break (St Laurent & Garrett, 2002; Garrett & Kunze, 2007), contributing to enhanced diapycnal mixing in the deep ocean and thus affecting the ocean circulation and the vertical fluxes of tracers (Sandstrom & Elliott, 1984).

2.2.2 Geostrophic flow over topography

In a stratified environment, the interaction of geostrophic flows with a variable bottom topography generates internal waves, and in particular lee waves. The interaction of the mean flow with the internal waves that are propagating from the bottom towards the surface creates the condition for enhanced mixing: when the velocity of the mean flow and of the propagating wave match, a critical layer forms in which turbulent mixing is enhanced (Garrett & Munk, 1979). This critical layer forms, in particular, where bottom geostrophic flows are strong and topography is rough (Nikurashin & Ferrari, 2011), and indeed the energy flux conversion from geostrophic flows into internal waves is particularly large in the Southern Ocean and in the tropical eastern Pacific, i.e. in regions of deep-reaching bottom currents and eddies (Nikurashin & Ferrari, 2011). It has been estimated that lee waves contribute ~0.2 TW of power to the deep ocean, but most of that contribution seems to come from the Southern Ocean region, where they are an important source of turbulent mixing (Nikurashin & Ferrari, 2010*a*, *b*).

2.2.3 Near-inertial waves

Near-inertial waves, or internal gravity waves with a frequency close to the Earth's rotational frequency, are a ubiquitous phenomenon in the ocean given that nearly any forcing

excites near-inertial motions. The primary mechanisms generating near-inertial waves are the wind stress on the surface of the ocean, non-linear wave-wave interactions, lee waves formed by the interaction of geostrophic flow with the bottom topography, and spontaneous emission through loss of balance, but the relative importance of these different mechanisms is still unknown (see review in Alford *et al.* (2016)). Wind stress clearly plays an important role in generating near-inertial waves, which makes it the most understood and studied of the different mechanisms. Therefore, the importance of near-inertial waves in enhancing the mixing in the upper ocean is well established. On the contrary, it is still not well understood how near-inertial waves propagate downwards from the ocean surface, and how important the sources of near-inertial waves in the deep ocean are. Alford & Whitmont (2007) look at current-metre records and show that near-inertial wave energy decreases only very slowly with depth, with the seasonal cycle only partially affecting the result, which suggests that near-inertial waves could play a non-negligible role also in deep ocean mixing.

2.2.4 Other sources

There are other sources of internal waves that are not the main focus of this thesis, and so are only briefly mentioned in this section. These include wind-generated internal waves that are not near-inertial waves, such as waves generated by oscillations of the mixed layer due to storms or wind bursts (D'Asaro, 1985; Wunsch & Ferrari, 2004). Whalen *et al.* (2018) have also shown that the mixing generated in the upper ocean by near-inertial waves is enhanced in the presence of large eddy kinetic energy, indicating that the mesoscale flow (10-100 km) can contribute to determining the spatial (both horizontal and vertical) and temporal variability of turbulent mixing.

Finally, this study does not account for internal waves that do not break locally, i.e. at the site where they have been generated. Internal waves have a complex vertical structure, and different processes can generate internal waves of different modes. High-mode waves

tend to break locally, while low-mode waves tend to radiate away, and can travel long distances (thousands of kilometres) before breaking, therefore contributing to turbulent mixing in regions far away from where they were generated. The fraction of low-mode waves generated by different mechanisms, where they break and how much mixing they generate are still unknowns and are topics of current research.

Chapter 3

Mixing sensitivity to internal wave local breaking and mixing efficiencies

The research presented in this chapter is published in:

"Sensitivity of deep ocean mixing to local internal tide breaking and mixing efficiency", L. Cimoli, C.P. Caulfield, H.L. Johnson, D.P. Marshall, A. Mashayek, A.C. Naveira-Garabato, and C. Vic., Geophysical Research Letters, 43. https://doi.org/10. 1029/2019GL085056

This chapter focuses on the role of mixing in setting the patterns of diapycnal downwelling and upwelling in the deep ocean, for density classes representative of the lower cell of the MOC. In particular, this chapter describes the sensitivity of diapycnal mixing to changes in two parameters: q and Γ. The former, q, quantifies the local breaking efficiency, i.e. the fraction of internal wave energy that is spent close to where the waves have been generated, while the rest radiates away. The latter, Γ, is the flux coefficient defined in equation 2.24 and quantifies the fraction of the energy (generated through a wave-breaking event) translated into irreversible mixing, while the rest is lost to viscous dissipation. Fol-

lowing the notation in chapter 2, the flux coefficient is defined as

$$\Gamma = \frac{\eta}{1-\eta} = \frac{\mathcal{H}_{3D}}{\epsilon},$$

where η is the mixing efficiency, $\mathcal{H}_{3D}$ is the buoyancy flux and ϵ is the dissipation rate of turbulent kinetic energy. Diapycnal mixing ($\mathcal{M}$) is the primary term contributing to the buoyancy flux, while diffusion via molecular viscosity ($\mathcal{D}_p$) is much smaller, such that $\mathcal{H}_{3D} = \mathcal{M} + \mathcal{D}_p \approx \mathcal{M}$ (recalling that stirring does not contribute to irreversible mixing). Given the difficulties in directly measuring mixing, it is possible to infer it from estimates of ϵ through some knowledge of Γ.

Therefore, q and Γ are parameters which map the global and local distribution of wave energy into diapycnal mixing and dissipation (figure 3.1). Due both to lack of knowledge of their variation and for practical reasons, it is customary to assume constant values for both q and Γ: $q = 0.3$, i.e. only one third of the wave energy is dissipated locally (Jayne, 2009; St Laurent *et al.*, 2002), and $\Gamma = 0.2$, i.e. assuming a fixed partitioning of energy between $\mathcal{M}$ and ϵ. These constant values are used in parameterisation of deep ocean mixing in coarse resolution ocean and climate models that do not resolve the internal wave field and wave breaking.

The choice of $q = 0.3$ derives from earlier estimates of the tidal energy flux in different topographic regions (Egbert & Ray, 2003; St Laurent *et al.*, 2002; St Laurent & Garrett, 2002); however, such studies did not account for the energy converted from small-scale waves, nor resolve the interaction of waves with small topographic features (St Laurent *et al.*, 2002; St Laurent & Garrett, 2002), or focused on particular regions (Egbert & Ray, 2003) where the narrowness and steepness of the ridge are not representative of the global ocean. The sensitivity of the mixing-driven water mass transformation to different values of q has been explored in Nikurashin & Ferrari (2013) (see their supplementary material). Their result suggests that turbulent mixing is simply linearly dependent on the value of q

chosen, but they limited their sensitivity tests to relatively few values of constant q, without exploring non-constant values that would take into account its spatial variability. A constant rate of internal wave breaking does not do justice to the different regimes of internal wave generation, and likely induces biases in global circulation models (MacKinnon *et al.*, 2017).

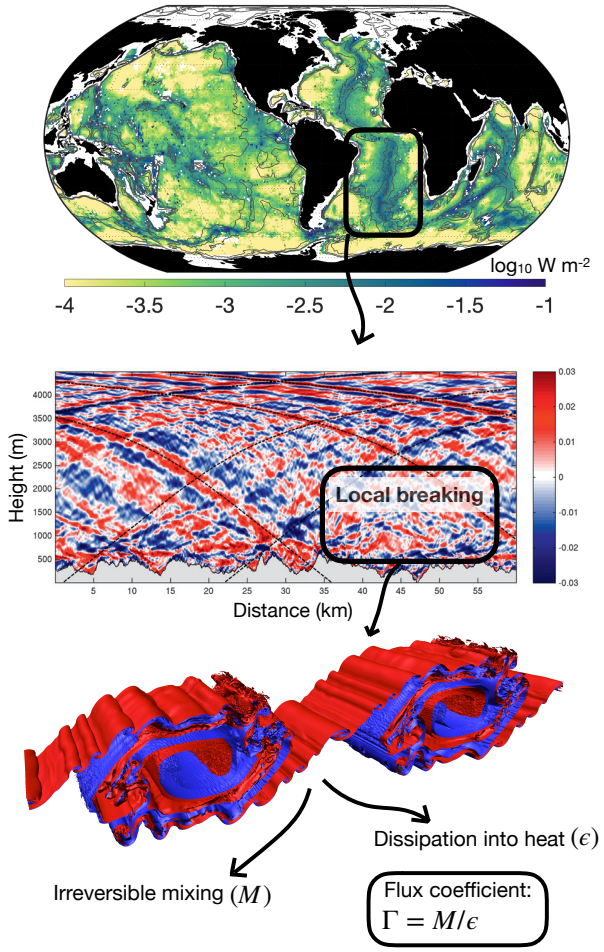


Figure 3.1: *Distribution of energy from global to micro scales. Top panel: global distribution of energy in the internal wave field induced by the flow of tides, jets and eddies over bottom topography (reconstructed from the estimates shown in figure 3.2 and discussed in section 3.1). Middle panel (from Mashayek* et al. *(2017*b*)): generation of internal tides over rough topography (the panel shows internal tide velocities [m/s] from numerical simulations from Nikurashin & Legg (2011)). A fraction of the generated wave energy,* $(1 - q)$*, radiates away from the generation region, while the rest, fraction q, gets invested in localised breaking of waves. Bottom panel (from Mashayek* et al. *(2017*a*)): from each wave breaking event, part of the generated turbulence is converted into irreversible mixing (*$\mathcal{M}$*), while the rest is dissipated into heat (*ϵ*). The ratio* $\mathcal{M}/\epsilon$ *defines the flux coefficient* Γ.

$\Gamma = 0.2$ was the empirical upper bound proposed by Osborn (1980), but since then there has been extensive evidence that Γ can vary significantly depending on the properties of the flow (e.g. Moum (1996); Ruddick *et al.* (1997); St Laurent & Schmitt (1999); Smyth & Caldwell (2001); Mashayek *et al.* (2013*a*); Salehipour *et al.* (2016); Gregg *et al.* (2018)). To represent such variability, Γ has often been parameterised (e.g. see Shih *et al.* (2005); Bouffard & Boegman (2013)) as a non-monotonic function of the buoyancy Reynolds number, defined as

$$Re_b = \frac{\epsilon}{\nu N^2}. \tag{3.1}$$

Re_b represents the ratio of the tendency of turbulence to mix density to the influence of stratification and viscosity in suppressing vertical motion and turbulence (Mashayek *et al.*, 2017*c*) and returns a natural, non-trivial parameterisation of Γ, although other more complicated multidimensional parameterisations exist (eg. Salehipour *et al.* (2015)). As discussed in Mashayek *et al.* (2017*c*), there is no physical mechanism that justifies the choice of $\Gamma = 0.2$. In fact, firstly, $\Gamma(Re_b)$ has a strong spatial variability (see later figure 3.3), important in setting the patterns of local upwelling/downwelling and so affecting the strength of the deep ocean overturning circulation. Secondly, a constant Γ does not allow mixing to vanish close to the bottom, where stratification tends to zero; the parameterisation $\Gamma(Re_b)$ takes into account this physical mechanism. Previous studies have investigated the sensitivity of the mixing-driven deep overturning circulation to variations in Γ (De Lavergne *et al.*, 2016; Mashayek *et al.*, 2017*c*), but without exploring its co-variation with other parameters.

From previous studies, the diapycnal water mass transformation of dense waters seems to be linearly dependent on the values of q and $\Gamma(Re_b)$ chosen, but none of them have explored the effect of a co-variation of q and $\Gamma(Re_b)$. When adopting a non-uniform q, the patterns of local diapycnal mixing and dissipation are going to change, since more or less energy is locally generating turbulence and so is available to be converted into diapycnal mixing. A variation in the local dissipation rate ϵ will consequently change

the flux coefficient $\Gamma(Re_b)$, whose parameterisation depends on ϵ itself. Therefore, these parameters should be co-varied when exploring the sensitivity of diapycnal mixing, and so of the dense water mass transformation, to different parameters.

This chapter explores the effects of a co-variation of q and $\Gamma(Re_b)$ on diapycnal mixing across the deep global meridional overturning circulation, and explores how the combined variation of these two parameters modifies the global patterns of upwelling and downwelling of deep waters. Note that the work presented in this chapter builds upon previous estimates of the energy flux into internal tides and lee waves, of the local breaking efficiency of internal waves and of parameterisation of the flux coefficient as a function of the buoyancy Reynolds number. However, examining the impacts of the co-variations of q and Γ on the deep ocean internal wave driven-mixing is novel and useful, as mixing parameterisations in current global ocean models use constant values of q and Γ. As such, the present study contributes to a better understanding of diapycnal mixing and could lead to more realistic parameterisations of diapycnal mixing in ocean models.

Section 3.1 presents the estimates of energy conversion from internal tides and lee waves used here and their rate of local breaking q. Section 3.2 describes (i) how turbulent mixing can be inferred from estimates of the turbulent dissipation ϵ by calculating the amount of energy from locally breaking waves, and (ii) how such energy is split between dissipation and irreversible mixing through some parameterisation of the flux coefficient Γ. The implications of a co-varying q and Γ are presented in section 3.3. It is shown that the sensitivity of the water mass transformation to the co-varying parameters is strongly non-linear and has a key impact on both the global turbulent water mass transformation rate and on the rate of turbulent upwelling or downwelling of dense water masses into the different ocean basins. A short note on the contribution of near-inertial waves to the global water mass transformation rate is given in section 3.3.2, and a discussion of the results presented in this chapter is given in section 3.4.

3.1 Internal waves: energy and radiation

In the deep ocean, internal tides and lee waves (see section 2.2) are the primary sources of diapycnal mixing. Estimates of the energy converted into these internal waves and of their radiation rate are here used to infer the amount of diapycnal mixing in the deep ocean, the patterns of diapycnal upwelling/downwelling and the rate of mixing-driven water mass transformation in the ocean interior.

3.1.1 Internal wave energy

The amount of energy converted into internal tides and lee waves indicates the regions where most internal waves are generated. Assuming that at least a fraction of these waves break locally, these estimates of energy conversion are also an indicator of the regions where diapycnal mixing will happen, through internal wave breaking.

The rate of internal-tide energy generation is well predicted by linear theory (Garrett & Kunze, 2007), and so linear analytical models have been used to estimate the rate of internal tide generation $E_t(x, y)$ globally (Green & Nycander, 2013; Jayne & St Laurent, 2001; St Laurent *et al.*, 2002; Nycander, 2005). Here we use the global estimate of tidal energy conversion into normal modes from the recent work of Vic *et al.* (2019). The total energy conversion for the most energetic tides (semi-diurnal and diurnal) in the deep ocean is shown in figure 3.2a. Global patterns are consistent with previous estimates, showing enhanced conversion over mid-ocean ridges, seamounts and continental shelf breaks (Green & Nycander, 2013; Nycander, 2005).

The energy flux conversion from geostrophic flows into internal waves, E_g, is predicted by linear theory in the limit of small topographic steepness, i.e. when the topographic slope is smaller than the lee wave slope (Bell, 1975). Here we use the global estimate of energy conversion into lee waves from Nikurashin & Ferrari (2011), shown in figure 3.2c. The energy flux into lee waves is particularly large in the Southern Ocean and in the tropical

eastern Pacific, i.e. in regions of deep-reaching bottom currents and eddies.

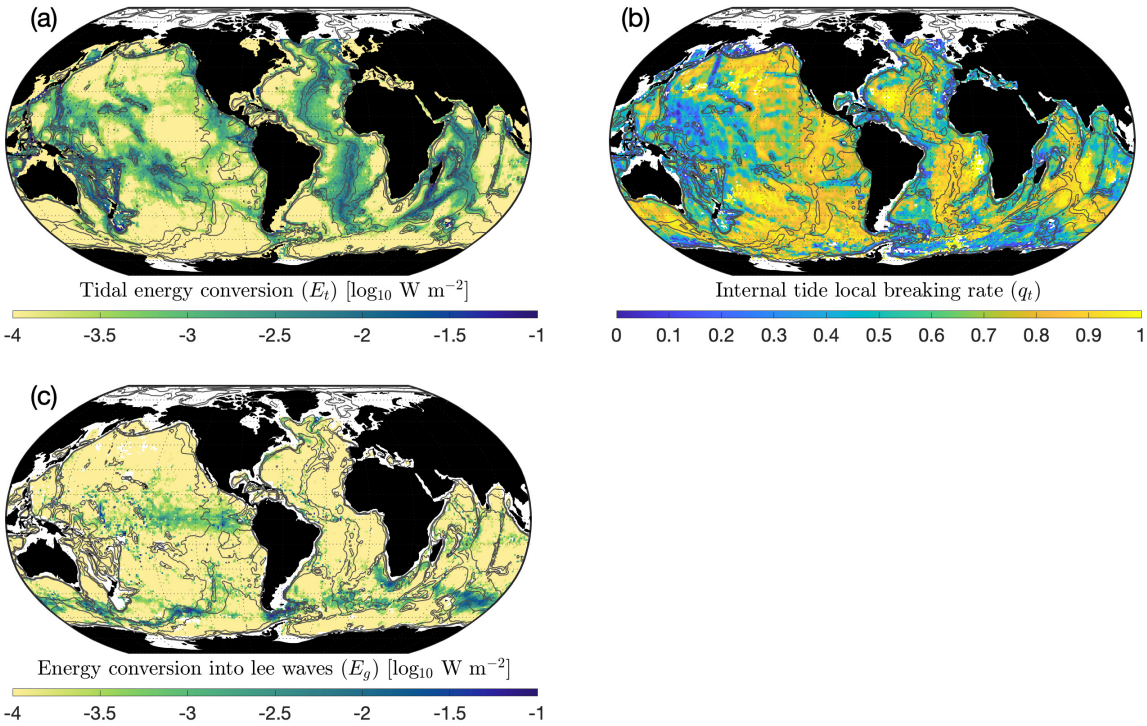


Figure 3.2: *(a) Global map of tidal energy conversion (log scale) reproduced from Vic* et al. *(2019). (b) Global map of the fraction of locally breaking internal tides, reproduced from Vic* et al. *(2019). (c) Global map of energy conversion into lee wave (log scale) reproduced from Nikurashin & Ferrari (2011).*

3.1.2 Internal wave radiation

The energy conversion estimates presented above are a proxy for the regions of enhanced diapycnal mixing, but it is important to take into account that only a fraction of the above energy is actually converted into local mixing: a fraction q of internal wave energy is spent close to the generation site, hence contributing to near-field mixing, whereas the rest of the energy $(1 - q)$ propagates away before contributing to far-field mixing. This separation has been discussed for internal tides, for example, in the review paper by MacKinnon *et al.* (2017). This section describes the parameterisation of a spatially variable q used here to test the sensitivity of diapycnal mixing to the amount of waves radiating away. The

following notation is used: q_t describes the local breaking efficiency for internal tides, and q_g describes the local breaking efficiency for lee waves.

Previous studies have shown observational evidence for a strong geographical variation in q_t (St Laurent & Nash, 2004; Lefauve *et al.*, 2015), yet current mixing estimates use a constant value of 0.3. For example, climate and ocean models such as the Community Climate System Model (CCSM) and the Nucleus for European Modeling of the Ocean (NEMO) use a constant value $q_t = 0.3$ in parameterisation of tidal mixing. Internal tides span a wide range of horizontal and vertical scales, and it is customary to cast them into a set of orthogonal modes whose structure is determined by the local stratification. This modal decomposition is particularly useful to separate internal tides into two broad families of waves. Low-mode (i.e. large-scale) internal tides are able to propagate over one thousand kilometres from their generation site before breaking into turbulence (Zhao *et al.*, 2016). On the contrary, high-mode (i.e. small-scale) internal tides are more prone to local dissipation (St Laurent & Nash, 2004; Vic *et al.*, 2018). Hence, low-mode internal tides contribute to far-field mixing whereas high-mode internal tides contribute to near-field mixing (MacKinnon *et al.*, 2017). Vic *et al.* (2019) used a modal partitioning to separate the portion of internal tides contributing to near-field dissipation (i.e. tides with modes higher than 4, see Vic *et al.* (2019) for details) from the total energy conversion, hence determining a geographically variable $q_t = q(x, y)$ (figure 3.2b). Strikingly, $q_t(x, y)$ displays significant geographical variability and equals ~0.6 on average, much higher than the canonical value of 0.3. Stemming from the modal partitioning, $q_t(x, y)$ is small over steep and narrow ridges, e.g. the Hawaiian Ridge, and seamounts, which generate preferentially low-mode internal tides, hence leaking energy away. On the contrary, $q_t(x, y)$ is much higher over widely spread mid-ocean ridges featuring rough topography (e.g. the Mid-Atlantic Ridge) that mostly generate high-mode internal tides. We will use this map of spatially variable $q_t(x, y)$ to explore the sensitivity of diapycnal mixing to changes in the local breaking efficiency.

The radiation of lee waves from the source location is controlled by the ratio of the topographic slope to the slope of the internal wave phase lines. Different studies report that, depending on the topographic to internal wave slope ratio, the fraction of lee waves that break locally can vary between $q_g = 0.1 - 0.5$ (Nikurashin & Ferrari, 2011; Sheen *et al.*, 2013; Zheng & Nikurashin, 2019). Here, a constant value $q_g = 0.3$ is adopted. Changes in q_g might affect the estimates of diapycnal mixing in the Southern Ocean, but are not expected to alter significantly the results in the rest of the ocean basins, where the contribution from lee waves is small.

3.2 From internal wave breaking to irreversible mixing

This section describes first how we estimate the fraction of the energy conversion from internal waves that break locally versus the fraction that radiates away, and secondly how we parametrise the flux coefficient Γ, i.e. the parameter that allows us to estimate how much of the energy from locally breaking waves is converted into diapycnal mixing, rather than being lost in viscous dissipation.

3.2.1 Energy from locally breaking internal waves

The combined contribution of internal tides and lee waves gives us an estimate of the total internal wave energy conversion in the deep ocean. Through q_t and q_g, which respectively describe the local breaking efficiency for internal tides and lee waves, and assuming an exponential decay scale in the vertical for the waves breaking in the deep ocean, the energy locally available to turbulence is given by:

$$E_{loc} = (q_t E_t + q_g E_g)\mathcal{F}(z) \tag{3.2}$$

$$\mathcal{F}(z) = \frac{e^{-(H+z)/\zeta}}{\zeta(1 - e^{-H/\zeta})} \tag{3.3}$$

where z is the height above the bottom, H is the total depth of the water column and ζ is the vertical decay scale of turbulence, taken to be 500 m. The vertical decay scale described by $\mathcal{F}(z)$ is motivated by turbulence observations from the abyssal ocean and the continental slope (St Laurent *et al.*, 2002). Note that the calculation of E_{loc} does not take into account the contribution of radiating internal waves originated in other locations.

3.2.2 A parameterisation for the flux coefficient

Diapycnal mixing is a process that requires both turbulence and stratification, but more precisely it emerges only when both turbulence and stratification fall within a specific range of values. Mixing is weak in the limits of both weak and strong stratification, the former because there is not enough density gradient for waters to be mixed and the latter because a too strong stratification can suppress mixing. Also, in the limit of strong turbulence, stratification is quickly eroded and only a small amount of energy is converted into mixing. Therefore, there must be a range of values of turbulence and stratification within which mixing is more efficient (de Lavergne *et al.*, 2016; Mashayek *et al.*, 2017*c*), thus leading to a larger flux coefficient.

The above limits are important when inferring $\mathcal{M}$ from the internal wave energy conversion, but they are not accounted for with a constant flux coefficient. Here we use the parameterisation of Γ described by Mashayek *et al.* (2017*c*) to account for the effects of turbulence and stratification on the flux coefficient. Mashayek *et al.* (2017*a*) parameterises the decrease of the flux coefficient in the limits described above through the non-monotonic dependence of Γ on the buoyancy Reynolds number, Re_b, as shown in figure 3.3a. With maximum $\Gamma^*(Re_b^*)$ when $Re_b = Re_b^*$, $\Gamma(Re_b)$ increases with $\sqrt{Re_b}$ when $Re_b < Re_b^*$ and decreases with $1/\sqrt{Re_b}$ when $Re_b > Re_b^*$. This parameterisation is based on data from oceans (Smyth & Caldwell, 2001), lakes (Bouffard & Boegman, 2013) and high resolution direct numerical simulations (Mashayek & Peltier, 2013; Mashayek *et al.*, 2013*a*; Salehipour & Peltier, 2015), which all show the non-monotonic relationship between $\Gamma(Re_b)$ and Re_b

described above.

As already noted, it is natural that the first leading order parameterisation of Γ is in terms of Re_b. Although there are other possible parameterisations (eg. Salehipour *et al.* (2016)), based for example on the Richardson number $Ri = N^2/S^2$, there is some evidence, at least in idealised flows, that Ri and Re_b are inversely correlated (eg. Lucas & Caulfield (2017)).

The spatial variability of $\Gamma(Re_b)$ is shown in figure 3.3b at depth of 3000 m and in figure 3.3c on the isopycnal $\gamma^n = 28.1$. $\Gamma(Re_b)$ has been calculated by applying a variable $q_t(x, y)$ to the estimates of internal tide dissipation rates, and by using a climatological stratification (N^2) from WOCE climatology (Koltermann *et al.*, 2011). Following the dependence of Γ on Re_b shown by Mashayek *et al.* (2017*c*) (see their figure 3) inferred from observational datasets and results from direct numerical simulations, Re_b^* is here chosen to be 100, and $\Gamma^*(Re_b^*) = 0.35$. Note that while the estimates of energy conversion into internal waves, the map of spatially variable $q_t(x, y)$ and the way the flux coefficient is parameterised are built on previous work, the way they have been combined in this work is novel. As such, the global maps of the flux coefficient shown in figure 3.3 have not been presented in any study before. Γ increases in the proximity of complex topographic structures (figures 3.3a,b), but is largest on the ridge's flanks, rather than at the crest. On the ridge crest, where ϵ is the largest (see later figure 3.4), the combination of large values of ϵ and the decrease of stratification with depth, leads to a larger buoyancy Reynolds number ($Re_b \sim 1000$, not shown), and so to a reduction of the flux coefficient (figure 3.3a). Also the zonal average of the flux coefficient (figure 3.3d) shows that $\Gamma(Re_b)$ intensifies in the deep ocean, where turbulence is larger, but decreases in the proximity to the bottom, where stratification vanishes. Figure 3.3d also shows the zonally averaged neutral density contours in the deep ocean.

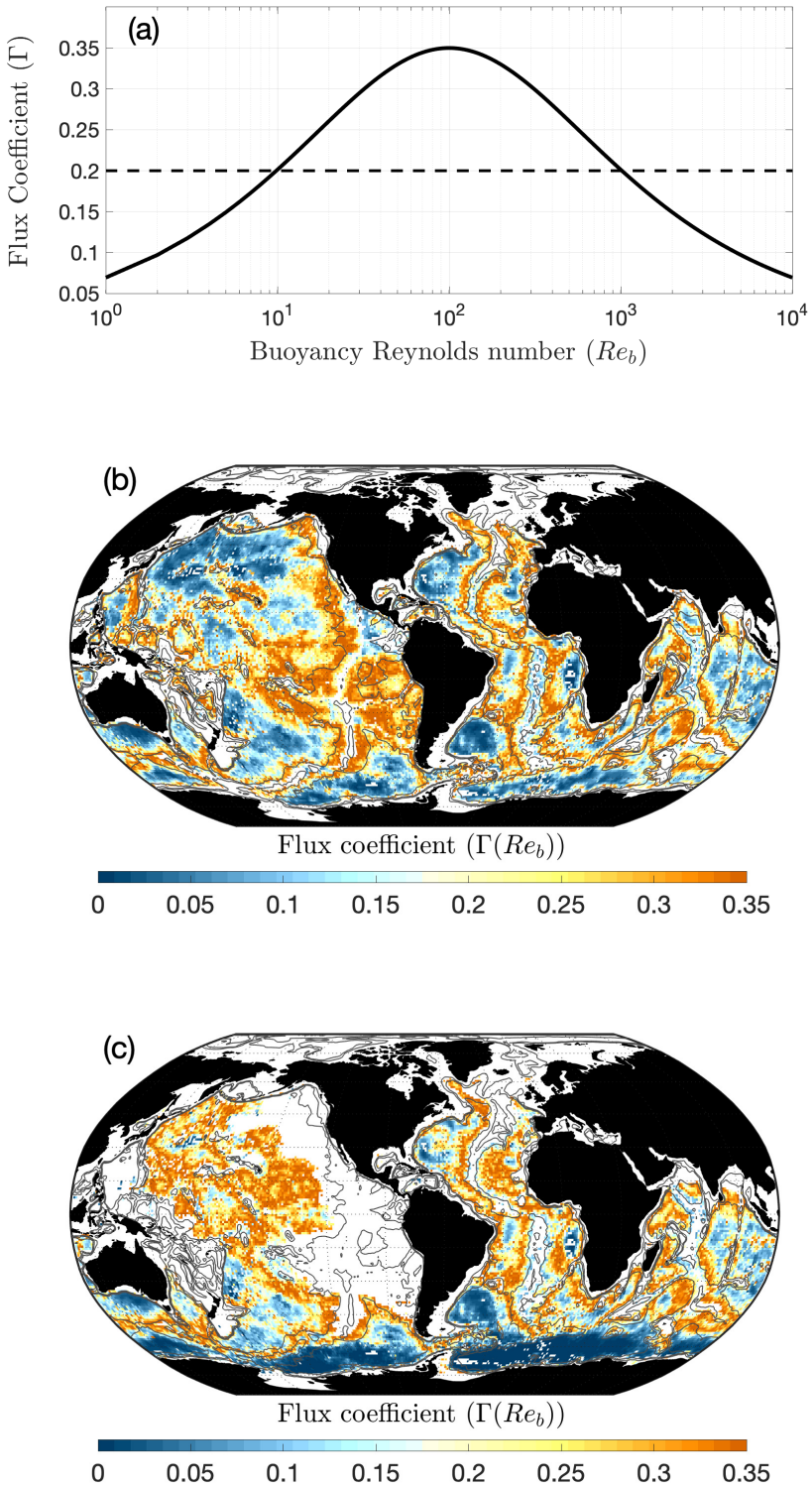


Figure 3.3: *(a) Parameterisation for the flux coefficient as a function of the buoyancy Reynolds number (following Mashayek* et al. *(2017c)), with* $Re_b^* = 100$ *and* $\Gamma^*(Re_b^*) = 0.35$. *(b) Global map of the flux coefficient* $\Gamma(Re_b)$ *at 3000 m, and (c) on the density surface* $\gamma^n = 28.1$. *The flux coefficient has been calculated by applying the parameterisation in conjunction with a variable* $q_t(x, y)$ *as shown in figure 3.2c, and global hydrographic stratification* (N^2) *from WOCE climatology. (d) Global zonal average of* $\Gamma(Re_b)$ *and neutral density surfaces in the deep ocean.*

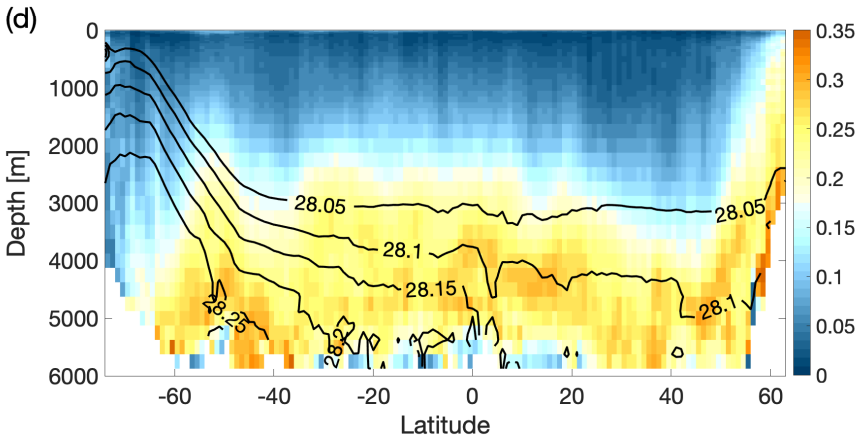


Figure 3.3 continued

3.2.3 Inferring mixing

As described in chapter 2, it is difficult to directly measure diapycnal mixing given its small scales and its highly heterogeneous spatial and temporal nature (Smyth & Caldwell, 2001; Thorpe, 2007). Therefore, diapycnal mixing is often approximated from estimates of the dissipation rate and knowledge of the flux coefficient, as described in equation 2.24, repeated below for convenience:

$$\mathcal{H}_{3D} \approx \mathcal{M} \approx -\frac{g}{\rho_0}\overline{w'\rho'} \approx \Gamma\epsilon \tag{3.4}$$

where $-(g/\rho_0)(\overline{w'\rho'})$ is the turbulent buoyancy flux due to correlations between w' and ρ', which are turbulent fluctuations in velocity and density, respectively, on time scales shorter than that of the average expressed by the overbar (Ferrari *et al.*, 2016). It is assumed that the average is taken over a sufficiently long period that reversible components of the buoyancy flux cancel out, and that the horizontal components of the buoyancy flux are negligible. Therefore, diapycnal mixing $\mathcal{M}$ can be expressed, in an approximative way, as a fraction of ϵ, with Γ as the coefficient connecting the two variables (Osborn, 1980). Note that in the calculation of the buoyancy flux $\mathcal{M}$ we also include the contribution of geothermal heat flux, from the estimate of Davies & Davies (2010). The geothermal heat flux from the

Earth's interior at the meeting points of tectonic plates contributes to the transformation of dense abyssal waters into lighter waters (Mashayek *et al.*, 2013*b*; de Lavergne *et al.*, 2016).

There are a few simple steps needed to estimate (i) the dissipation rate ϵ, from the energy generated by locally breaking waves E_{loc}, and (ii) the flux coefficient Γ (in the case of non-constant Γ) from knowledge of ϵ and of the buoyancy Reynolds number Re_b. First, by noticing that E_{loc} represents the local energy available to turbulence, i.e. the sum $(\mathcal{M} + \epsilon)$, and that $\mathcal{M}$ can be rewritten as in equation 3.4 as $\mathcal{M} \approx \Gamma\epsilon$, it is possible to derive an expression for the dissipation rate:

$$\epsilon = \frac{E_{loc}}{\Gamma + 1}. \tag{3.5}$$

This expression itself depends on the flux coefficient, and it is therefore solved in a short iterative loop: from a first initial guess of Γ, we calculate a first estimate of ϵ, used to calculate Re_b, which is used to re-calculate (update) Γ. This loop is repeated until Γ converges, i.e. at each location the variation between the previous estimate and the last one is smaller than 10^{-6}, assuming that variations in Γ of that order are negligible. Figures 3.4a and 3.4b show the energy from locally breaking waves E_{loc} and the dissipation rate ϵ at the depth of 3000 m calculated by using a variable dissipation efficiency $q_t(x, y)$ and a variable flux coefficient $\Gamma(Re_b)$. E_{loc} is enhanced close to complex topographic structures (i.e. where the energy conversion into either internal tides or lee waves is strong), but takes into account also the spatial variability of the local breaking efficiency; for example, it returns relatively lower values in the Eastern Pacific, where $q_t(x, y)$ is small. The dissipation rate (figure 3.4b) shows that turbulence is enhanced in the proximity of regions of rough topography, i.e. where both E_{loc} and $\Gamma(Re_b)$ are larger.

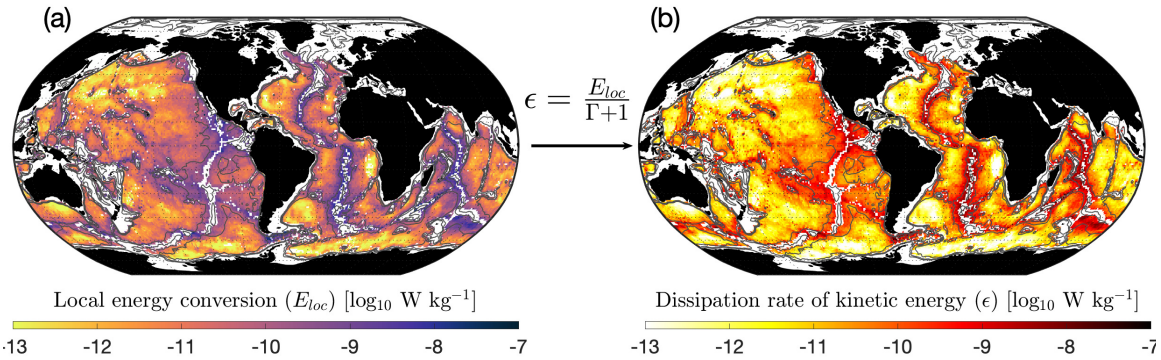


Figure 3.4: *(a) Global map of locally breaking energy, E_{loc}, at 3000 m (log scale). (b) Global map of turbulent dissipation rate ϵ at 3000 m inferred from the global map of E_{loc} by using the relationship shown. Both panels have been produced using the spatially variable breaking efficiency $q_t(x, y)$ shown in figure 3.2b and a spatially variable flux coefficient $\Gamma(Re_b)$ shown in figure 3.3b.*

3.3 Internal wave local breaking efficiency and flux coefficient co-variation: effects on diapycnal mixing

The sensitivity of turbulent mixing to the simultaneous variation of q_t and the flux coefficient Γ is described here by analysing several cases. The case in which both q_t and Γ are constant and equal to the canonical values $q_t = q_g = 0.3$ and $\Gamma = 0.2$ is taken to be the control case, (*ctrl*). First, the effect of a larger fraction of local wave breaking is analysed in a set of cases in which q_t is kept constant but equal to the global average of the spatially variable $q_t(x, y)$, i.e. $q_+ = \langle q_t(x, y) \rangle = 0.6275$. Two cases are run with a larger q_t, namely:

- (q_+), in which the flux coefficient is kept constant, $\Gamma = 0.2$;
- ($q_+\Gamma$), in which the flux coefficient is parameterised as $\Gamma(Re_b)$ as described in section 3.2.2.

Subsequently, two other cases are run to investigate the impact of a spatially variable $q_t(x, y)$, in combination with a constant or variable flux coefficient:

- (q_{var}), in which q_t is spatially variable, as shown in figure 3.2b, and the flux coefficient is constant, $\Gamma = 0.2$;

- ($q_{var}\Gamma$), in which q_t is spatially variable and the flux coefficient is parameterised as $\Gamma(Re_b)$.

The turbulent mixing $\mathcal{M}$ for the (*ctrl*) case is shown in figure 3.5a on the neutral density surface $\gamma^n = 28.1$ (the zonal average of which is shown in figure 3.3d), showing that here mixing is particularly large close to topographic ridges and where the density surface is in contact with the bottom. However, whether mixing is going to change the density of these waters depends on the vertical divergence of the turbulent mixing: if mixing is homogeneous, i.e. it does not vary in the vertical, there is no convergence or divergence of water masses and no net water mass transformation. On the contrary, if there is a vertical variation in $\mathcal{M}$, i.e. if mixing is non-homogeneous, it follows that there is a convergence or divergence of water masses, which move at the diapycnal velocity (from Ferrari *et al.* (2016)):

$$\tilde{\mathbf{e}} \approx \frac{\partial_z \mathcal{M}}{\partial_z b}, \tag{3.6}$$

where $b = -g/\rho_0 \, \delta\rho$ is the buoyancy. A positive $\tilde{\mathbf{e}}$ indicates diapycnal upwelling, i.e. water becomes lighter, while a negative $\tilde{\mathbf{e}}$ indicates diapycnal downwelling, i.e. water becomes denser. The diapycnal velocity for the (*ctrl*) case is shown in figure 3.5b, showing that upwelling is happening close to the ridges (magenta), while downwelling is happening in the ocean interior (cyan), as described in previous studies De Lavergne *et al.* (2016); Ferrari *et al.* (2016). For turbulent mixing to raise dense waters to shallower depths, the residual from the sum of the along-boundary upwelling and interior downwelling has to be positive, indicating a net lightening of dense water masses. The calculation of the total water mass transformation from these contributions is discussed later and shown in figure 3.6. Note that while previous studies (e.g. De Lavergne *et al.* (2016); Ferrari *et al.* (2016); McDougall & Ferrari (2017)) comment on the patterns of the diapycnal velocity and their net effect on the water mass transformation, they do not show or focus on the spatial variability of the diapycnal velocities, as it is done here.

The differences in diapycnal velocity between the different cases are shown in figure 3.5c-3.5j over the neutral density surface $\gamma^n = 28.1$. These panels show differences in diapycnal upwelling (3.5c,e,g,i) and diapycnal downwelling (3.5d,f,h,j). Positive anomalies in diapycnal upwelling indicate enhanced upwelling, while negative anomalies in diapycnal downwelling indicate enhanced downwelling (note that the diapycnal velocity changes sign between different cases in only very few points).

An increase in the fraction of the internal waves breaking locally, case (q_+), returns both a larger upwelling (positive anomalies in figure 3.5c) and a larger downwelling (negative anomalies in figure 3.5d), meaning that turbulent mixing raises deep waters to shallower depths at a faster rate, and sinks waters at a faster rate. The larger diapycnal velocities are a direct consequence of the fact that a larger constant q_t means that a larger fraction of internal waves breaks locally, leading to a larger dissipation rate, and so to enhanced upwelling and downwelling. By employing a variable flux coefficient $\Gamma(Re_b)$ with a larger constant q_t, in the case ($q_+\Gamma$), the anomalies in the diapycnal velocities return a much larger spatial variability: given that the spatial changes cannot be attributed to the change in q_t, since this is still kept constant and simply contributes to changing the rate at which waters are transformed, the spatial changes must be attributed to the spatial variability in the flux coefficient. In particular, these anomalies show the regions where $\Gamma(Re_b)$ is larger than 0.2 (areas of larger upwelling or downwelling), and regions where $\Gamma(Re_b)$ is smaller than 0.2 (areas of weaker upwelling or downwelling). For example, figure 3.5f indicates that $\Gamma(Re_b)$ is smaller than 0.2 along the eastern side of the Mid-Atlantic Ridge, along the western side of the ridge in the Indian Ocean, and in several regions in the Pacific Ocean, especially where the density surface is in contact with the bottom. The spatial distribution $\Gamma(Re_b)$ on the isopycnal $\gamma^n = 28.1$ is shown in figure 3.3c.

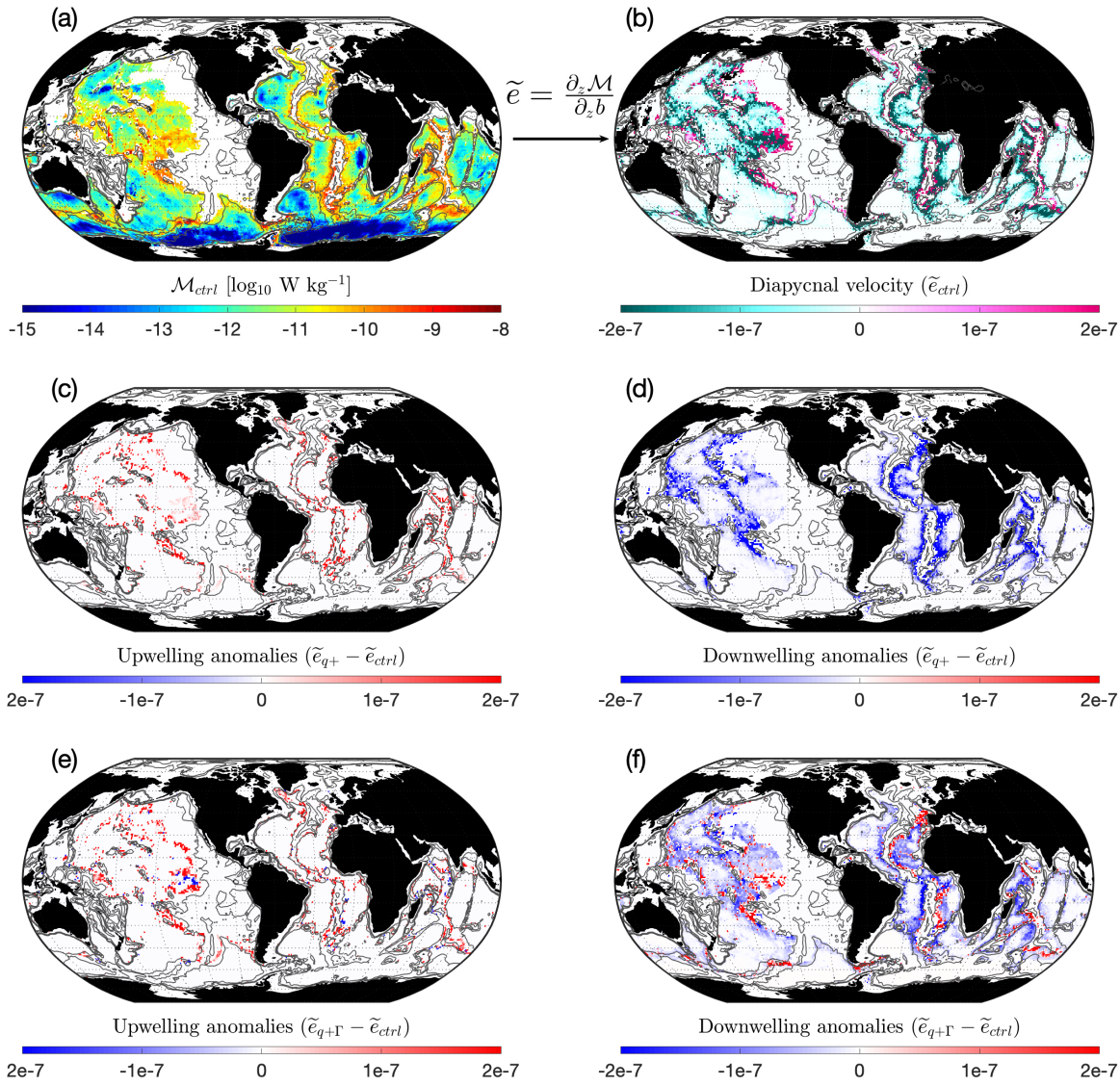


Figure 3.5: *(a) Turbulent mixing (log scale) over the neutral density surface* $\gamma^n = 28.1$ *for (ctrl) case, i.e.* $q_t = q_g = 0.3$, $\Gamma = 0.2$. *All the following panels are on the same neutral density surface. (b) Diapycnal velocity* $\tilde{e}$ *for case (ctrl). (c-d) Differences in (c) upwelling and (d) downwelling between case* (q_+) *and (ctrl). (e-f) Differences in (e) upwelling and (f) downwelling between cases* ($q_+\Gamma$) *and (ctrl). (g-h) Differences in (g) upwelling and (h) downwelling between cases* (q_{var}) *and (ctrl). (i-j) Differences in (i) upwelling and (j) downwelling between cases* ($q_{var}\Gamma$) *and (ctrl).*

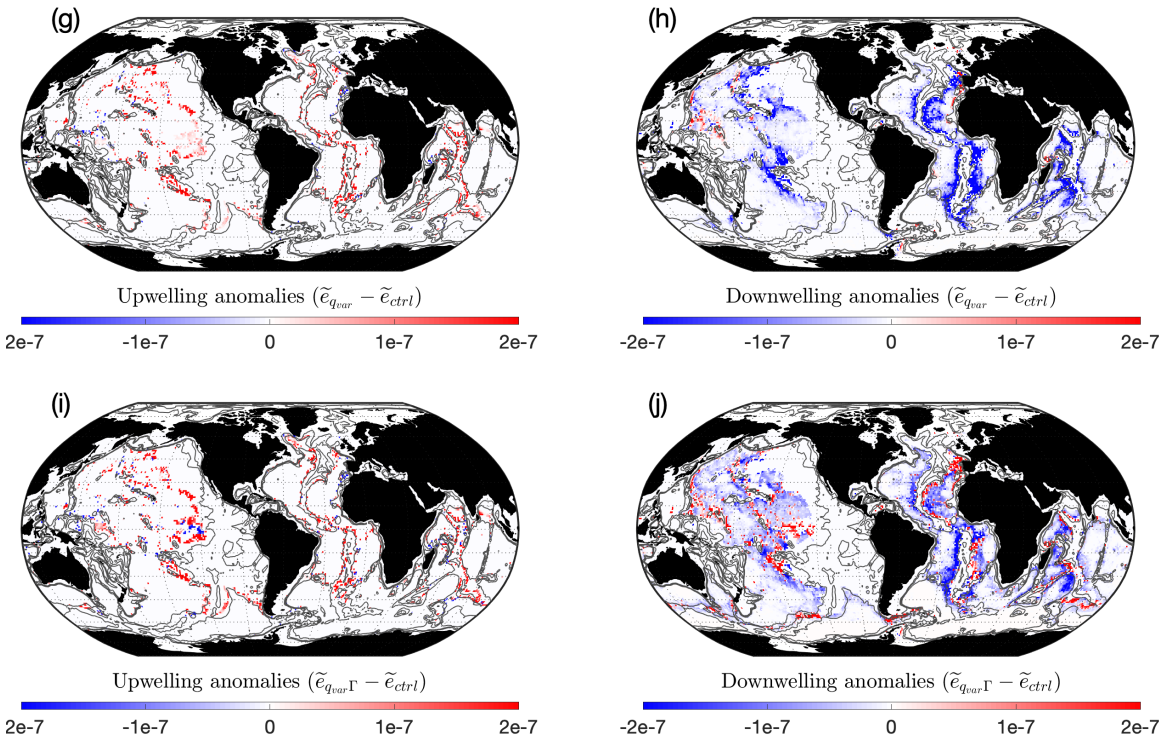


Figure 3.5 continued

The impact of a spatially variable $q_t(x, y)$ on the diapycnal velocities is shown in figures 3.5g-j. The comparison of the (*ctrl*) case with the (q_{var}) case allows to identify the regions where the spatially variable q_t is smaller than 0.3, i.e. the regions where diapycnal upwelling and downwelling are weaker than in the (*ctrl*) case. These regions are located especially in the western Pacific Ocean and in the eastern Atlantic Ocean. When allowing the flux coefficient to vary as well, instead of relying on a constant value, we expect it to vary closely with $q_t(x, y)$: changes in q_t alter the amount and the spatial variation of energy from locally breaking waves E_{loc}, and consequently of the energy available to turbulent mixing and dissipation, leading to changes in the buoyancy Reynolds number, and so in the flux coefficient. The differences between this scenario ($q_{var}\Gamma$) and the (*ctrl*) case are shown in figures 3.5i,j. The anomalies in the diapycnal velocities in these two cases combine the effects of a spatially variable q_t (shown in figures 3.5g,h) and of a spatially variable flux coefficient (shown in figures 3.5e,f). The anomalies shown in figures 3.5i,j are

almost identical to the anomalies in figures 3.5e,f, indicating that the spatial variability in $\Gamma(Re_b)$ dominates over the variability in q_t in setting the spatial variability of the patterns of upwelling and downwelling of dense waters. Also, changes in q_t return mainly uniform but larger rates of diapycnal upwelling/downwelling, while the much larger spatial variability in the diapycnal velocities in the cases ($q_+\Gamma$) and ($q_{var}\Gamma$) implies that changes in $\Gamma(Re_b)$ tend to compensate for the excess in local energy available to turbulence when using a larger q_t, with implications for the strength of the deep ocean circulation and for tracer distribution.

To quantify the effect of such differences in the patterns of upwelling and downwelling on the ocean circulation, and especially on the rising of deep waters back to shallower depths, the total water mass transformation is calculated for the different cases on different density surfaces. The results shown here present three of the cases described above, namely the (*ctrl*) case and the two cases with a spatially variable local dissipation efficiency, (q_{var}) and ($q_{var}\Gamma$). The global integrated water mass transformation rate in the cases with larger but constant q_t is similar to the cases with spatially variable $q_t(x, y)$ and so is not shown here. For a given density surface, the total water mass transformation is given by the integral of the diapycnal velocity $\tilde{\mathbf{e}}(\rho)$ over that surface:

$$D(\rho) = -\iint_A \tilde{\mathbf{e}}(\rho) \cdot \mathbf{n}\, dA \tag{3.7}$$

where $\mathbf{n}$ is the unit vector normal to the density surface, A is the surface area of the density surface, and the minus sign is used such that water mass transformation is positive when water goes from denser to lighter (following Ferrari *et al.* (2016)). The water mass transformation is measured in Sverdrups.

Figure 3.6a shows the total global water mass transformation, i.e. the residual of the along-boundary upwelling and interior downwelling, for the three cases analysed here. As expected, the residual is positive, indicating that the net contribution of diapycnal mixing is to transform dense water into lighter water, therefore contributing to the raising of deep

waters back to the surface.

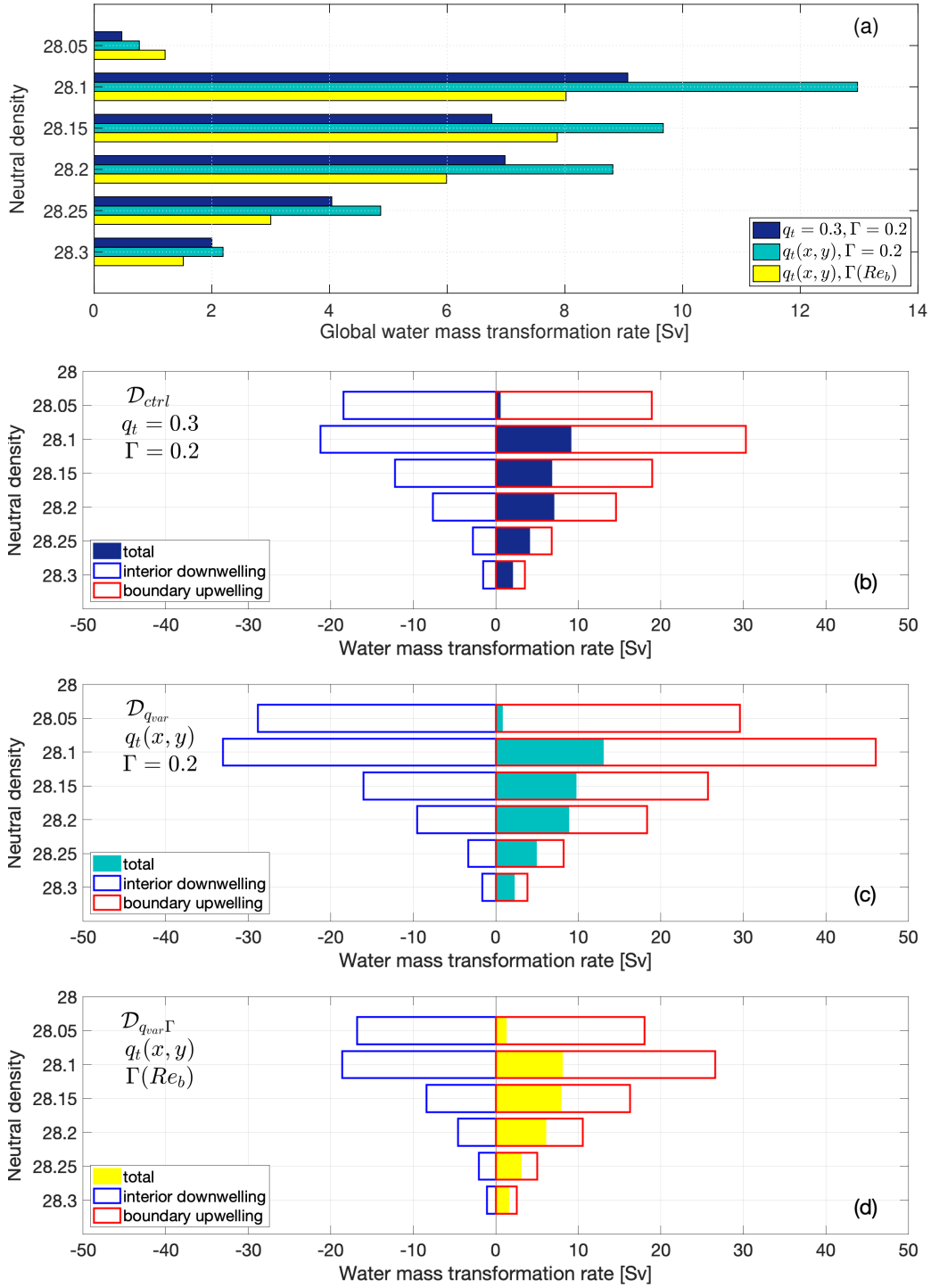


Figure 3.6: *(a) Total global water mass transformation (i.e. net of along-boundaries upwelling and interior downwelling) for the three cases investigated here. (b) Total water mass transformation (filled bars, same colors as panel a) dissected into upwelling along boundaries (red bars) and interior downwelling (blue bars) for the (ctrl) case. (c-d) Same as in panel b, but for the cases (q_{var}) and ($q_{var}\Gamma$).*

The water mass transformation indicates how much, for each of the neutral density layers analysed here, water is transformed into lighter density classes. In a steady-state ocean, this corresponds to the overturning rate of the lower cell, assuming that its strength depends only on diapycnal mixing. The cases analysed here return a rate of overturning of the lower cell of 8-13 Sv approximately, thus smaller than the ~20 Sv returned from inverse estimates (e.g. Lumpkin & Speer (2007)). However, the contribution of far-field mixing is not taken into account here, and other processes could contribute to mixing in the deep ocean (see for example the next section on the contribution from near-inertial waves).

Figure 3.6a also shows that case (q_{var}) returns a larger water mass transformation rate, up to 1/4-1/3 larger than in the other cases, not surprising given the larger fraction of the global internal wave energy dissipating locally in this cases. Cases (*ctrl*) and ($q_{var}\Gamma$), on the other hand, return similar water mass transformation values, which is a quite fortuitous result. Indeed, the fact that a variable flux coefficient compensates for the enhancement in turbulence caused by a variable $q_t(x, y)$ brings the two estimates of net water mass transformation close together. However, understanding the role of turbulent mixing in the ocean circulation is not just about getting the globally integrated water mass transformation right. As shown in figure 3.5, the patterns of upwelling and downwelling are different in the different cases, and depend on the joint effect of both a variable q_t and a variable $\Gamma(Re_b)$.

Changes in the rates of total global upwelling and total global downwelling for the different cases are quantified in figures 3.6b-3.6d, which shows the distinct contribution of along-boundary upwelling (red bars) and interior downwelling (blue bars), as well as the residual water mass transformation (filled bars, color-coded following figure 3.6a). Case (q_{var}) returns much larger rates of upwelling and downwelling, up to 50% larger than cases (*ctrl*) and ($q_{var}\Gamma$), consistent with the results shown in figure 3.5g,h. On the contrary, cases (*ctrl*) and ($q_{var}\Gamma$) return similar values of global rates of upwelling and downwelling. This is interesting, given that figure 3.5i,j shows that the patterns of diapycnal upwelling and downwelling are significantly different between the two cases. These results indicate that

the water mass transformation rates are sensitive to the choice of the rate of local breaking and the flux coefficient in non-linear ways, and that the two parameters should be varied together to avoid overestimating the rates of diapycnal upwelling and downwelling.

The contribution of the different ocean basins to the total water mass transformation, as well as to the diapycnal upwelling and downwelling, is shown in figure 3.7 for the case ($q_{var}\Gamma$). This is the only case shown given that the other two cases, (*ctrl*) and (q_{var}), are qualitatively similar. The (*ctrl*) case is also quantitatively close to the results shown in figure 3.7, with differences of only 2-3 Sv between the two cases for the different ocean basins. Figure 3.7a shows the area of density surfaces considered here (namely, $\gamma^n = 28.05 - 28.3$) and the regions over which the water mass transformation is calculated in figure 3.7b, namely in the Atlantic, Pacific and Indian basin north of 32°S, while the Southern Ocean is considered a distinct region. Figure 3.7b shows that the Pacific and Atlantic Oceans are the main contributors to the global water mass transformation rate for density classes lighter than $\gamma^n = 28.15$. The Indian Ocean has a relatively important contribution for light density classes, but it does not contribute to any diapycnal upwelling for $\gamma^n \geq 28.2$ and to any diapycnal downwelling for $\gamma^n \geq 28.25$. Also the Atlantic and Pacific Oceans do not contribute (or contribute only minimally) to the water mass transformation at density classes denser than 28.25, while the Southern Ocean plays a dominant role for density classes denser than $\gamma^n = 28.2$. The net water mass transformation is negative in the Southern Ocean for light density classes, a point that will be discussed in more detail in the next section.

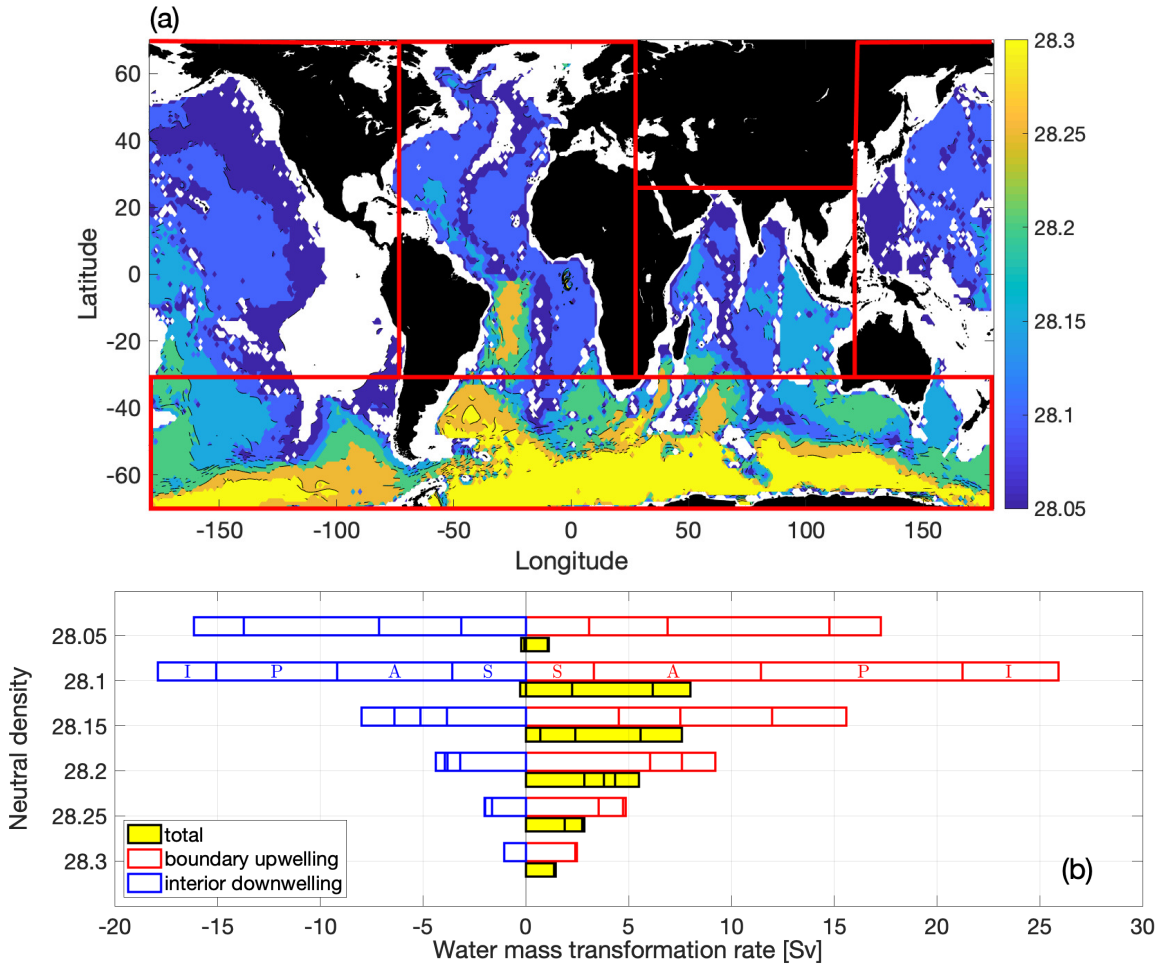


Figure 3.7: *(a) Area of the neutral density surfaces over which the water mass transformation rate is calculated in panel (b). The red boundaries are used to indicate the regions over which the water mass transformation has been calculated. The Southern Ocean is considered the region south of 32°S. (b) Water mass transformation (total and dissected into along-boundary upwelling and interior downwelling) in different ocean basins, namely Southern (S), Atlantic (A), Pacific (P) and Indian (I) Oceans. Labels are reported only for the neutral density surface* $\gamma^n = 28.1$ *but the same arrangement is applied to all density surfaces, in the same order from the x-axis origin.*

3.3.1 Contribution of different mixing-generating processes

Further to understanding how the diapycnal velocities respond to changes in the q and Γ parameters, and which basins contribute most to the net water mass transformation, it is meaningful to investigate the importance of internal tides, lee waves and the geothermal heat flux in contributing to the net buoyancy flux responsible for the water mass transformation shown here. The results are shown in figure 3.8: the net water mass transformation

rate for the three different cases is split into three bars, indicating the contribution of the three processes taken into account here; this calculation is repeated for the global ocean and for the Southern Ocean only, i.e. south of 32°S.

Internal tides are the largest contributor to the net global water mass transformation, especially for density surfaces lighter than $\gamma^n = 28.2$ (left panels in figure 3.8). For denser density surfaces, the contribution of lee waves is comparable with (i.e. close to, or in some cases even larger than) that of internal tides. The geothermal heat flux (ghf in the figure legend) contributes to a maximum of ~ 4 Sv of water mass transformation (in agreement with previous studies, such as Adcroft *et al.* (2001); Scott *et al.* (2001); Emile-Geay & Madec (2009); Mashayek *et al.* (2017*a*)) on the density surface $\gamma^n = 28.1$, playing a non negligible role in regulating the lower MOC cell. The comparison between the water mass transformation rates in the global ocean and in the Southern Ocean raises a few interesting points.

First, the contribution of lee waves to the global water mass transformation is dominated by the transformation rate in the Southern Ocean for density surfaces denser than $\gamma^n = 28.15$ (note that the left and right panels in figure 3.8 have different x-axes). This result follows from the fact that most of the energy conversion into lee waves takes place in the Southern Ocean, as shown in figure 3.2. Given that the same local dissipation efficiency, $q_g = 0.3$, has been used in the different experiments, the contribution of lee waves does not change between the (*ctrl*) and (q_{var}) cases. The increase in the net global water mass transformation for the case (q_{var}) shown in figure 3.6 is caused, therefore, only by a larger contribution from internal tides. On the other hand, case ($q_{var}\Gamma$) shows a smaller contribution from lee waves, caused by the change in the flux coefficient. Given that lee waves are dominant in the Southern Ocean, and that their contribution decreases with a variable flux coefficient, this reflects the fact that $\Gamma(Re_b)$ is smaller than 0.2 in the Southern Ocean (see figure 3.3).

Interestingly, lee waves contribute to a net *downwelling* for density surfaces lighter than

$\gamma^n = 28.15$ in the Southern Ocean, and lighter than $\gamma^n = 28.05$ in the global ocean. A net downwelling indicates that the along-boundary upwelling is not large enough to compensate for the downwelling in the ocean interior, which is caused by an increase of diapycnal mixing in proximity of the ocean sea-floor. Lee wave energy conversion (figure 3.2) depends mainly on the strength of bottom currents (Nikurashin & Ferrari, 2011) and less on the presence of topographic structures. This could explain why a net upwelling is found only for denser density classes: density classes from $\gamma^n = 28.2$ and below are closer to the ocean bottom, and so more strongly interact with ridges and hills, generating more along-boundary upwelling than interior downwelling; lighter density classes, however, do not interact with topographic features as much, and there is not sufficient energy into lee waves close to the boundaries to generate enough upwelling to compensate for the downwelling in the ocean interior. Light density surfaces are not shown here, given that the focus is on the sensitivity of mixing in the deep ocean, but lee waves contribute to a net diapycnal downwelling for all the density surfaces lighter than $\gamma^n = 28.15$ analysed (the analysis stopped at $\gamma^n = 27.2$). A net diapycnal downwelling from lee waves is found also in the global water mass transformation for density surfaces lighter than $\gamma^n = 28.05$, suggesting that here the presence of ridges allows lee wave-driven diapycnal upwelling to compensate for the interior downwelling up to slightly shallower depths. This result indicates the crucial role of boundaries and continental shelf in creating corridors for the dense waters to come back to shallower depths. It also indicates that different processes can have opposite contributions to the net water mass transformation on the same density surface, and so it is important to not exclude relevant processes from the picture. On this point, a brief discussion on the role of near-inertial waves is included in the next section.

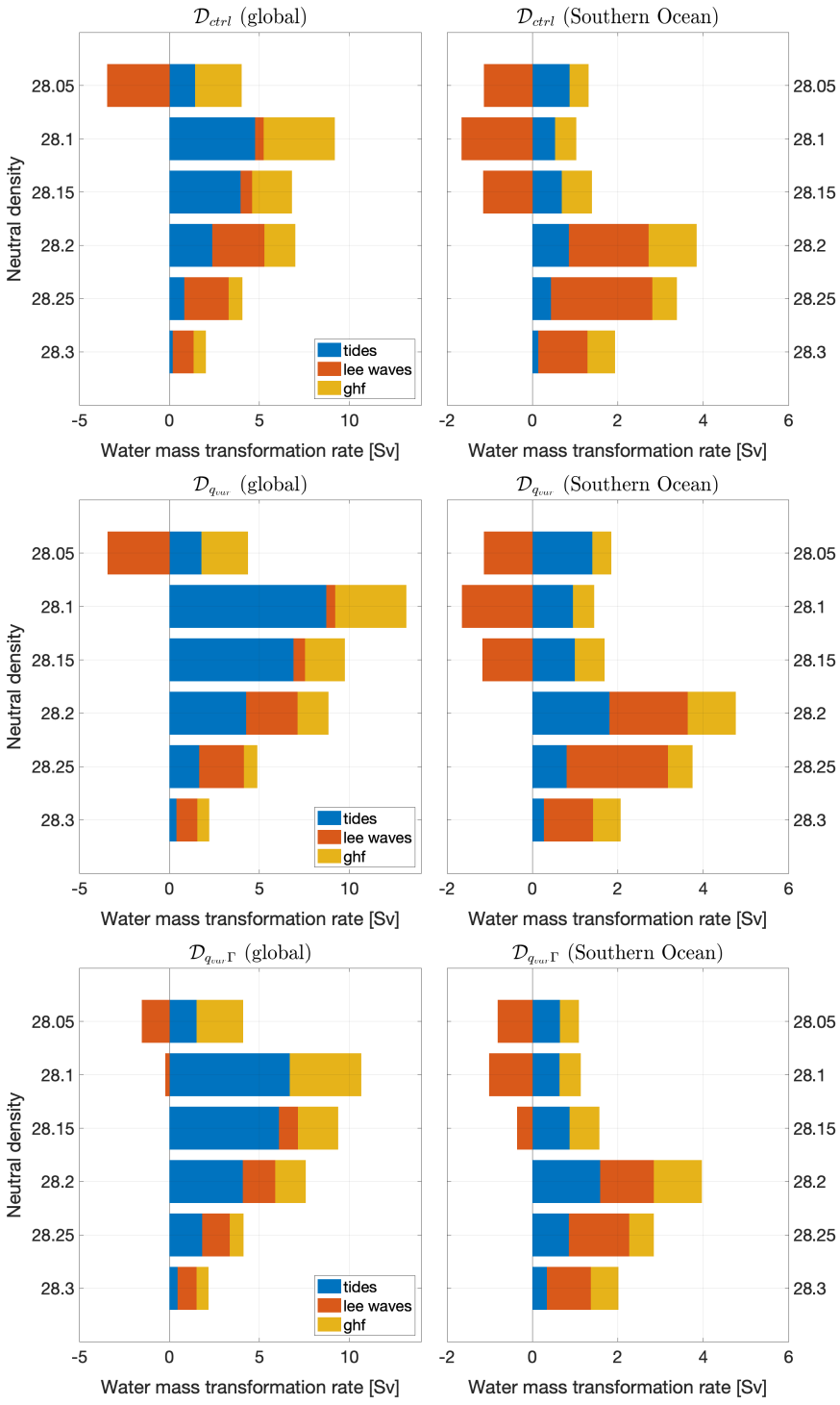


Figure 3.8: *Water mass transformation rate in the (left) global ocean and (right) Southern Ocean for the three cases ((ctrl), (q), and (qΓ) from the top to the bottom). In each panel, the net water mass transformation is split into the contribution of (blue) internal tides, (red) lee waves and (yellow) geothermal heat flux (ghf). Note that the panels on the left have a different x-axis than the panels on the right.*

3.3.2 A brief comment on the contribution of near-inertial waves

In the analysis presented above only internal tides and lee waves have been considered as sources of diapycnal mixing from the breaking of internal waves. While they are indeed primary sources of mixing in the deep ocean (Munk & Wunsch, 1998; Nikurashin & Ferrari, 2013; MacKinnon *et al.*, 2017), there are other sources that can potentially play an important role, such as near-inertial waves. The aim of this section is to briefly comment on the role of near-inertial waves in mixing the deep ocean, and especially on their contribution to sustaining the lower cell of the MOC.

Near-inertial waves (see section 3.1), are known to be generated by several processes whose relative importance is yet to be established. While the wind stress at the surface of the ocean is a key mechanism in the generation of near-inertial waves, it is not clear how fast such waves decay in the ocean interior. Here, the contribution of near-inertial waves to the net global water mass transformation is tested by comparing different decay scales.

Here we use the annual mean energy flux from the wind into near-inertial waves at the surface of the ocean from Alford (2003), shown in figure 3.9a. The energy flux is larger in the mid-latitude regions, and particularly on the western side of the ocean basins, associated with winter storms (Alford, 2001, 2003). A good fraction of this energy is estimated to be dissipated within the mixed layer, therefore contributing to mixing only in the upper 100 m (taken as an approximate global ocean, annual mean mixed layer depth, e.g. de Boyer Montégut *et al.* (2004)). The diapycnal mixing generated by near-inertial wave energy in the ocean interior depends on the amount of energy that makes it through the mixed layer, and that does not radiate away horizontally. Crawford & Large (1996) estimated that 70%-80% of the near-inertial energy is dissipated in the mixed layer, and Furuichi *et al.* (2008) found that approximately half of the energy that makes it through the mixed layer radiates away (Jochum *et al.*, 2013). Therefore, based on such estimates, only 15% of the energy at the ocean surface makes it below the mixed layer, below which

it decays. Jochum *et al.* (2013) assumed a decay function, with an e-folding scale of 2000 m, based on the results of Alford & Whitmont (2007), which showed a very slow decay of such energy in the ocean interior from mooring observations. However, all these estimates are still very much uncertain (Alford *et al.*, 2016).

Here, the contribution of the near-inertial waves has been added to the estimates of the net, global water mass transformation, assuming that only 15% of the energy at the surface makes it into the ocean interior, while different possible decay scales have been tested. Figure 3.9b shows the total water mass transformation, calculated by taking into account the contribution of internal tides, lee waves, near-inertial waves, and geothermal heat flux. The results are presented only for the case ($q_{var}\Gamma$), but they are qualitatively similar to the other ($ctrl$) and (q_{var}) cases. The results presented in figure 3.9b show that the global water mass transformation is hugely dependent on the decay scale chosen for near-inertial waves. With a sharper decay scale, 500 m, near-inertial waves do contribute to some water mass transformation in the upper ocean, but have a very limited impact in the deep ocean, where internal tides and lee waves dominate. On the contrary, with a smoother decay scale of 2000 m, near-inertial waves play a large role in the deep ocean, strongly enhancing the water mass transformation here, contributing to more than doubling the water mass transformation for the density classes characteristic of the lower cell of the MOC. Observation-constrained inverse models (Lumpkin & Speer, 2007), the Estimating the Circulation and Climate of the Ocean (ECCO) state estimate (Cessi, 2019), and estimates of diapycnal mixing from hydrographic sections (Kunze, 2017*a*) all estimate a maximum transport of $\sim$ 20 Sv for the lower cell of the MOC. The inverse estimate of Talley *et al.* (2003) returns a maximum transport up to 29 Sv. Comparing these estimates with the water mass transformation rates calculated above suggest that internal tides, lee waves and geothermal heat flux are not sufficient to fully describe the strength of the lower cell (with the caveat that we are not including the contribution of far-field mixing), and near-inertial waves can play a significant role. An in-depth investigation on near-inertial wave impacts on deep diapycnal mixing

and the lower MOC is beyond the scope of this work, but the analysis above shows that near-inertial waves can potentially play a significant role also in the deep ocean. A key step will be to better quantify, from observations and high resolution models, how rapidly such waves decay from the surface to the deep ocean.

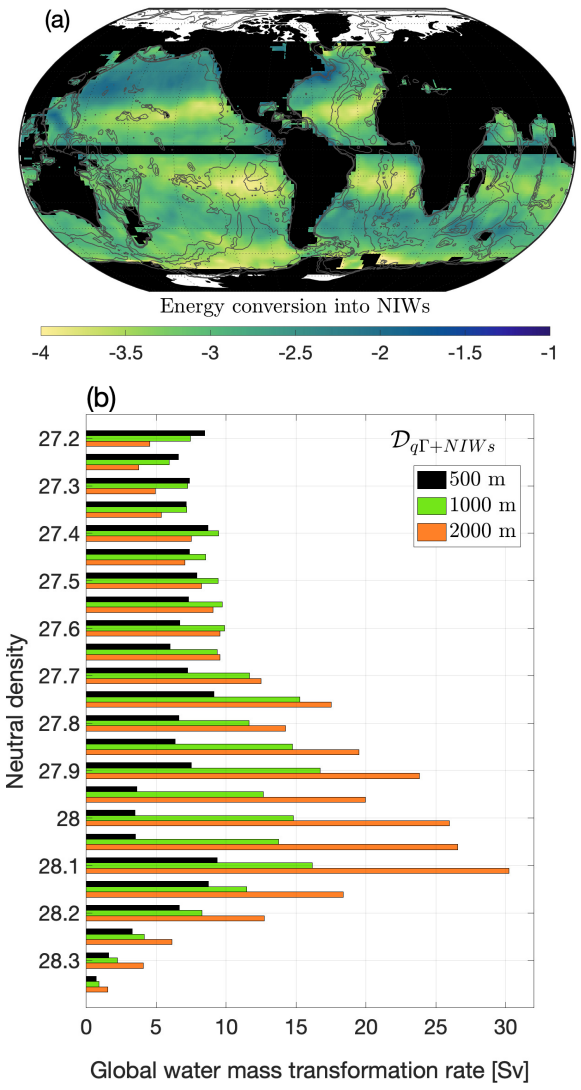


Figure 3.9: *(a) Annual mean energy flux from the wind into near-inertial waves (log scale), reproduced from Alford (2003). (b) Total global water mass transformation rate including the contribution of internal tides, lee waves, geothermal heat flux and near-inertial waves for the case* ($q\Gamma$)*. The different colors show the sensitivity of the water mass transformation to different decay scales for the near-inertial waves component.*

3.4 Summary and conclusions

In this chapter, we used estimates of the internal wave (internal tides and lee waves) energy flux and radiation, together with the geothermal heat flux, to infer the amount of diapycnal mixing in the deep ocean, the patterns of diapycnal upwelling/downwelling and the rate of mixing-driven water mass transformation across the lower cell of the MOC.

In particular, we have investigated the sensitivity of internal wave-induced mixing to spatially variable local breaking efficiency q and turbulent flux coefficient Γ, parameters representing the global to local energy pathway from internal waves to diapycnal mixing. In ocean and climate models that do not resolve the internal wave field, these parameters are often assumed to be constant due to lack of knowledge of their spatial variations. However, the use of constant q and Γ does not allow to take into account the different regimes of internal wave generation, which lead to different wave radiation, and the fact that mixing is non-homogeneous but depends on the ocean stratification and turbulence.

The work presented here builds on previous studies and aims at exploring the non-linear response of diapycnal mixing when multiple parameters are varied *in tandem*. In particular, we use the map of spatially variable $q_t(x, y)$, the internal-tide local breaking efficiency, from Vic *et al.* (2019). Indeed, the (common) choice of $q_t = 0.3$, derives from earlier estimates of the tidal energy flux at a few select topographic regions, which inevitably cannot be representative of the global ocean nor can they account for a variety of small-scale processes (St Laurent *et al.*, 2002; St Laurent & Garrett, 2002; Egbert & Ray, 2003). Recent observational- and model-based estimates have highlighted the strong spatial heterogeneity of q_t (e.g. Waterhouse *et al.* (2014); Lefauve *et al.* (2015); Vic *et al.* (2019)) and idealised model studies have shown that the ocean state is sensitive to the distribution of internal tide energy between the near-field and far-field (Melet *et al.*, 2016).

The implications of a spatially variable $q_t(x, y)$ on the internal wave-driven mixing and the overturning rate of the lower cell of the MOC have not been investigated before. Here

we do so in combination with either a constant or variable flux coefficient, following the parameterisation for Γ from Mashayek *et al.* (2017*c*). The effect of a variable flux coefficient, represented as a non-monotonic function of the buoyancy Reynolds number, have been investigated before, but not in combination with other parameters (de Lavergne *et al.*, 2016; Mashayek *et al.*, 2017*c*). Given the non-linearity of the problem, and the impact that $q_t(x, y)$ can have on the estimates of local turbulence, and hence on Γ, it is useful to investigate the sensitivity of mixing to a co-variation of these parameters. Therefore, the work presented here contributes to a better understanding of the impact of different parameters on the internal wave-driven mixing, on the net overturning rate of the lower MOC cell and on the role played by different processes in generating the mixing that regulates the overturning of this cell.

Our results show that a co-variation of q_t and Γ has important consequences on both the geographical variations of the diapycnal velocity (i.e. for the patterns of upwelling and downwelling of water masses) and for the water mass transformation rate. We show that turbulent mixing is highly sensitive to the choice of q_t and Γ made, and responds in non-linear ways to a simultaneous variation of the two parameters.

First, changing only q_t, either with a constant (case (q_+)) or spatially variable (case (q_{var})) values, while keeping Γ constant, returns much larger values of both upwelling and downwelling, and a larger total water mass transformation. This results is straightforward: a larger (constant or variable) q_t leads to an increase of energy available to turbulence, hence to larger diapycnal mixing and so to a larger overturning rate. However, when applying a variable flux coefficient $\Gamma(Re_b)$, the increase in energy is compensated by changes in the flux coefficient, indicating that the two parameters should be co-varied so as not to overestimate the rates of diapycnal upwelling/downwelling and the water mass transformation rate. Also, when using constant parameters, $q = 0.3$ and $\Gamma = 0.2$, the globally-integrated and individual basin water mass transformation rates are fortuitously similar to the rates obtained with geographically variable $q_t(x, y)$ and $\Gamma(Re_b)$. This indicates that the water

mass transformation, while useful to get an estimate of the overturning rate of the lower cell, does not capture the spatial changes in the diapycnal velocities.

In this chapter, we have also investigated the contribution of different processes to the mixing-driven rate of overturning circulation of the lower MOC cell. Here we took into account the contribution of the near-field mixing induced by internal tides, lee waves and geothermal heat flux, but we have ignored several other processes that can contribute to mixing in the deep ocean, such as the far-field internal tides or near inertial waves. The overturning rate found here (8-13 Sv) is comparable to other studies that used a similar approach, i.e. similar estimates of internal waves, and similar parameterisations of the flux coefficient (Ferrari *et al.*, 2016; Mashayek *et al.*, 2017*c*). However, it is not surprising that such rate is small compared to the 20-30 Sv of overturning rate inferred from inverse models or ocean-state estimates (Lumpkin & Speer, 2007; Talley, 2003; Cessi, 2019), which inherently account for the contribution of several other processes. For example, we showed that near-inertial waves could potentially contribute significantly to the overturning of the lower cell, depending on how fast they decay in the ocean interior, a topic that requires more research.

The results presented here are naturally dependent on the estimates of internal waves and q_t used and on the details of the parameterisation of Γ, as well as on our knowledge of the stratification in the deep ocean. The estimate of internal tides and lee waves used here compare well with other estimates available in literature, for example Nikurashin & Ferrari (2013) and Scott *et al.* (2011), and some analysis with the estimate of energy conversion into internal tide from Nikurashin & Ferrari (2013) have returned almost identical results (not shown). As for the local breaking efficiency, $q_t(x, y)$ depends on the cutoff mode number used to partition the near-field to the far-field energy available to mixing, as discussed in the Supplementary Note 4 in Vic *et al.* (2019). In particular, they show that $q_t(x, y)$ is poorly sensitive to values of the critical mode number in [3, 4, 5], due to the very strong conversion occurring in high modes (modes > 10). Therefore, we do not expect changes in

$q_t(x, y)$ to significantly affect the results presented here.

The choice of the parameters used in defining $\Gamma(Re_b)$ is expected to affect the net water mass transformation, but it is less likely to affect the spatial patterns of diapycnal upwelling and downwelling. Here, we chose values of Re_b^* and Γ^* that fall in between the bounds reported in Mashayek *et al.* (2017*c*). Mashayek *et al.* (2017*c*) analysed the sensitivity of the net water mass transformation to the choice of such parameters, suggesting that the peak water mass transformation found here (8-13 Sv at the neutral density surface $\gamma^n = 28.1$) could vary of approximately ±4 Sv. Changes in the patterns of diapycnal upwelling/downwelling depend on the value of Re_b^*, but $Re_b^* = 100$ (used here) seems so far the best fit to the available observational, experimental and numerical data as summarised in Mashayek *et al.* (2017*c*) and Monismith *et al.* (2018) and we do not expect it to vary significantly. Finally, the uncertainty in our knowledge of the deep ocean stratification, mainly due to the irregularity in the sampling of the data, can also affect the results presented here.

The uncertainties discussed above imply that our results may change as we improve our estimates of internal wave-driven turbulence and our parameterisations of the flux coefficient. Both the details of the spatial patterns of the diapycnal velocities and the net mixing-driven overturning rate (being the residual of large diapycnal upwelling and downwelling) are likely somewhat affected by the uncertainties mentioned above. However, while the details of the results presented here cannot be accurate, we believe this work contributes to a better understanding of the role of different process in generating the diapycnal mixing that regulates the lower MOC cell. This works also emphasises the importance of co-varying the different parameters we use in out representation of mixing, given that the inter-dependent variations of such parameters has a significant impact on the patterns of diapycnal upwelling and downwelling. It is crucial to get a correct representation of the spatial distribution of diapycnal mixing to represent the exchange of water masses and tracers accurately across the density surfaces of the deep overturning circulation, and so correctly quantify the role of diapycnal mixing in the closure of the deep circulation and

in the global redistribution of tracers. The work presented in this chapter suggests that it is now timely to implement spatially variable local breaking efficiency and flux coefficient parameterisations to move towards a more accurate representation of the patterns of diapycnal upwelling and downwelling in ocean and climate models.

Chapter 4

Observation-based estimates of mixing in the Atlantic Ocean

The research presented in this chapter is close to submission under the following title: *"Significant cross-density mixing within the Atlantic Overturning Circulation", L. Cimoli, A. Mashayek, H.L. Johnson, D.P. Marshall, A.C. Naveira-Garabato, J. McKinnon, M.H. Alford, L.D. Talley, and C.B. Whalen*.

This chapter and the following one focus on the role of diapycnal mixing in the Atlantic Ocean, investigating both its contribution to the closure of the upper cell of the MOC (i.e. in bringing dense waters back to the surface) and, maybe even more importantly for our climate, in affecting the distribution of tracers carried by the southward flowing waters of the upper MOC.

As described in chapter 1, the Atlantic Ocean is the only basin in which dense waters form and sink at high latitudes in the northern hemisphere, generating the upper cell of the MOC (see figures 1.1 and 1.2). The stratification in the Atlantic Ocean (from WOCE climatology) is presented in figure 4.1, which shows neutral density surfaces (γ^n) at values

characteristic of the upper cell: density surfaces outcrop in the North Atlantic, where surface buoyancy fluxes form dense waters, and in the Southern Ocean, where the westerly winds draw dense waters up to the surface, and are almost flat throughout much of the Atlantic Ocean basin, between 48°N and 32°S.

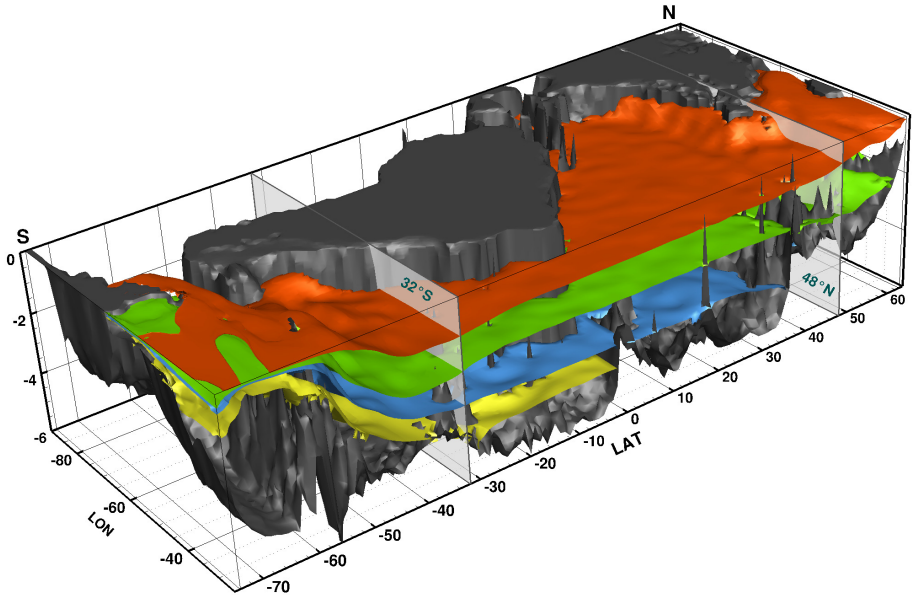


Figure 4.1: *Neutral density surfaces γ^n = 27.6 (orange), 28 (green), 28.1 (blue) and 28.2 (yellow) in the Atlantic basin. γ^n = 27.6 sits approximately at the maximum of the zonally integrated transport of the upper cell of the MOC, shown in figure 1.2; thus, it separates the waters flowing southward towards the Southern Ocean from the shallower waters flowing northward. γ^n = 28.2 coincides approximately with the boundary between the northward and southward flowing waters of the lower cell of the MOC.*

The upper cell of the MOC is the primary contributor to the redistribution of heat in the Atlantic Ocean (Johns *et al.*, 2011) and is especially important for the sequestration and transport of tracers that are taken up in the process of dense water formation. As an example, figures 4.2a and 4.2b respectively show the zonally-averaged concentration of oxygen in the Atlantic Ocean and the global concentration of oxygen at 2000 m from WOCE climatology. The deep Atlantic Ocean is greatly enriched in oxygen compared to the other major basins (figure 4.2b). This signal is associated with the oxygen-rich, southward-flowing waters formed in the North Atlantic (figure 4.2a), which contrast with shallower, northward-flowing waters that flow into the Atlantic from other basins and are

depleted in oxygen as a result of biological consumption. This pattern exemplifies the central role of the upper cell of the MOC in setting the global distribution and residence time of tracers in the ocean interior.

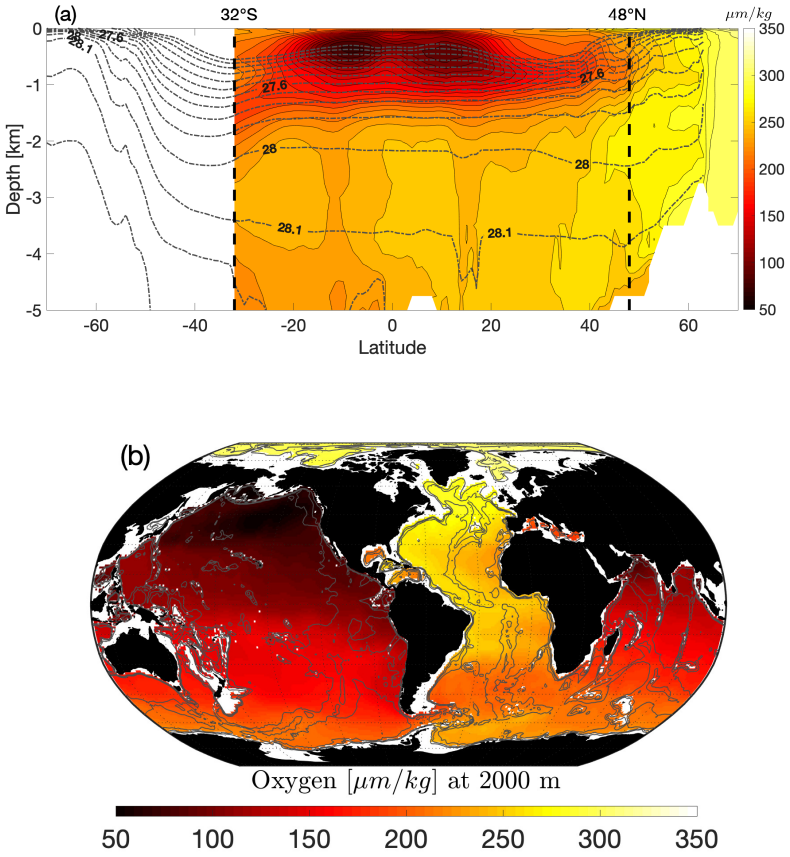


Figure 4.2: *(a) Zonally averaged concentration of oxygen in the Atlantic Ocean from WOCE data. The black dashed lines show the zonally averaged neutral density surfaces. (b) Concentration of oxygen at 2000 m from WOCE data.*

In between the outcropping regions in the North Atlantic and the Southern Ocean, the MOC's upper cell is often assumed to be mostly adiabatic, i.e. to flow along isopycnals (Toggweiler & Samuels, 1998; Gnanadesikan, 1999; Wolfe & Cessi, 2011; Marshall & Speer, 2012). The southward flowing waters of the upper MOC are mainly fed from the surface, by buoyancy loss induced sinking of dense water in the high-latitude North Atlantic, with only a minor contribution from below, by diapycnal mixing with the lower cell of the MOC (Marshall & Speer, 2012). These waters find their way back to the surface mainly through the pivotal role of the westerly winds in the Southern Ocean, with di-

apycnal mixing playing a minor role (Toggweiler & Samuels, 1998; Gnanadesikan, 1999; Marshall & Speer, 2012). This description of the upper cell of the MOC as an adiabatic flow has hindered the discussion of the role that diapycnal mixing can play in regulating the distribution of tracers across different water masses. To illustrate how diapycnal mixing may influence the pathways of tracers within the upper MOC cell, and in the global ocean circulation, consider the contrasting fates of two water masses that originate in the North Atlantic and flow southward towards the Southern Ocean. Water masses that when they reach the Southern Ocean are known as the Upper Circumpolar Deep Waters (UCDW, γ^n = 27.4 - 28) mainly upwell in a region of positive buoyancy flux, transform into lighter waters in the Southern Ocean and return to the North Atlantic on centennial time scales. In contrast, water masses that in the Southern Ocean are known as the Lower Circumpolar Deep Waters (LCDW, γ^n = 28 - 28.2) mainly upwell in a region of negative buoyancy flux, transform into denser abyssal waters near Antarctica and only re-emerge on millennial time scales (Sloyan & Rintoul, 2001; Santoso *et al.*, 2006; Talley, 2013; Naveira-Garabato *et al.*, 2014). Thus, any exchange of tracers induced by diapycnal mixing between the UCDW and LCDW prior to their entry into the Southern Ocean may lead to drastically different tracer pathways and significantly different global redistribution and ventilation timescales.

Here, the rate of diapycnal mixing within the density classes of the upper overturning cell is quantified from a set of state-of-the-art observational and theoretical mixing estimates in order to assess: (i) the contribution of diapycnal mixing to sustaining the upper cell by bringing dense waters back to the surface, and (ii) the extent to which diapycnal mixing may affect the pathways of tracers within the upper cell. Section 4.1 presents different estimates of either dissipation of turbulent kinetic energy or diapycnal diffusivity used here to infer diapycnal mixing. The role of diapycnal mixing in the closure of the upper overturning cell is discussed in section 4.2, while its role in the distribution of tracers is discussed is section 4.3. A brief concluding discussion of the results presented in this chapter is given in section 4.4.

4.1 Mixing estimates

A range of data sets from major international global ocean surveys is used here to provide a first estimate of basin-wide mixing in the Atlantic Ocean and its implications for the tracer transport by the upper cell. Global observational estimates of diapycnal mixing rates have become available only in recent decades through WOCE, the Global Ocean Ship-based Hydrographic Investigation Program (GOSHIP) (Hood *et al.*, 2010; Lumpkin & Speer, 2007; Naveira-Garabato *et al.*, 2014; Kunze, 2017*b*), the Argo float program (Whalen *et al.*, 2012) and implicitly through satellite altimetry observations, which has allowed for a quantification of tidal mixing (Garrett & Kunze, 2007).

These different types of estimates are here put together to provide a comprehensive description of diapycnal mixing in the Atlantic Ocean. We use (i) estimates of dissipation rate in the top 2000 m based on data from the global array of Argo floats (Whalen *et al.*, 2012); (ii) estimates of dissipation rate in the deep ocean, including the contribution of internal tides and lee waves (as presented in chapter 3) (Nikurashin & Ferrari, 2013; Ferrari *et al.*, 2016; Mashayek *et al.*, 2017*c*); (iii) estimates of dissipation rate based on a collection of hydrographic sections (Kunze, 2017*b*) and micro-structure profiles (Waterhouse *et al.*, 2014); and (iv) a bulk estimate of diapycnal diffusivity from an inverse model (Lumpkin & Speer, 2007). Note that (i) - (iii) are in the form of the dissipation rate of turbulent kinetic energy (ϵ), while the bulk estimate from Lumpkin & Speer (2007) returns information in the form of a diapycnal diffusivity (κ). Therefore, estimates of diapycnal mixing are calculated as $\mathcal{M} \approx \Gamma\epsilon \approx \kappa N^2$ depending on what product is used (see equations 2.24-2.25). A comparison between the localised estimates (i) - (iii) and the bulk estimate (iv) provides a measure of how much localised measurements of turbulent variables can be used to resolve the basin-scale diapycnal mixing (whose order of magnitude is given by the bulk estimate), and may help us identifying the areas in which data is lacking.

The estimates (i)-(iv) used here are either publicly available (iii) or have been kindly

shared by the authors of the papers cited above (i, ii and iv). These estimates have significant uncertainties, some intrinsic to the parameterisations used to infer mixing rate (Polzin *et al.*, 2014; Whalen *et al.*, 2015; Mashayek *et al.*, 2017*c*), and others due to sampling limitations. Despite these uncertainties, they have allowed us to gain knowledge in the quantification and spatial distribution of diapycnal mixing. Here, we contribute to the understanding of the significance of diapycnal mixing in the Atlantic Ocean by putting together these different estimates in the same currency. This work presents a first comparisons of these multiple approaches and aims to gain a first comprehensive look at the patterns of diapycnal mixing and its implications for the ocean circulation and tracer distributions.

Each estimate, briefly described in the following sections, is here used to calculate the contribution of diapycnal mixing to the density transformation of water masses in the Atlantic Ocean interior, and to the redistribution of tracers across different waters of the upper MOC cell, i.e. investigating how diapycnal mixing can affect the location at which tracers will upwell in the Southern Ocean, with implications for their redistribution across the different corridors of the global ocean circulation.

4.1.1 Estimates of diapycnal mixing based on Argo

Argo is an array of free-drifting floats that measure temperature, salinity and velocity over the upper 2000 m of the global ocean (http://argo.ucsd.edu/). Given that diapycnal mixing is highly variable in space and time, and so not sufficiently sampled by coarse-resolution ship-based observations, shear- and strain-based parameterisations (Kunze *et al.*, 2006; Polzin *et al.*, 2014) have been used to infer the rate of diapycnal mixing from Argo observations (Whalen *et al.*, 2012), which sustain measurements at a much higher spatial and temporal resolution than available from ships. The finescale parameterisation is based on internal wave-wave theory (McComas & Müller, 1981; Henyey *et al.*, 1986; Henyey, 1991): away from direct forcing by wind and currents at the boundary, the production of turbulence is controlled by the rate at which the internal wave energy cascades from large

to small vertical scales (Kunze *et al.*, 2006; Polzin *et al.*, 2014; Kunze, 2017*b*). The shear- and strain-based parameterisations provide a way to infer turbulence production from the internal wave shear and/or strain. Comparison with direct micro-structure measurements have shown that the strain parameterisations agree within a factor of 2-3 (Polzin *et al.*, 1995, 2014; Whalen *et al.*, 2015).

Here we employ estimates of the turbulent kinetic energy dissipation rate based on Argo from an update of the dataset in Whalen *et al.* (2012, 2015) (the updated data has a higher spatial and temporal resolution). The rate of turbulent dissipation by breaking internal waves is computed by applying a finescale parameterisation to estimates of vertical strain variance calculated over 200 m long segments of the Argo density profiles. To ensure that the observed strain is associated with internal waves, data within the upper-ocean mixed layer and in mode waters are removed from the profiles, segments that have large variability in stratification are omitted, and low-stratification segments are removed because there the calculated strain is dominated by noise. The finescale parameterisation used to build the estimates here, and its underlying assumptions, are comprehensively described by Whalen *et al.* (2012).

Figures 4.3a,b show the localised estimates of dissipation rate from the Argo-based parameterisation on two different density surfaces, interpolated to fill the gaps where Argo data are missing. These estimates reveal marked spatial variability, with intense dissipation in regions of rough topography, elevated tidal and wind energy or high eddy kinetic energy (Whalen *et al.*, 2012). The estimates are in good agreement with microstructure profiler observations: when at least 10 estimates are averaged together, 81% of the dissipation rate comparisons agree within a factor of 2, and 96% agree within a factor of 3 (Whalen *et al.*, 2015). An accurate estimate of the basin-mean dissipation rate is contingent on averaging over a large enough number of point estimates. In the analyses that follow, the Argo-based estimates are averaged on different density surfaces across the entire Atlantic Ocean interior (48°N - 32°S), so the uncertainty is expected to be within the factor of 2-3 found in Whalen

et al. (2015).

4.1.2 Estimates of bottom-generated diapycnal mixing

In the deep ocean, below the depth range covered by Argo floats, estimates of diapycnal mixing are inferred from the rate of energy conversion into internal waves from tidal and geostrophic currents as they impinge upon rough topography. The estimates of internal tide and lee wave energy conversion used here are based on the earlier studies of Nikurashin & Ferrari (2013), Ferrari *et al.* (2016) and Mashayek *et al.* (2017*a*). In Chapter 3 we used the same estimate of lee wave energy conversion, but a different estimate of internal tide energy conversion (from Vic *et al.* (2019)); the different estimates of internal tide energy conversion used in this thesis largely agree (not shown). It is here assumed that the rate of wave breaking is constant and equal to $q = 0.3$, and that the energy decays upward with a decay scale of 500 m. Out of the locally expended energy, it is here assumed that a constant fraction $\Gamma = 0.2$ goes to mixing while the rest is lost in viscous dissipation (St Laurent *et al.*, 2002; Mashayek *et al.*, 2017*a*). The results with a variable q and Γ (not shown here) return very similar water mass transformation (later discussed in figure 4.5) to the case with constant parameters. Figures 4.3c,d show the localised estimates of dissipation rate from bottom-generated mixing on two different density surfaces. The turbulence generated by internal tides and lee waves in the deep ocean is enhanced in the proximity of rough bottom topography (such as around the Mid-Atlantic Ridge) and rapidly decays away from the bottom given the sharp decay scale of 500 m, hence explaining the much weaker values in the ocean interior on lighter density surfaces (figure 4.3c).

In the calculation of diapycnal mixing generated at the ocean bottom, the contribution of geothermal heat flux (from the estimate of Davies & Davies (2010)) is also taken into account.

4.1.3 Estimates of diapycnal mixing based on CTD data

One of the major limitations of the estimates presented above (sections 4.1.1 and 4.1.2) is that they are each limited to only a portion of the water column, the top 2000 m of the ocean for the Argo-based estimates, and the bottom of the ocean, given the sharp decay scale used for the estimates of bottom-generated mixing. To overcome this limitation, we consider a third dataset which combines dissipation rate estimates from hydrographic casts, from Kunze (2017*b*) (Conductivity, Temperature and Depth - CTD - profiles, which return a localised vertical profile of temperature and salinity), with estimates of the dissipation rate from microstructure profiles, from Waterhouse *et al.* (2014). Kunze (2017*b*) inferred internal wave-driven turbulent dissipation rates (ϵ) and diapycnal diffusivities (κ) by applying a finescale parameterisation to $\sim 30,000$ CTD profiles (see section 4.1.1 for a brief description of the parameterisation used by Kunze (2017*b*)). Direct measurements of the dissipation rate of turbulent kinetic energy from $\sim$ 800 microstructure profiles (Waterhouse *et al.*, 2014) have been added, which mainly improve the quality of the estimates below 2000 m in areas of strong internal tides. Figures 4.3e-g show the dissipation rate estimate from CTD data and microstructure profiles on different density surfaces. These estimates agree with the picture shown by the Argo-based estimates (figures 4.3a,b), both qualitatively, identifying the regions on enhanced turbulence (e.g. in the northwest Atlantic Ocean, a region of enhanced eddy activity and where the Mid-Atlantic Ridge reaches shallower depths) and weak turbulence (e.g. in the Angola basin), and quantitatively, returning the same magnitude of ϵ (with a few exception in the mid Atlantic). The use of hydrographic and microstructure data has the advantage of providing a continuous estimate from the surface to the bottom based on observations, but has a coarser horizontal resolution (figures 4.3e-g show the results from Kunze (2017*b*) gridded on a 1°grid), and lacks information close to topographic boundaries. Moreover, this dataset is well suited for the study of quasi-steady turbulence sources, such as internal waves in the ocean interior, but

given its limited temporal resolution is less suitable for studying wind-driven turbulence, for which Argo floats are more appropriate (Kunze, 2017*b*).

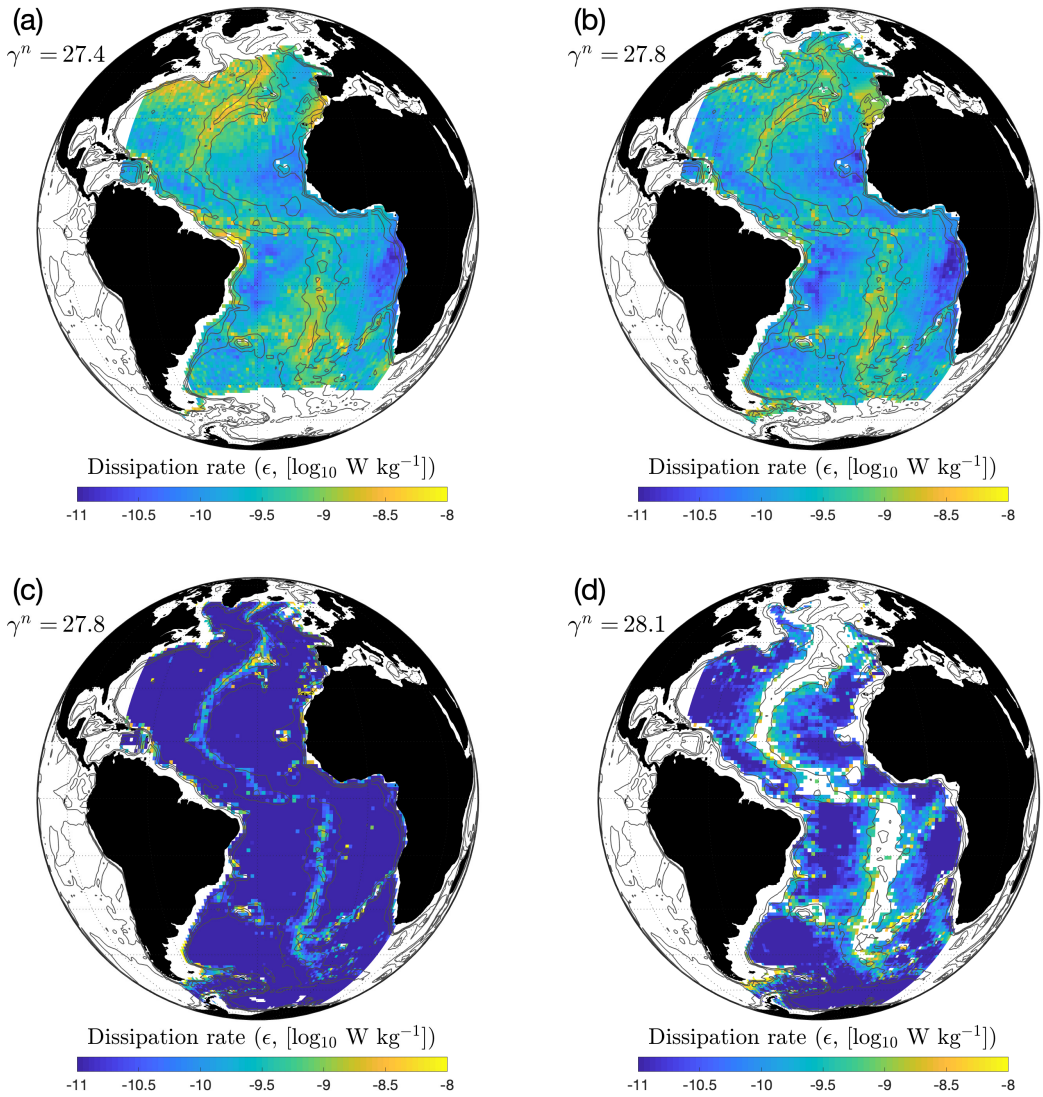


Figure 4.3: *Dissipation rate of turbulent kinetic energy from: (a)-(b) Argo-based estimates on the density surfaces (a) γ^n = 27.4 and (b) γ^n = 27.8; (c)-(d) estimates of internal waves (internal tides and lee waves) breaking in the deep ocean on the density surfaces (c) γ^n = 27.8 and (d) γ^n = 28.1; (e)-(g) estimates from CTD data and microstructure profiles on the density surfaces (e) γ^n = 27.4, (f) γ^n = 27.8 and (g) γ^n = 28.1.*

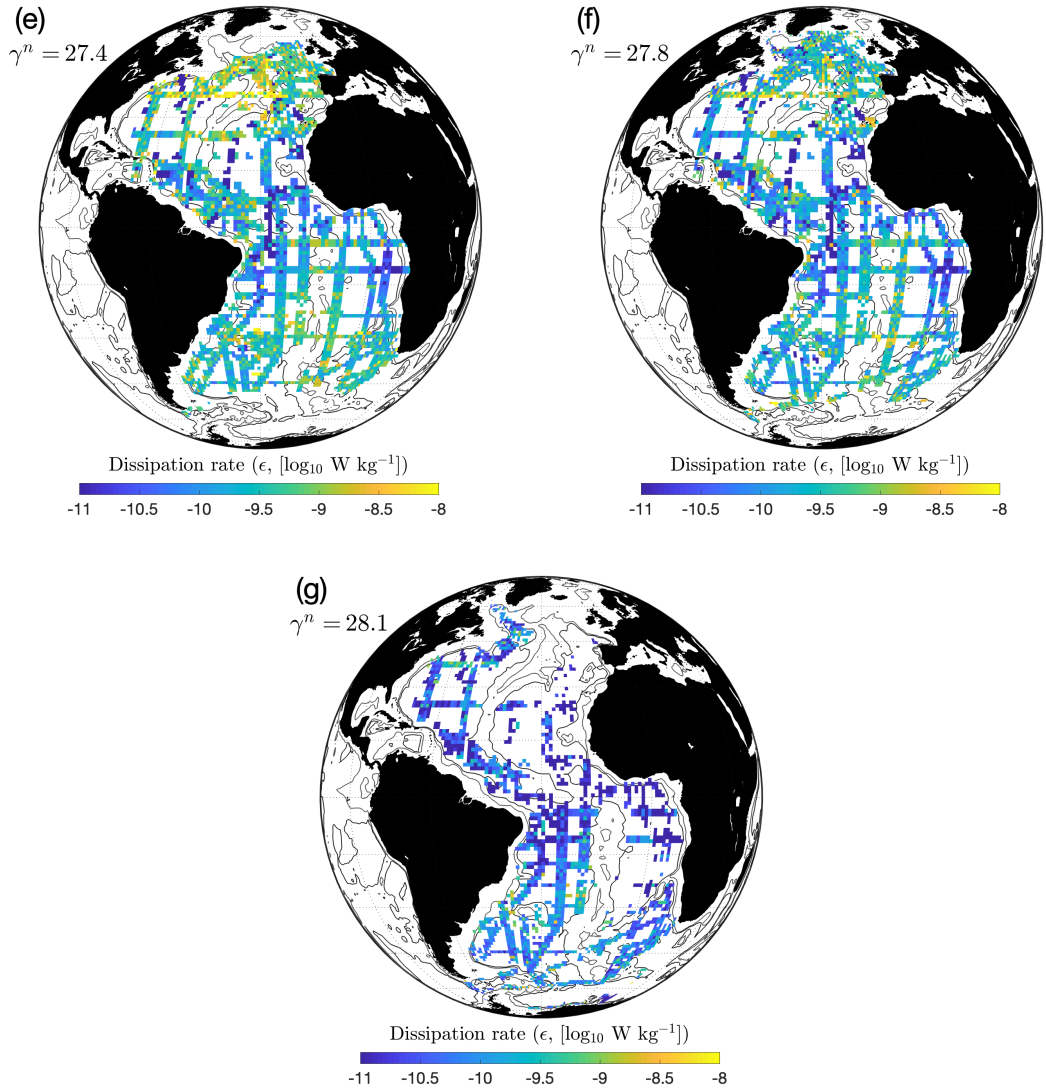


Figure 4.3 continued

4.1.4 Bulk estimates of basin-scale diapycnal mixing

The localised estimates of turbulence outlined above suffer from two substantial limitations: they lack full spatial coverage (across the globe, in depth and especially close to boundaries), and entail a range of underlying assumptions. As such, it is important to assess inferences from these estimates against bulk diagnostics of basin-scale diapycnal mixing. Bulk estimates are obtained from inverse models, which reconstruct the ocean circulation by constraining it with data from hydrographic sections, floats, current measurements, and

satellite altimetry, amongst other sources (Ganachaud & Wunsch, 2000; Ganachaud, 2003; Talley *et al.*, 2003; Lumpkin & Speer, 2007; Naveira-Garabato *et al.*, 2014). Such inverse estimates typically dissect the ocean into various large regions and use the observational data to close the density budget of each region, tuning diapycnal mixing to achieve closure.

In this thesis, the inverse estimate of Lumpkin & Speer (2007), which used WOCE hydrographic sections and observational data sets of air-sea exchanges of heat and freshwater to quantify the global MOC, is employed. Hydrographic sections are used to divide the ocean into different boxes, in which diapycnal mixing is estimated as a bulk averaged rate across each density surface. In particular, Lumpkin & Speer (2007) evaluated diapycnal mixing in the Atlantic Ocean between 48°N and 32°S, which overlaps optimally with the region of interest of this work. This bulk estimate does not provide any information on the spatial pattern of mixing within this large region, nor on the processes that underpin it. However, it gives information on the order-of-magnitude of mixing required to sustain the inferred MOC. Processes that are not measurable, and may thus be missing from the local measurements, are implicitly included in the bulk estimate.

4.2 Diapycnal water mass transformation in the Atlantic Ocean

This section describes the contribution of turbulent mixing to the diapycnal transformation rate of water masses within the upper MOC waters in the Atlantic Ocean interior. The analyses span density classes corresponding to the northward and southward branches of the upper cell of the MOC. Note that the density which separates southward and northward flowing waters of the upper MOC changes with latitude, but falls in the range of density values, $\gamma^n \approx 27.4 - 27.7$ (see figure 3 in Lumpkin & Speer (2007)). The maximum of the overturning streamfunction is characterised by denser waters ($\gamma^n \approx 27.7$) in the North Atlantic, and gets lighter while moving southward ($\gamma^n \approx 27.4$ at 32°S), indicating that wa-

ters are mixed along the way (see inverse estimates from Talley *et al.* (2003) and Lumpkin & Speer (2007)). Note also that the southward flowing waters can also be separated into waters that will contribute to UCDW, which will then be transformed mainly into lighter waters in the Southern Ocean, and waters that will contribute to LCDW, which will be transformed into denser waters in the Southern Ocean. Various studies, such as Sloyan & Rintoul (2001), Santoso *et al.* (2006) and Naveira-Garabato *et al.* (2014), set the boundary between UCDW and LCDW at $\gamma^n \approx 28$.

The water mass transformation rate is the rate at which water is transformed to a different density via diapycnal mixing. As described in section 3.3, in the presence of a vertical divergence of the buoyancy flux, water masses move across density surfaces with the diapycnal velocity $\tilde{\mathbf{e}} \approx (1/\partial_z \rho)(\partial \mathcal{M}/\partial z)\,\mathbf{z}$. The diapycnal velocity is positive (implying upwelling) when mixing decreases with depth, such as in the case of surface-intensified mixing and close to ocean boundaries, as demanded by the no-flux boundary condition through the ocean bottom (Ferrari *et al.*, 2016). On the contrary, the diapycnal velocity is negative (implying downwelling) when mixing increases with depth, such as in the interior of the deep ocean, where mixing is bottom enhanced. The diapycnal velocity for the estimate of bottom-generated diapycnal mixing on the density surface $\gamma^n = 28.1$ is shown in figure 4.4a: diapycnal upwelling (red) is happening in the vicinity of rough topography, for example along the Mid-Atlantic Ridge and along the western boundary around the equator and in the South Atlantic; diapycnal downwelling (blue) takes place in the ocean interior (St Laurent *et al.*, 2001; De Lavergne *et al.*, 2016; Ferrari *et al.*, 2016).

For a neutral density surface γ^n, the transformation rate across it in the ocean interior is given by the integral of the diapycnal velocities over that density surface (equation 3.7). The net transformation rate is therefore given by the residual of two contributions: the water mass transformation along the boundaries, which generates an along-isopycnal upwelling, and the water mass transformation in the ocean interior, which generates diapycnal upwelling/downwelling depending on the sign of $\partial \mathcal{M}/\partial z$. For the estimates of diapycnal

mixing used here, the role of the above two contributions can be investigated only with the estimate of bottom-generated mixing; neither the Argo-based nor the hydrographic-based estimates have enough resolution to resolve the water mass transformation along the boundaries, and the bulk estimate does not carry any information about the spatial variation of mixing.

Figure 4.4b shows the water mass transformation rate $\mathcal{D}(\gamma^n)$ for the diapycnal velocities shown in figure 4.4a, as well as for other density surfaces in the deep ocean (here only the density range γ^n = 27.9 - 28.3 is shown, since the water mass transformation rate at lighter density surfaces is negligible when considering just the bottom-generated mixing, which decays sharply away from the bottom). The contributions of along-boundary upwelling and interior downwelling are represented by the empty red and blue bars, respectively, while the residual water mass transformation rate integrated over the entire isopycnal between 48°N and 32°S is shown by the filled black bars. The residual water mass transformation is positive for most of the density surfaces analysed, indicating a net lightening of these water masses. This result is consistent with Ferrari *et al.* (2016) and agrees with the theory that diapycnal mixing in the deep ocean acts to raise dense waters back to shallower depths, contributing to the closure of the overturning cells of the MOC.

The results show that the maximum net water mass transformation is less than 2 Sv, but the red and blue bars indicate more than 6 Sv and -4 Sv of diapycnal upwelling and downwelling, respectively. Thus, the net water mass transformation of $\sim$ 2 Sv is the residual of two much larger contributions. This result is naturally dependent on the estimates of internal tides and lee waves used and on the values of q and Γ chosen. However, the qualitative picture shown here is robust to changes in these parameters (not shown). This point has significant implications for the distribution of tracers: while the residual seems to suggest little exchange across these density surfaces, the two separated contributions suggest that tracers can experience significant upwelling/ downwelling depending on their location and distribution. Therefore, when investigating the exchange of tracers between different water

masses, it is important to take into account where the tracers are located together with the spatial distribution of diapycnal upwelling and downwelling.

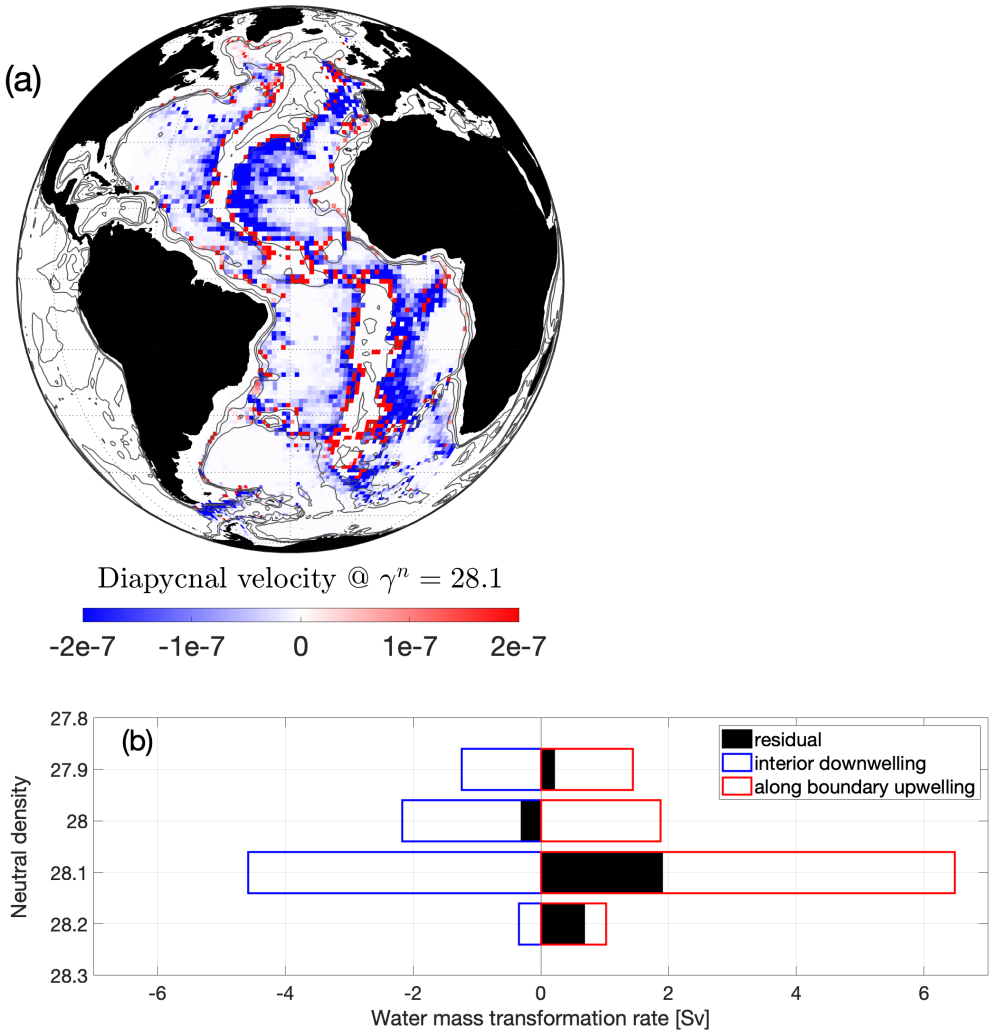


Figure 4.4: *(a) Diapycnal velocity, calculated as per equation 3.6, for the bottom-generated mixing on the density surface γ^n = 28.1. Positive values (red) indicate diapycnal upwelling, while negative values (blue) indicate diapycnal downwelling. (b) Water mass transformation rate, calculated as per equation 3.7, for the bottom-generated mixing estimate. The contributions of along-boundary upwelling and interior downwelling are shown by the empty red and blue bars, respectively, while their residual is shown by the filled black bar.*

The Atlantic-integrated residual water mass transformation rate, based on the different estimates of diapycnal mixing discussed in section 4.1 is shown in figure 4.5a. The basin-integrated transformation rates shown in figure 4.5a have been calculated in the Atlantic Ocean between 48°N and 32°S. The density range identified by the pink band (γ^n = 27.4-

27.7) indicates the boundary between the southward and northward flows of the upper cell of the MOC, while the green band around $\gamma^n = 28$ indicates the boundary between waters that will contribute to the formation of UCDW (waters lighter than $\gamma^n = 28$), and LCDW (waters denser than $\gamma^n = 28$). The boundary between upper and lower cells of the MOC is $\gamma^n = 28.2$ (Sloyan & Rintoul, 2001; Naveira-Garabato *et al.*, 2014).

The net transformation rate is positive for most density levels in figure 4.5a, indicating a net diapycnal upwelling or, in other words, a lightening of the deep and abyssal waters. The different estimates return a consistent pattern: the transformation rate is larger within the southward branch of the upper MOC, and especially in the UCDW density range (between $\gamma^n = 27.7$ - 28), and weakens both for lighter and denser density classes - but increases slightly again while getting closer to the surface ($\gamma^n = 27.2 - 27.3$). The fact that different estimates, based on data collected with different methods and using different parameterisations or assumptions, return a similar pattern is promising and gives confidence that we can use such estimates to try to draw a basin-wide picture of diapycnal mixing. The Argo-based estimate (red) is available only down to $\gamma^n = 27.9$, since denser waters lie below 2000 m (hence out of reach of the Argo floats). Argo floats return the smallest of the estimates of water mass transformation rate, with values up to $\sim$ 1 Sv at $\gamma^n = 27.8$-27.9 and on the lighter surface $\gamma^n = 27.3$, and weaker values on the other density surfaces. Bottom-generated mixing (green) returns a water mass transformation maximum of $\sim$ 2 Sv at $\gamma^n = 28.1$; values for lighter density classes are negligible, as expected, given the sharp decay scale and are thus not shown for clarity of the plot. The estimate based on CTD data and microstructure profiles (yellow) returns transformation rates up to $\sim 2 - 2.5$ Sv within the southward flowing waters of the upper MOC cell, and smaller values for both lighter and denser isopycnals. As reported in Kunze (2017*b*), this estimate has limited temporal resolution and does not well capture the wind-driven turbulence in the upper ocean, for which the Argo-based estimate is better suited; this may perhaps explain the negative values for light density surfaces, $\gamma^n = 27.3$-27.4. The bulk estimate from Lumpkin & Speer (2007)

(blue) returns the largest values, up to ~ 4 Sv at γ^n = 27.8-27.9, i.e. in the UCDW density range.

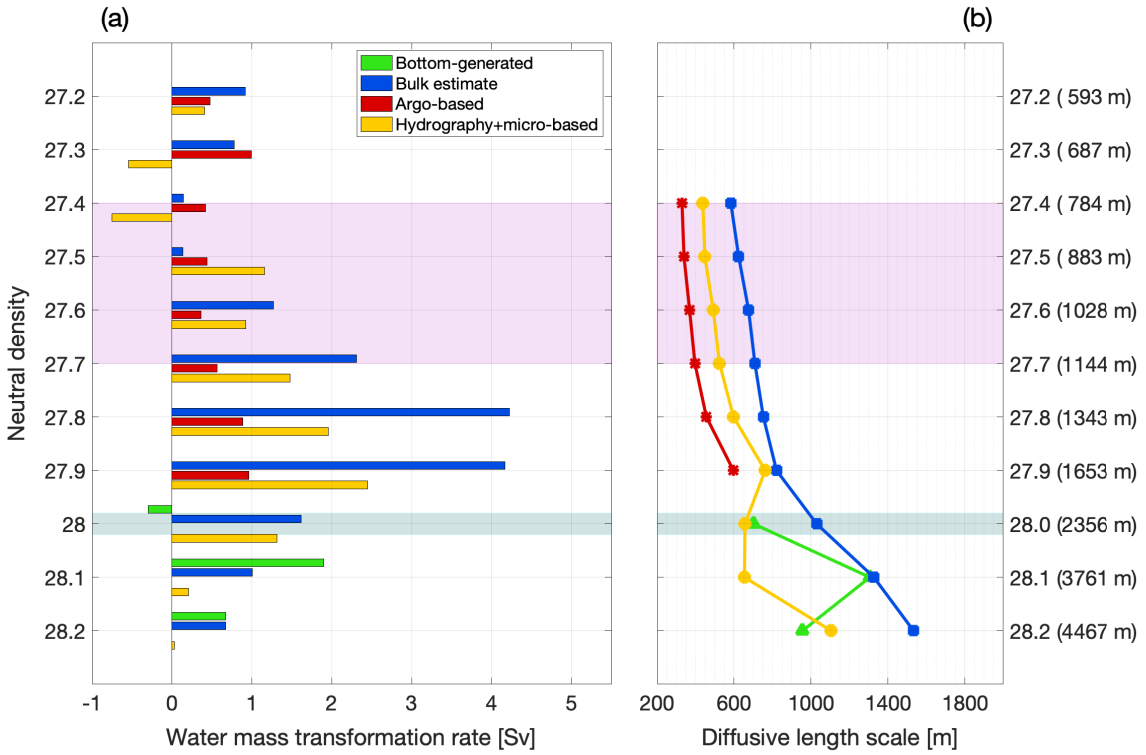


Figure 4.5: *(a) Water mass transformation rate and (b) diffusive length scale from the Argo-based estimate of diapycnal mixing (red), estimate of bottom-generated diapycnal mixing (green), CTD data+microstructure profile-based estimate (yellow) and the bulk estimate of diapycnal mixing from Lumpkin & Speer (2007) (blue). The y-axis in panel (b) reports the mean depth of each density surface in the Atlantic Ocean between 48°N and 32°S. The pink shading indicates the density range separating the southward and northward flow of the upper cell. The green shading indicates the density range separating UCDW and LCDW.*

4.3 Diffusive tracer transport in the Atlantic Ocean

Given the significant amount of mixing within the southward flowing waters (figure 4.5a), it is not unreasonable to expect that tracers carried southward by the upper cell of the MOC can diffuse across density surfaces. To crudely quantify the tracer diapycnal diffusion, it is possible to calculate a diffusive length scale, which represents the extent to which diapycnal mixing can potentially move a tracer in the vertical as it is transported by the

southward branch of the upper MOC cell from the North Atlantic (48°N) to the Southern Ocean (32°S). Diffusion of tracers across density surfaces depends on the ambient effective turbulent buoyancy flux ($\mathcal{M}$), density stratification (N^2) and transit time (Δt). The latter is an estimate of the time it takes for a tracer to be carried by the upper cell of the MOC from 48°N to 32°S.

Following Fick's law of diffusion, the diffusive length scale is calculated as

$$\mathcal{L} = 2\sqrt{\frac{\langle \mathcal{M} \rangle}{N^2}\Delta t} \;=\; 2\sqrt{\kappa \Delta t}, \tag{4.1}$$

where $\langle \mathcal{M} \rangle$ is the buoyancy flux averaged over each density surface and is inferred from the different estimates described in section 4.1, and the average N^2 is calculated from WOCE hydrographic climatology. Note that the calculation of $\mathcal{L}$ in equation (4.1) can also be written as a function of a diffusivity coefficient, κ, through the approximation $\mathcal{M} \approx \Gamma\, \epsilon \approx \kappa\, N^2$ (see chapter 1, equation 2.25). The transit time Δt is inferred from observations of the meridional transport in the North Atlantic at 26°N available from the RAPID array. A decadal average of the transport at 26°N (Smeed *et al.*, 2014) is used to calculate an average meridional velocity at different depths from the transport maximum at ~ 1100 m to ~ 4500 m, where the zonally integrated transport changes direction (i.e. below 4500 m the transport is northward). The average velocity is used to calculate a depth-dependent estimate of the transit time from 26°N to 32°S. The mean depth of the density surfaces (shown along the right-hand y-axis in figure 4.5b) is then used to estimate the mean transit time for waters at each density level. This transit time is ~ 100 years at $\gamma^n = 27.6$, whose average depth is close to the depth of the maximum southward transport (see Smeed *et al.* (2014)), and ~ 350 years at $\gamma^n = 28.2$. Note that the focus here is on the transit time of the southward flowing waters, and therefore the northward branch of the upper cell is not considered here. For this reason, the diffusive length scale is only calculated up to $\gamma^n = 27.4$, i.e. within the lightest southward flowing waters (recalling again that the boundary between southward

and northward waters changes with latitude).

Figure 4.5b shows the diffusive length scale corresponding to the different estimates presented in figure 4.5a. For the density classes associated with the southward flow of the upper MOC cell, $\mathcal{L}$ lies between 350 m and 1500 m approximately. If compared with the mean depth of the density surfaces reported in figure 4.5b, the diffusive length scale calculated here suggests that tracer can potentially experience enough mixing to diffusively move between different water masses. For example, a diffusive length scale of $\sim 800 - 1000$ m at $\gamma^n = 28$ or of ~ 1400 m at $\gamma^n = 28.1$ indicates that mixing could potentially move tracers from waters that will contribute to LCDW to waters that will convert into UCDW. Thus, mixing can potentially move tracers between water masses with very different pathways and lifecycles, leading to significantly different ventilation times. As a second example, a diffusive length scale of ~ 400 m at $\gamma^n = 27.6 - 27.7$ indicates that tracers could potentially move from the southward branch of the upper cell of the MOC to the overlying northward branch. Thereby, tracers could be carried back to the North Atlantic and into contact with the atmosphere over much shorter timescales.

It is important to note that calculation of the diffusive length scale relies on two important limiting assumptions: (i) the mean buoyancy flux is calculated from either the rate of dissipation of turbulent kinetic energy or from the diapycnal diffusivity, integrated over each density class, and is therefore meaningful only in a bulk sense; (ii) the heterogeneity of tracer concentration over isopycnals is not accounted for. This calculation is, therefore, only meaningful in an average sense and provides a first guess of how significant mixing is for tracer transport in the Atlantic Ocean. As noted above, the spatial patterns of both mixing and tracer concentration are key in determining how much diapycnal mixing, and hence upwelling/downwelling, a tracer will experience. When carried over weak mixing regions, a tracer experiences only a minor vertical displacement. But in regions of enhanced mixing, the mean vertical tracer displacement estimated here could be an under-estimate.

4.4 Summary and conclusions

In this chapter, it has been shown that there is significant diapycnal mixing within the southward flowing branch of the upper cell of the MOC, with important implications for the redistribution of tracers carried by it into the ocean interior. We used different available estimates of the dissipation rate of turbulent kinetic energy or diapycnal diffusivity to investigate the role of diapycnal mixing the closure of the upper MOC cell and in setting the distribution of tracers carried within these dense waters. These estimates, while previously available from past studies, have never been compared by putting them all in the same currency in terms of water mass transformation rate, as it has been done here. All the different estimates used here (both from localised sources and a bulk estimate) return a similar vertical profile of water mass transformation rate and show that diapycnal mixing transforms waters mostly in the southward flowing limb of the upper MOC cell, and especially in the UCDW ($27.4 < \gamma^n < 28$) density range. The water mass transformation found here suggests that diapycnal mixing can contribute between $\sim 1-2$ Sv to the closure of the upper cell of the MOC, therefore contributing only marginally to raising the dense waters formed in the North Atlantic back to the surface. This is a smaller contribution than that estimated from inverse models, which indicate a diapycnal component of the upper MOC cell of approximately 6 Sv (Talley *et al.*, 2003; Lumpkin & Speer, 2007). This result confirms that the upper cell is largely adiabatic, as already vastly discussed in literature. The novelty and additional value of this quantification is that it relies on direct or inferred estimates of diapycnal mixing, and not on theoretical contributions or idealised numerical simulations (e.g. Gnanadesikan (1999); Wolfe & Cessi (2011); Marshall & Speer (2012); Nikurashin & Vallis (2012); Johnson *et al.* (2019)).

The water mass transformation calculation also shows a discrepancy in the amount of diapycnal mixing estimated: while the localised estimates (based on Argo floats, CTD data and microstructure profiles, and theory of internal wave breaking in the deep ocean) return

a maximum of ~ 2 Sv transformation rate for the density classes investigated here, the bulk estimate from Lumpkin & Speer (2007) returns values up to ~ 4 Sv. The localised estimates all have uncertainties intrinsic to the parameterisations used to infer mixing (Polzin *et al.*, 2014; Whalen *et al.*, 2015; Mashayek *et al.*, 2017*c*). While these uncertainties can explain part of the discrepancy, they might not fully justify the difference between 2 Sv and more than 4 Sv. The source of the discrepancy between the different estimates could potentially reside in the lack of ability of the Argo floats and CTD data to capture turbulent processes in close vicinity to the ocean boundaries, and the lack of representation of such processes in the bottom-generated estimate employed here. Such processes, while not included independently in bulk inverse estimates, are implicitly accounted for therein as bulk inverse estimates try to close the budgets of basins constrained by observed hydrographic sections. This suggestion adds to evidence from recent studies in other regions of the ocean which have found a discrepancy between bulk estimates and those based on localised measurements of mixing (Huussen *et al.*, 2012; Voet *et al.*, 2015; Mashayek *et al.*, 2017*b*). Close to boundaries, such as continental shelves, mid-sea ridges, seamounts or canyons, non-propagating processes such as hydraulic jumps and trapped/evanescent waves can generate significant diapycnal mixing (Alford *et al.*, 2013; Voet *et al.*, 2015; Van Haren *et al.*, 2017; Van Haren, 2018). Evidence of enhanced mixing in the vicinity of western boundaries in the Atlantic Ocean has been previously reported (Stober *et al.*, 2008; Kohler *et al.*, 2014) but without direct connections to basin-wide diapycnal upwelling of water masses and tracers.

The water mass transformation rates calculated here are naturally affected by different sources on uncertainties, which are quantitatively challenging to quantify, but are qualitatively discussed here. The estimates of dissipation rate inferred from the observations of Argo floats or CTD casts depend on the choices made in applying the strain-based parameterisation, for example the length of the segments chosen for averaging, the number of observations used for averaging and the shear-to-strain ratio (Kunze *et al.*, 2006; Whalen

et al., 2012, 2015; Kunze, 2017*b*, *a*). While it is challenging to assess systematic biases, here we average the individual estimates over wide areas (e.g. over a density surface in the mid-Atlantic Ocean), which helps in reducing the uncertainties in individual estimates (Whalen *et al.*, 2015; Kunze, 2017*a*). Kunze (2017*b*) converts the estimates of dissipation rate from the strain-based parameterisation into estimates of diffusivity, which the author compares with the results from Lumpkin & Speer (2007). They show that the inferred diffusivity falls within the range estimated by the inverse model, except for density classes denser than $\gamma^n > 28$ (where the bulk diffusivity from Lumpkin & Speer (2007) is largely uncertain, given that their inverse model mainly relies on air-sea fluxes observations, and returns large uncertainties at depth). The uncertainty associated with the estimates of bottom-generate mixing have been extensively discussed in chapter 3, and are briefly summarised here. Different estimates of energy conversion into internal tides and lee waves return very similar results (not shown). The choice of parameters (such as q and Γ) used to inferring mixing does not significantly alter the picture of the water mass transformation rates shown here (not shown), as shown also in chapter 3. While these different sources of uncertainties should be taken into account and better quantified, the fact that the different estimates return a similar vertical profile of water mass transformation rate is promising and suggests that we are on the right track to build a more complete picture of diapycnal mixing in the Atlantic Ocean.

The significant amount of diapycnal mixing found within the southward flowing branch of the upper cell suggests that tracers can experience significant diapycnal upwelling/downwelling and so be exchanged between different water masses along their pathways from 48°N to 32°S. In particular, it has been shown that the net water mass transformation is the residual of two larger contributions, i.e. along-boundary upwelling and interior upwelling/-downwelling. Thus, insofar as tracer mixing is concerned, it is important to consider both contributions: while the residual seems to suggest little exchange across density surfaces, the two separated contributions suggest that tracers can experience significant upwelling/-

downwelling depending on their location and distribution.

To estimate the extent to which diapycnal mixing can move a tracer in the vertical as it is transported by the southward flowing branch of the upper cell, we calculated a diffusive length scale. The diffusive length scale calculated here is meaningful only in a bulk sense, since it uses the average buoyancy flux on density surfaces and does not take into account the heterogeneity of tracer concentration over isopycnals. However, it returns an estimate of how much mixing can potentially impact tracer distribution. It has been found that tracers can potentially experience enough mixing to diffusively move between different water masses prior to their entrance into the Southern Ocean in the Atlantic sector. As schematically shown in figure 4.6, different water masses can have very different fates once they upwell in the Southern Ocean: while the UCDW is mainly transformed into lighter water and much of it finds its way back to the Northern Hemisphere, the underlying LCDW is mainly transformed into denser abyssal waters and sinks into the abyss around Antarctica. Hence, if tracers mix between these water masses prior to their entrance into the Southern Ocean in the Atlantic sector, they will experience very different pathways with sequestration times that can vary from hundreds to thousands of years.

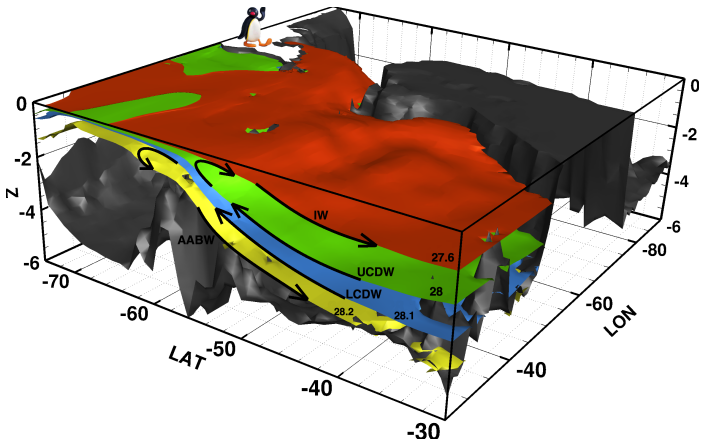


Figure 4.6: *Schematic of the circulation in the Atlantic sector of the Southern Ocean overlaid on outcropping density surfaces (shown in different colors and labelled in the figure). Black arrows show the pathways of the UCDW and LCDW, the former transformed into lighter waters and moving back northward and the latter transformed into denser waters and contributing to the formation of AABW.*

The results shown in this chapter indicate that, while it is reasonable to neglect the net contribution of diapycnal mixing in the closure of the upper cell (in agreement with previous literature), it is important to include its contribution in setting the distribution of tracers carried by these dense water masses. Indeed, describing the upper cell as an adiabatic flow can hinder the discussion of the role that diapycnal mixing can potentially play in changing the distribution of tracers within the Atlantic Ocean. The diffusive length scale suggests that more research should be dedicated to more accurately quantify the patterns of diapycnal mixing and their interaction with the tracer distributions. To start addressing some of these points, in the next chapter we analyse the diffusive spreading of a tracer in the Atlantic Ocean by using a set of quasi-realistic numerical simulations.

Chapter 5

A numerical study of tracer mixing in the Atlantic Ocean

The research presented in this chapter is being prepared for submission under the following title:
"Significance of diapycnal mixing for tracer pathways in the Atlantic Ocean", L. Cimoli, S. Downes, H.L. Johnson, D.P. Marshall, A. Mashayek, A.C. Naveira-Garabato, K. Snow.

In this chapter, we analyse how diapycnal mixing can impact the distribution of a tracer carried by the upper MOC cell in a sector model of the Atlantic Ocean. In particular, we analyse how a different model representation of mixing can affect the upwelling of the tracer in the Southern Ocean, with important implications for its global distribution.

The representation of diapycnal mixing in ocean and climate models has evolved in the last few decades, as summarised in the review papers Jayne (2009) and MacKinnon *et al.* (2017). Mixing was originally represented in models via a diffusivity coefficient constant in space and time, with the exception of the Bryan & Lewis (1979); Marotzke (1997); Scott & Marotzke (2002) profile, which is horizontally uniform but increasing with

depth, to represent the larger diffusivity observed in the deep ocean. In particular, it was shown that both the strength of the overturning circulation and the ocean heat transport are sensitive to the choice of diapycnal mixing used in the models (e.g. Bryan (1987)). Direct observations of enhanced bottom mixing (e.g. Polzin *et al.* (1997); Ledwell *et al.* (2000)) and a better knowledge of the dissipation rates and locations of barotropic tides (e.g. Egbert & Ray (2000); St Laurent *et al.* (2001)) allowed us to improve the representation of diapycnal mixing in the deep ocean. The most recent ocean and general circulation models represent the internal tide-driven mixing through the parameterisation of St Laurent *et al.* (2002), implemented in models by Simmons *et al.* (2004). This parameterisation takes into account the spatial variability of the dissipation rate, and assumes an exponential vertical decay of the energy conversion into internal tides. Different studies investigated the sensitivity of the strength of the ocean circulation to different mixing profiles based on this parameterisation (see for example Jayne (2009); Melet *et al.* (2013) and references therein), but the impact of these different mixing schemes on the transport of tracers is still subject of active research. In this context, the simulations used here have been designed to investigate how diapycnal mixing can impact the distribution of a tracer carried southward by the dense waters formed in the North Atlantic. The simulations have been performed in collaboration with the Australia National University, by using Atlantic sector model described by Snow *et al.* (2015, 2016). While the outputs of the simulations have been made available thanks to an ongoing collaboration, the work presented here is new and the simulations described and used here have not been discussed in any previous publication.

Section 5.1 describes the model employed here; the impact of different mixing profiles on a tracer distribution is presented in section 5.2, while its impact on the upwelling of the tracer in the Southern Ocean is discussed in section 5.3.

5.1 A three-dimensional Atlantic sector model

The model used here is described in detail by Snow *et al.* (2015, 2016) and it is therefore only briefly presented in this section, with a focus on the diapycnal diffusivity used in the model. The model is a 1° horizontal resolution sector model of the Atlantic Ocean, with closed boundaries everywhere except in the Drake Passage, where periodic boundary conditions are applied to simulate the Antarctic Circumpolar Current. To increase the computational efficiency, by minimising the number of land points within the domain, the topography is deformed at each latitude via a linear mapping to a fixed 60° wide section. Despite the deformation, the bathymetry retains the primary features that control the flow, which follows the expected pathways (Snow *et al.*, 2015).

The ocean is modelled with the Modular Ocean Model version 5 (Griffies, 2012) and it is coupled to the GFDL sea-ice simulator (Winton, 2000). The ocean model uses 65 vertical levels, from 10 m thick at the surface to 200 m at depth (over a total depth of 5.5 km). Given the coarse horizontal resolution, the model relies on the parameterisations of Gent & McWilliams (1990) and Fox-Kemper *et al.* (2008) to simulate the contribution of eddies and sub-mesoscale processes to the large-scale circulation. The surface of the ocean is forced with the Coordinated Ocean-Ice Reference Experiments (CORE) normal year wind and buoyancy forcing (Large & Yeager, 2009), deformed in the same way as the bathymetry to match the new domain shape.

The focus of this chapter is to investigate the impact of diapycnal mixing on the distribution of tracers carried by the upper MOC cell. Two simulations with different vertical mixing distributions are compared. Vertical diffusivity is represented in the model through the *K* profile parameterisation (KPP) surface boundary layer scheme (Large *et al.*, 1994), an interior gravity waves mixing scheme (Simmons *et al.*, 2004) and a coastal tidal mixing scheme (Lee *et al.*, 2006) in what will be hereafter called the "low-mixing" case. In what will be hereafter called the "high-mixing" case, the model diapycnal diffusivity is

enhanced by adding the estimates of diffusivity from internal tides and lee waves following Nikurashin & Ferrari (2013), i.e. enhancing the internal wave-driven diffusivity. Both simulations have been run until the model has fully spun up. The basin averaged profiles of diapycnal diffusivity in the model (excluding KPP) for the low-mixing and high-mixing cases are plotted in figure 5.1. They are compared with the profiles of diapycnal diffusivity from the inverse model of Ganachaud (2003) (this estimate is chosen because it is calculated in depth space, and not in density space as in Lumpkin & Speer (2007)), and inferred from the combination of Argo-based dissipation rate estimates in the upper 2000 m with bottom-generated dissipation rate estimates from Nikurashin & Ferrari (2013). Figure 5.1 shows that in the basin interior, at depths of approximately 2 - 4 km, the diffusivity in the three-dimensional simulations lies between the localised (Argo-based and bottom-generated) estimate and the bulk estimate of diffusivity. The diffusivity profiles used in the model are, however, more uniform in the vertical, while both the localised and bulk estimates return a more prominent increase of the diffusivity with depth.

Figure 5.2 shows the zonally averaged diffusivity in the low-mixing and high-mixing simulations (excluding KPP), and their differences. In the high-mixing case, values are of order 10^{-4} m^2s^{-1} in the deep ocean interior (below 2000 m), with peaks up to 10^{-3} m^2s^{-1} above rough topography. These values are up to one order of magnitude larger than in the low-mixing case. Note that diffusivity is set to zero in the last grid point above the ocean bottom, which explains the low values close to the bottom in the zonally averaged diffusivity plots shown in figure 5.2 and the weaker values in the proximity of the ocean bottom in the profiles of the basin average diffusivity in figure 5.1. This pattern represents the change in sign of the vertical gradient of the buoyancy flux in the proximity of the ocean boundaries, where the flux vanishes to respect the condition of no-flux across the boundary. At the ocean boundary, the transformation of water masses into lighter water, with consequent diapycnal upwelling along the boundaries, is represented in the model through the convection scheme in the KPP parameterisation (Snow *et al.*, 2015). In other

words, the vertical diffusion of buoyancy results in the formation of instabilities at the ocean boundaries, with light water sitting below denser water. This instability generates convection, not included in figure 5.2, where only the contribution of internal waves to the diapycnal diffusivity is shown.

The impact of the different diapycnal diffusivities used here on the ocean dynamics and on the distribution of a tracer carried by the upper overturning cell in the Atlantic Ocean is presented in the next section.

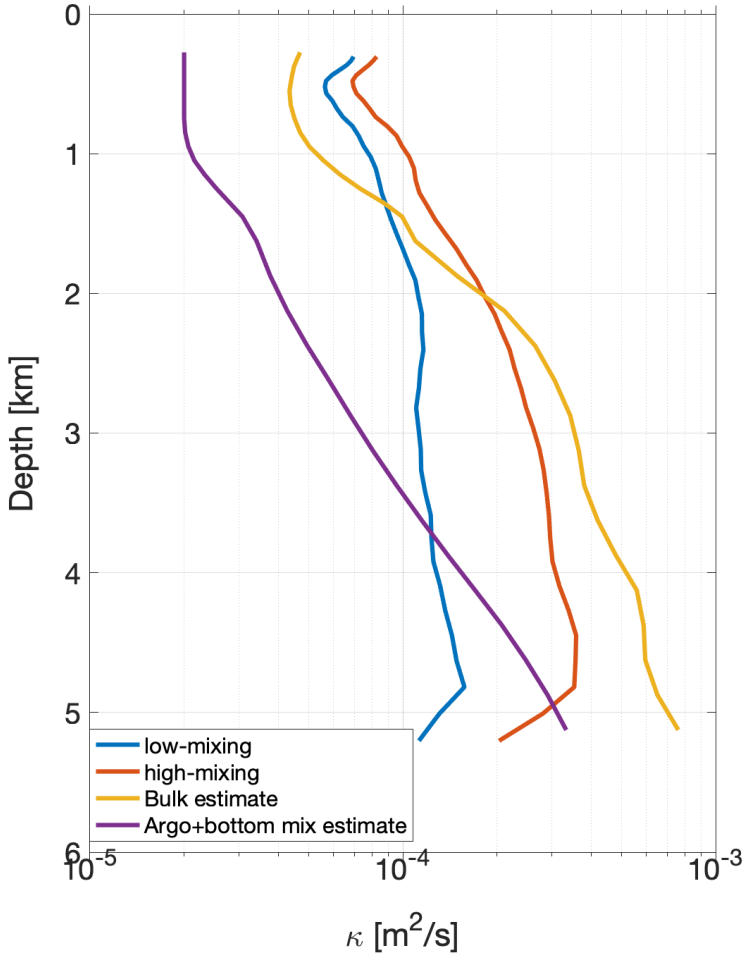


Figure 5.1: *Basin-average diapycnal diffusivity as a function of depth for the (blue) low-mixing and (red) high-mixing simulations. As a comparison, the diapycnal diffusivity from (yellow) an inverse estimate (Ganachaud, 2003) and (purple) based on Argo floats and estimates of bottom-generated mixing (Whalen* et al.*, 2012; Nikurashin & Ferrari, 2013) are also shown.*

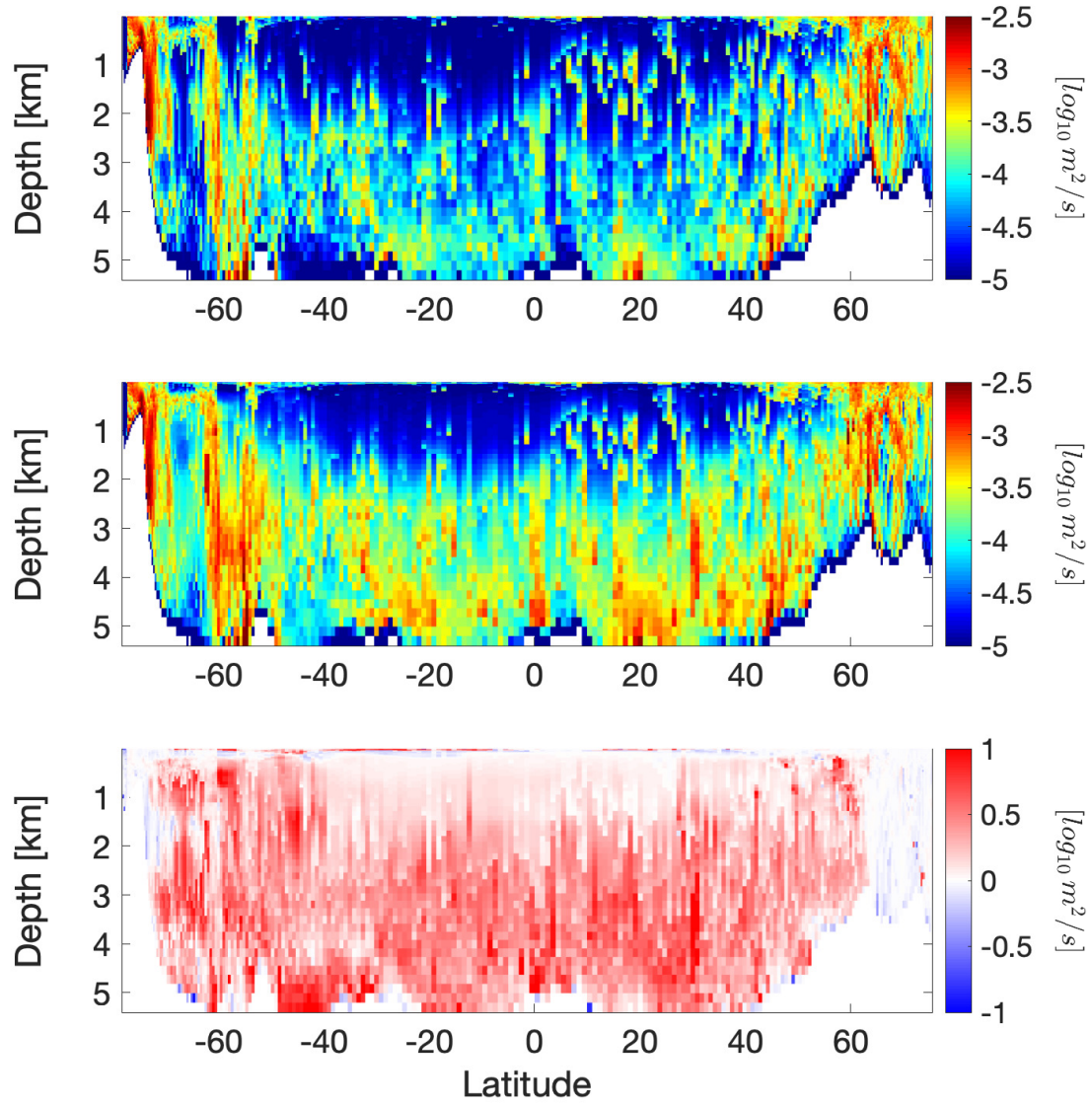


Figure 5.2: *Zonally averaged diapycnal diffusivity in the (top) low-mixing and (middle) high-mixing simulations. (Bottom) Difference in the zonally averaged diapycnal diffusivities (high-mixing - low-mixing). All the panels are plotted on a logarithmic scale.*

5.2 Tracer mixing in the Atlantic Ocean

Figure 5.3 shows the model overturning streamfunction, i.e. the zonal and vertical integral of the meridional velocities, for the low-mixing and high-mixing cases. The meridional

transport shown in figure 5.3 is given by the sum of the Eulerian mean and the bolus transports, the latter representing the component of the transport due to unresolved mesoscale eddies that are parameterised in terms of resolved quantities through the parameterisation of Gent *et al.* (1995). The sum of the Eulerian and bolus transports is referred to as the "residual" transport, which is responsible for the advection of tracers.

In both simulations, the upper cell of the MOC is both shallower and weaker than in observations: it reaches a maximum depth of approximately 1800 m, instead of reaching down to approximately 3500 m (Talley *et al.*, 2003; Lumpkin & Speer, 2007; Kuhlbrodt *et al.*, 2007), and the maximum transport is $\sim$ 7 Sv, in comparison with the 17-19 Sv observed by the RAPID array at 26°N (Smeed *et al.*, 2014; McCarthy *et al.*, 2015), estimated by inverse estimates (Talley *et al.*, 2003; Lumpkin & Speer, 2007) or by the Estimating the Circulation and Climate of the Ocean (ECCO) ocean state estimate (Cessi, 2019). The strength and depth of the upper cell are strongly connected with the steepness of the isopycnals in the Southern Ocean and their depth throughout the Atlantic basin, as described in section 1.2. The steepness of the isopycnals in the re-entrant channel is set by a balance between the effect of the westerly winds, which tend to steepen them, and the formation of baroclinic eddies, which tend to flatten them. The isopycnals are too shallow and flat in this sector model, which, being forced with realistic forcing over the Atlantic, does not capture the effect of steepening of the isopycnals in the Pacific Ocean, where baroclinic eddies are weaker than in the Atlantic Ocean (Stevens & Killworth, 1992; Smith, 2007).

The strength and depth of the upper cell are directly connected with the time it takes a tracer to be carried from the North Atlantic to the Southern Ocean. With a weaker overturning transport, the flow and the tracer are exposed to diapycnal mixing for a longer time, thus potentially increasing the diffusive length scale of a tracer, i.e. the extent to which a tracer can vertically spread while carried southward by the upper cell of the MOC. On the other hand, given that mixing is predominantly bottom-enhanced, it has a minor impact on a tracer carried by the upper MOC in the case of a shallower cell. While such caveats need

to be taken into account, the sector model overturning streamfunction has the right order of magnitude and correctly catches the pathways of the upper and lower cells (see figure 5.6 below).

The model's upper cell is almost insensitive to the increase in the diapycnal diffusivity (figure 5.3), while the lower cell gets stronger in the high-mixing case, as expected given that the lower cell's streamfunction is proportional to diapycnal mixing (section 1.2), and in agreement with previous studies (e.g. Bryan (1987); Marotzke (1997); Nikurashin & Vallis (2011, 2012); Mashayek *et al.* (2015)). The lower cell returns a maximum transport of approximately -2.2 Sv and -3.1 Sv in the low-mixing and high-mixing cases, respectively. These values are comparable both with inverse estimates (Lumpkin & Speer, 2007) and ocean state estimates (e.g. see Cessi (2019)).

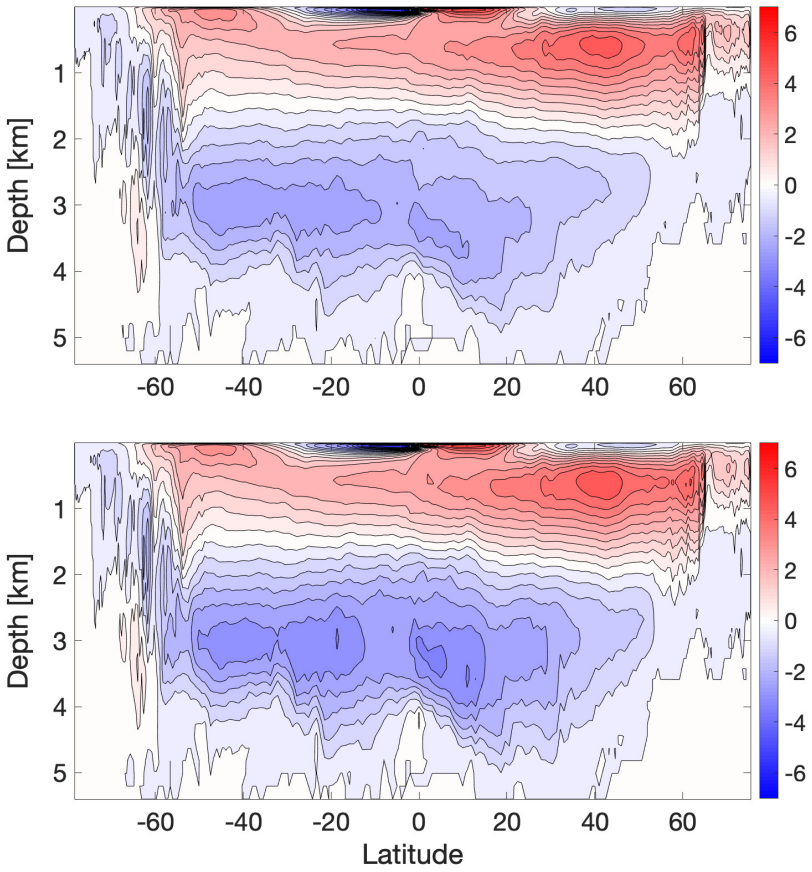


Figure 5.3: *Overturning streamfunction for the (top) low-mixing case and (bottom) high-mixing case. Contours are plotted every 0.5 Sv in both panels.*

To investigate the effect of different diapycnal diffusivities on the distribution of a tracer carried by the upper overturning cell, a tracer has been injected at the surface of the ocean in the northern hemisphere. The tracer concentration is set to 1 in the northernmost grid point in the North Atlantic and linearly decays with latitude to 0 at the equator, and the model is subsequently run for 500 years. The temporal evolution of the zonally averaged tracer concentration in the low-mixing and high-mixing simulations, as well as the difference between the two, is shown in figure 5.4. Note that all the panels have the same color-scale, showing the dilution of the tracer in the water column over time. Note also that the overturning streamfunction is super-imposed.

The tracer is rapidly mixed in the deep convection region in the North Atlantic and from there it enters the southward flow of dense waters, while mixing with the underlying lower cell. The tracer clearly mixes more with the dense waters of the lower cell in the high-mixing case, and the difference between the two cases shows a clear separation between regions with more and less tracer. This separation sits initially at the interface between the upper and lower cells, and slowly moves deeper with time as the tracer "leaks" from the upper cell and enters the lower cell. Tracer concentration anomalies are visible from about 100 years after the tracer injection, but note that the maximum positive and negative differences in tracer concentration are not located at the same latitude (bottom panels in figure 5.4). The largest positive anomaly is located in the North Atlantic, and more broadly in the northern hemisphere, throughout the whole simulation. This pattern is determined by the fact that the equatorial region acts as a barrier (visible in the second column in figure 5.4) and generates a zonal recirculation within the northern hemisphere, acting to keep the tracer within this hemisphere for a longer time. Moreover, the upper cell transport in this model is not as strong as in reality, therefore increasing the time over which mixing can change the tracer distribution before the southward flow crosses the equator. In contrast, the largest negative anomaly, at the end of the simulation, is located between 30°N and 30°S and between 500 m - 2000 m approximately. This pattern indicates that the tracer

leaks from the southward flowing waters in both direction, i.e. it is mixed not only with the denser waters below, but partially also with the lighter waters above, therefore returning back to the North Atlantic via shallow northward flowing waters and so recirculating within the Atlantic Ocean.

To better quantify how the amount of tracer changes with depth and latitude as the tracer is entrained in different water masses on its way southward, figure 5.5 shows the decadal mean percentage of the tracer calculated in 10°-wide latitudinal sections from 70°N to 70°S. The solid and dashed lines show the percentage for the low-mixing and high-mixing cases, respectively, and the line colours indicate different time intervals, every 50 years from 10 years after the model injection (darkest blue) to 500 years (brightest yellow). Figure 5.5a shows the tracer percentage calculated over the whole water column, thus it does not take into account the differences in the tracer distribution in depth

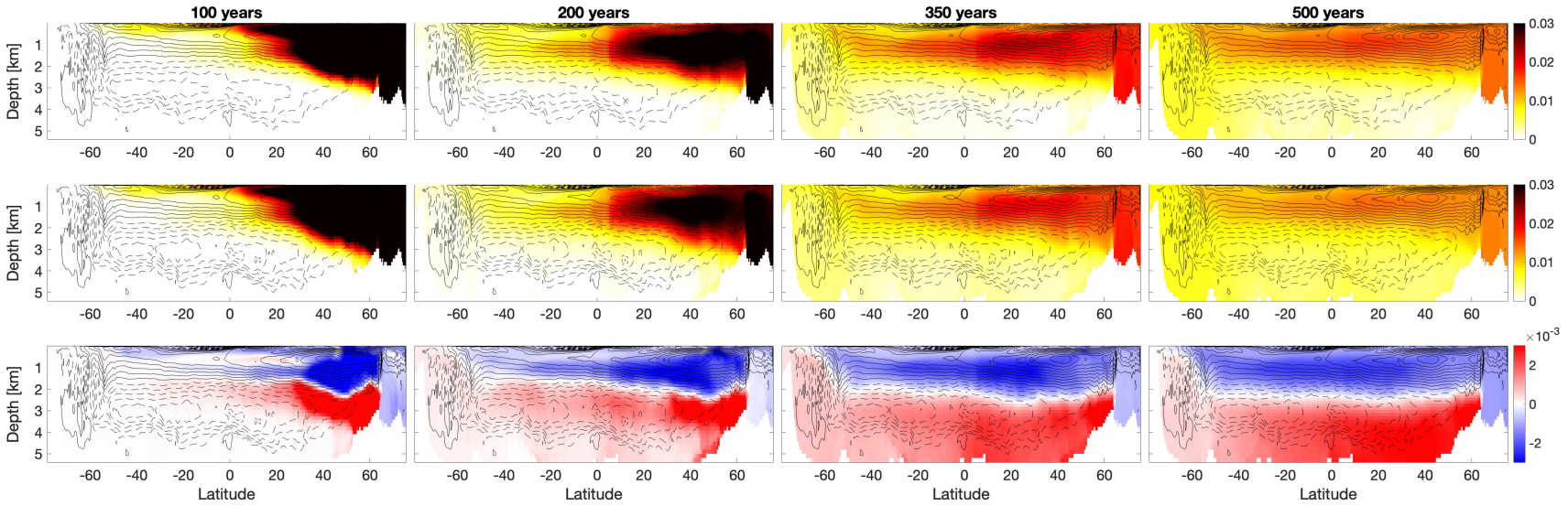


Figure 5.4: *Zonally averaged tracer concentration from the three-dimensional semi-realistic model. The tracer (colors) is injected at the surface of the ocean in the northern hemisphere (set to 1 in the last grid point in the North Atlantic and linearly decaying to 0 at the equator) and is here plotted 100, 200, 350 and 500 years after the injection. The overturning streamfunction is shown in black contours; contours are every 1 Sv and negative contours are dashed. Top panels correspond to the low-mixing case, middle panels to the high-mixing case and the bottom panels show the difference between the two cases (high-mixing - low-mixing). The overturning streamfunction of the high-mixing case is also shown in the bottom panels.*

and explains why the low-mixing and high-mixing simulations return almost exactly the same result. In both cases, the percentage of the tracer in the northern hemisphere decreases over time as the tracer is carried southward, and at the end of the simulation the tracer percentage in each of the two hemispheres is almost exactly 50% (~50.5% in the northern hemisphere and ~49.5% in the southern hemisphere).

Figure 5.5b and 5.5c show the tracer percentage in the upper 1800 m (which is approximately the limit between the upper and lower cells in a zonally averaged sense), and from 1800 m to the bottom, respectively. Most of the tracer remains in the upper 1800 m of the water column, with some differences between the different mixing scenarios: about 70% and 60% of the tracer remains within the upper 1800 m in the low-mixing and high-mixing cases, respectively. The remaining 30% and 40%, respectively, enters the lower cell, and while part of it is still carried southward by the upper branch of the lower cell, 8% (low-mixing) and 15% (high-mixing) of the total tracer is mixed below 3000 m (not shown), i.e. enters the deeper northward branch of the lower cell. The implications of such differences on the tracer upwelling in the Southern Ocean and its residence time in the Atlantic Ocean will be discussed later (see figures 5.7-5.8 below).

The differences in the zonally averaged tracer concentration indicate that mixing can play a primary role in determining the residence time, distribution and exchange rates of tracers carried southward by the upper cell, but to be able to fully describe the tracer distribution and its exchange between different water masses, it is necessary to analyse a three-dimensional picture, that takes into account both the pathways of the upper overturning cell and the spatial variability of mixing.

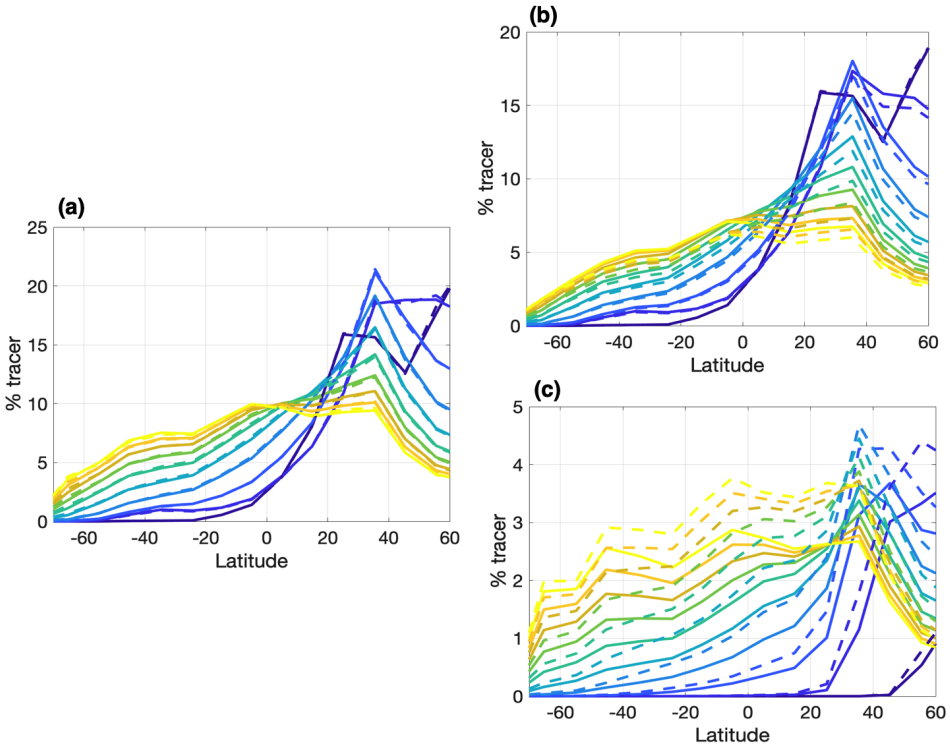


Figure 5.5: *Decadal mean percentage of the tracer in 10°-wide latitudinal sections (i.e. the percentage at each point is calculated in a section between ±5° from that point) calculated (a) over the total depth, (b) in the upper 1800 m, and (c) between 1800 m and the ocean bottom. The solid and dashed lines show the percentage for the low-mixing and high-mixing cases, respectively. Line colors indicate different timesteps, every 50 years from 10 years after the model injection (darkest blue) to 500 years (brightest yellow).*

The pathways of the circulation at different depths are shown in figure 5.6. The top row (panels a-d) shows the time-mean barotropic streamfunction and the circulation streamlines at different depths from the three-dimensional model, while the bottom row (panels e-h) shows the same results from the ECCO ocean state estimate. The streamlines are superimposed over the velocity field (cyan arrows), which helps identify the areas where the flow is stronger. Note that all the panels in the top row of figure 5.6 correspond to the high-mixing case averaged over the last 100 years of the simulation, but the results for the low-mixing case are not significantly different, especially in the upper ocean (not shown). The barotropic streamfunction, calculated from the depth integrated zonal velocities, shows the expected gyres, western boundary currents and near-zonal flows of the upper ocean circulation. The atmospheric winds over the surface of the ocean generate gyres, i.e. large-

scale recirculations between the continents; in particular, the surface circulation at mid-latitudes is characterised by the anti-cyclonic subtropical gyre, while high-latitudes in the northern hemisphere are characterised by a cyclonic subpolar gyre. A key feature of the gyre circulations are the intense flows along the western side of the ocean basin, known as western boundary currents, which compensate in a narrow region for the meridional transport of the gyres over the basin interior. Western boundary currents are an energetic component of the upper ocean circulation, with velocities up to 1 m s^{-1}, and are important contributors to the transport of heat from equatorial to polar regions. Finally, easterly trade winds in the tropics and westerly winds in the high latitudes generate strong zonal currents that characterise the equatorial region and the Southern Ocean. The absence of continental barriers between Antarctica and the northern land masses allows the formation of a quasi-zonal current around Antarctica, the Antarctic Circumpolar Current.

The upper ocean circulation in the Atlantic sector model is weaker than in the real ocean: the gyres are up to 14 Sv instead of $\sim 20 - 30$ Sv (see comparison with ECCO and Talley *et al.* (2011); Williams & Follows (2011)), and the Antarctic Circumpolar Current reaches a maximum of about 45 Sv, around one third of the observed value (Meredith *et al.*, 2011). Also, the circulation in the sector model is too zonal in comparison with observations (e.g. Reid (1994)) and with the ECCO state estimate. A crucial feature of the circulation beneath the upper ocean gyres (figures 5.6c and 5.6g) is the meridional flow of the dense waters formed in the North Atlantic. Most of the southward flow of the upper cell takes place close to the western boundary, i.e. in the form of a deep western boundary current, as shown by the streamlines and velocity field in figure 5.6c and 5.6g, with recirculation in the basin interior. Underlying the upper cell (figure 5.6d and 5.6h), the northward flow of the lower MOC cell fills the western South Atlantic, until it separates at the equator through the Romanche Fracture Zone, from where it spreads in both western and eastern North Atlantic basin, as well as flowing back southward in the eastern South Atlantic (Stephens & Marshall, 2000).

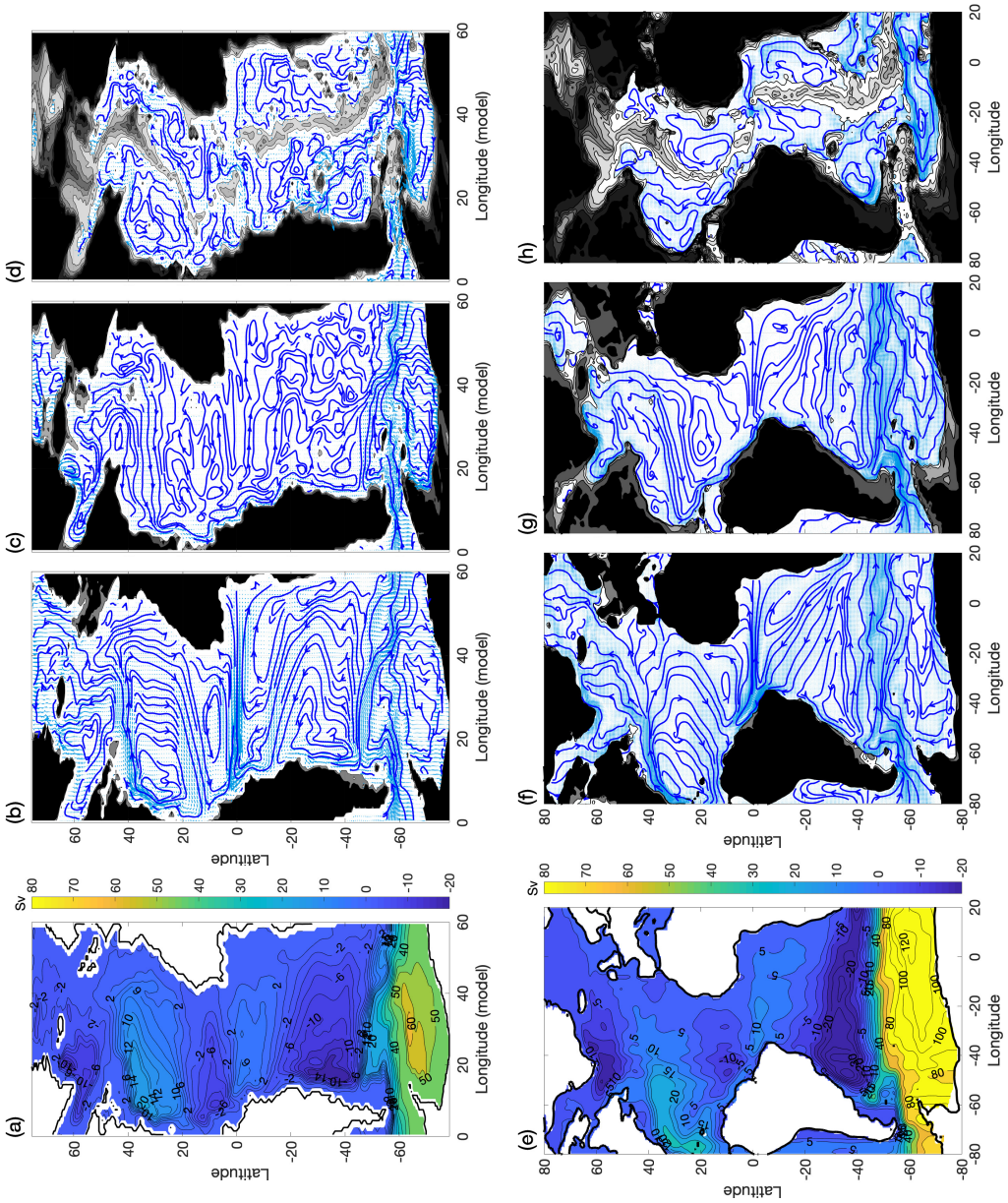


Figure 5.6: *(a,e) Time-mean barotropic streamfunction and streamlines at (b-d, f-h) 100 m, 1500 m and 3500 m in the Atlantic sector model (top row) and in the ECCO state estimate (bottom row).*

The comparison of the ocean circulation in the sector model with the ECCO state estimate shows that the model, despite its bathymetric alterations, captures the main features of the ocean circulation, and the flow overall follows the expected pathways. In the sector model, the low-mixing and high-mixing experiments return a qualitatively similar deep circulation, but the transport of the lower cell is stronger in the high-mixing case, as already clear from figure 5.3.

Knowledge of the pathways of the upper and lower cells is particularly important to estimate the amount of mixing that a tracer can experience while advected by the overturning circulation. The large spatial variability of diapycnal mixing can generate significantly different scenarios: tracers can be upwelled, if brought into contact with regions of rough topography or carried along the ocean bottom boundaries, or downwelled, if carried in the ocean interior in regions where mixing increases with depth. Figures 5.7 and 5.8 (top rows) show the diapycnal velocity for the low-mixing and high-mixing cases, respectively. The diapycnal velocities have been calculated from a decadal mean of the model diffusivity and stratification as per equation 3.6, and assuming that diapycnal mixing can be approximated through the diapycnal diffusivity as per equation 2.25. Diapycnal velocities in figures 5.7 and 5.8 are shown on the different depth levels of 1000 m, 2000 m, 3000 m and 3600 m from left to right, respectively. Note that a section in depth crosses different isopycnals: it crosses denser isopycnals in the high latitudes (where isopycnals outcrop to the surface) and lighter isopycnals in the ocean basin (where isopycnals are approximately flat).

Diapycnal velocities show large spatial variability, especially close to the ocean bottom. Values are mainly positive in the upper ocean (left panel), where mixing is surface enhanced, and negative deeper down, where mixing begins to increase with depth (left-middle panel). The signal of bottom enhanced mixing, leading to negative diapycnal velocity, is particularly evident in the proximity of the Mid-Atlantic Ridge, which dominates the signal in the whole basin at 2000 m and in the high-latitude North Atlantic at 1000 m.

In the deeper ocean (right-middle and right panels), diapycnal velocities return negative

values as long as the buoyancy flux keeps increasing with depth. In close proximity to the ocean boundary, diapycnal velocities return positive values, due to the change in sign of the buoyancy flux vertical gradient. The high-mixing case returns larger diapycnal velocities at all depths and especially larger diapycnal downwelling over the Mid-Atlantic Ridge (left-middle and right-middle panels) and larger diapycnal upwelling in proximity to the ocean bottom (right-middle and right panels). Note that there are differences in the spatial pattern of diapycnal velocities between the low-mixing and high-mixing cases in a few locations, especially close to the ocean bottom (for example, in the east South Atlantic). Such changes are due to differences in the vertical divergence of the buoyancy flux between the different cases.

The bottom rows of figures 5.7 and 5.8 show a decadal mean of the distribution of the tracer 500 years after its injection at the ocean surface. The tracer distribution is shown at the same depth levels as the diapycnal velocity shown in the top rows. The differences between the low-mixing (figure 5.7) and high-mixing (figure 5.8) cases clearly show that the tracer is more concentrated in the upper ocean in the low-mixing case (left and left-middle panels), while more of the tracer has been mixed into the denser waters below in the high-mixing case. Consequently, the same tracer is more abundant in the deeper ocean in the high-mixing case (right-middle and right panels).

The patterns of tracer concentration in the low-mixing and high-mixing scenarios also return information about the ocean overturning circulation. Most of the tracer is concentrated on the western side of the basin, consistent with the fact that most of the transport takes place in the form of a deep western boundary current. The spatial distribution of the tracer concentration at 1000 m shows that the tracer, while mainly concentrated along the western boundary, is zonally distributed and diluted in the basin interior (figure 5.6). The signature of the deep western boundary current is clearly visible at 2000 m, extending from the North Atlantic all the way to the Southern Ocean.

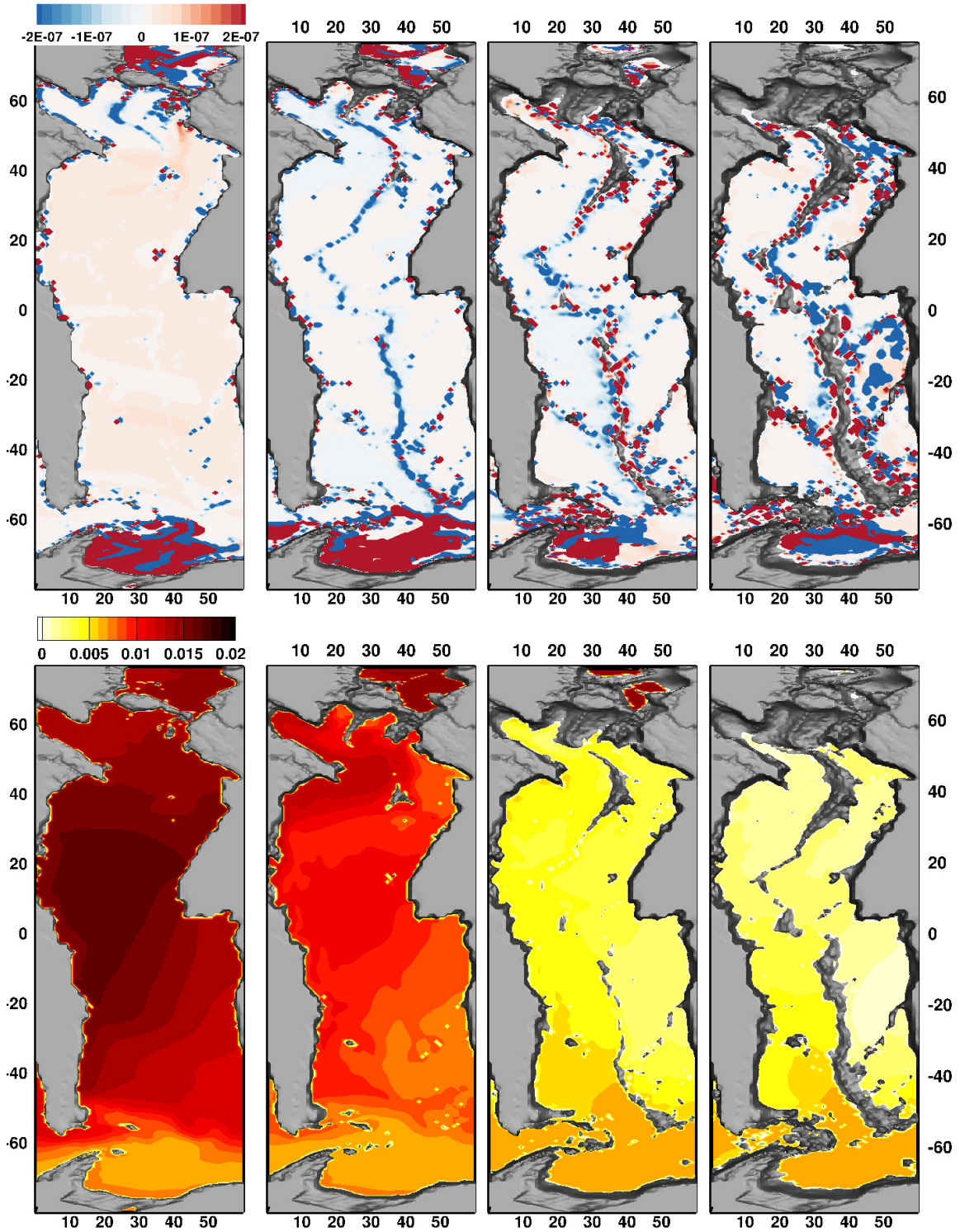


Figure 5.7: *(Top row) Diapycnal velocity (m/s) for the low-mixing case at depths of 1000 m, 2000 m, 3000 m, and 3600 m from left to right, respectively. (Bottom row) Decadal mean of the (dimensionless) concentration of a tracer 500 years after it has been injected at the surface of the ocean in the northern hemisphere, shown at the same depth levels as for the top row.*

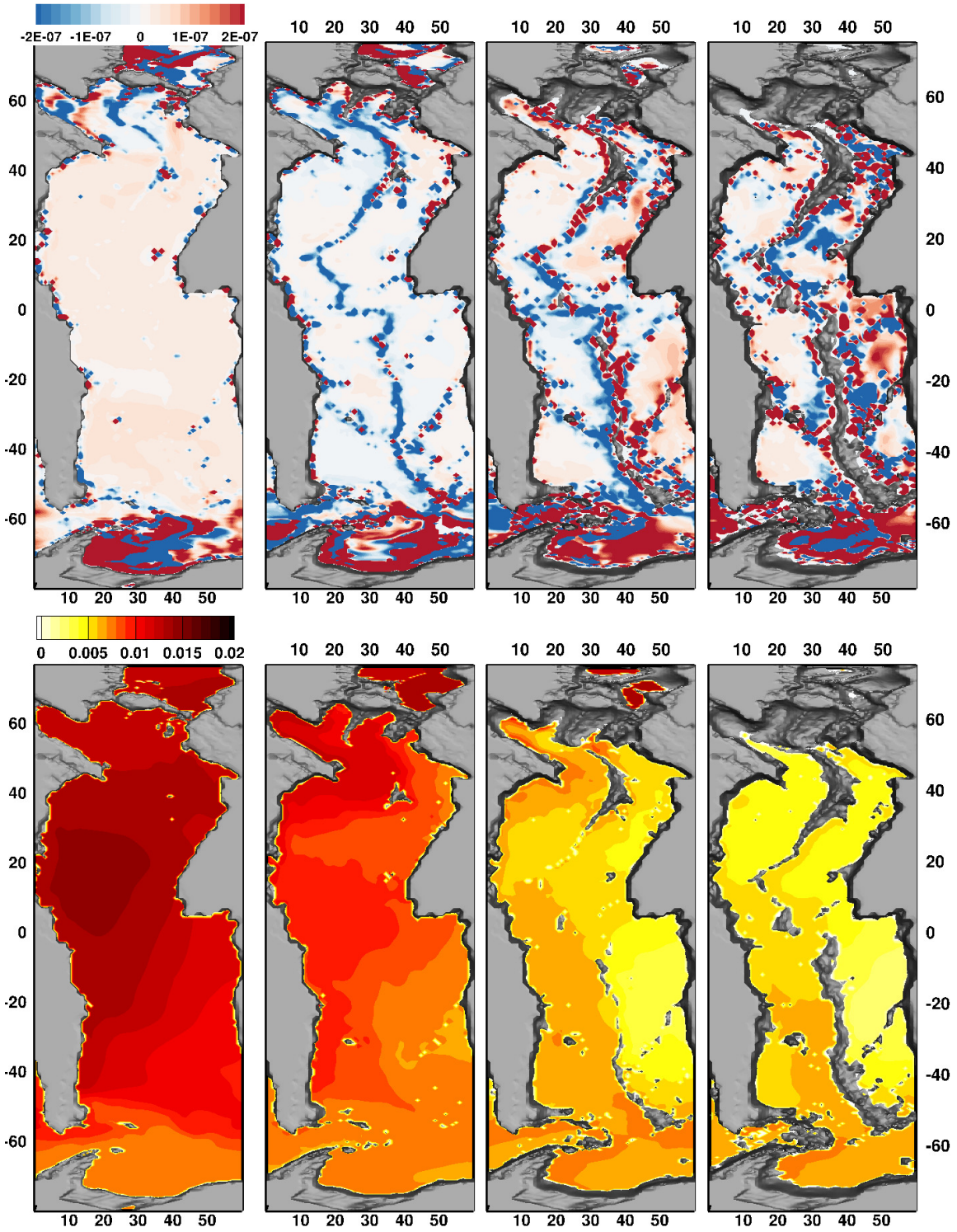


Figure 5.8: *Same as in figure 5.7 but for the high-mixing case.*

The tracer concentration at this depth also shows a clear recirculation, especially around the equatorial region, which plays an important role in ventilating the basin interior while

delaying the equatorward transport (Fine, 2011). Indeed, it has been shown both through float data and CFC data (e.g. Rhein (1994); Lozier (1997); Bower *et al.* (2009)) that water parcels are not transported southward in a direct way along the western boundary, but follow mainly interior pathways, spending a considerable amount of time in deep recirculations and eddies (Fine, 2011).

The signature of the dense southward flowing waters of North Atlantic origin has almost completely vanished in the low-mixing case while it is still visible at 3000 m in the high mixing case, a consequence of the stronger mixing that tends to deepen the stratification in the ocean interior, and so allows a deeper upper cell. The upper cell is also strengthened in the high-mixing case by the waters of the lower cell that upwell into the lighter waters above, feeding the southward flow. In both low- and high-mixing cases, the tracer concentration at 3000 m also returns a clear signature of the waters of the lower cell flowing northward. The tracer concentration in these waters is large after the tracer has been upwelled in the Southern Ocean, mixed within the deep convection regions around Antarctica and entrained in the dense waters formed there.

The pathway of the deep branch of the lower cell in its journey northward is clearly visible from the tracer concentration at 3600 m. The dense waters formed around Antarctica flow northward in the western South Atlantic until they reach the Romanche Fracture Zone (close to the equator), through which they can cross the Mid-Atlantic Ridge, flowing northward in both the eastern and western North Atlantic basin as well as turning southward in the eastern South Atlantic. As already noted in figures 5.4 and 5.5, comparison of tracer concentrations at 3000 m and 3600 m between the two cases (right-middle and right panels in figures 5.7 and 5.8) reveals that the tracer is more concentrated in the dense waters of the lower cell in the high-mixing case. This pattern indicates that in the case of stronger mixing a larger amount of tracer is entrained in the lower cell waters, whereas a larger fraction enters the lighter waters that return to the North Atlantic in the case of weaker mixing. The next section analyses in more detail the impact of diapycnal mixing on the upwelling of the

tracer in the Southern Ocean, which affects its redistribution throughout the whole basin.

5.3 Tracer upwelling in the Southern Ocean

As discussed above and shown in figures 5.4, 5.7 and 5.8, the tracer is exported to the deep ocean not only through mixing along its southward journey, but also because part of it upwells in the Southern Ocean in regions which provide the source waters for the lower cell. Indeed, as described in chapter 4, the pathway of different water masses, and of the tracers that they carry, is crucially dependent on the location in which they upwell in the Southern Ocean. The denser waters upwell further south, closer to the marginal seas where the abyssal waters of the lower cell are formed, whereas lighter waters upwell further north, where the positive buoyancy flux at the surface transforms them into intermediate waters that flow northward at shallower depths. Here we show that a different amount of mixing can affect the distribution of tracers by changing where they will upwell in the Southern Ocean.

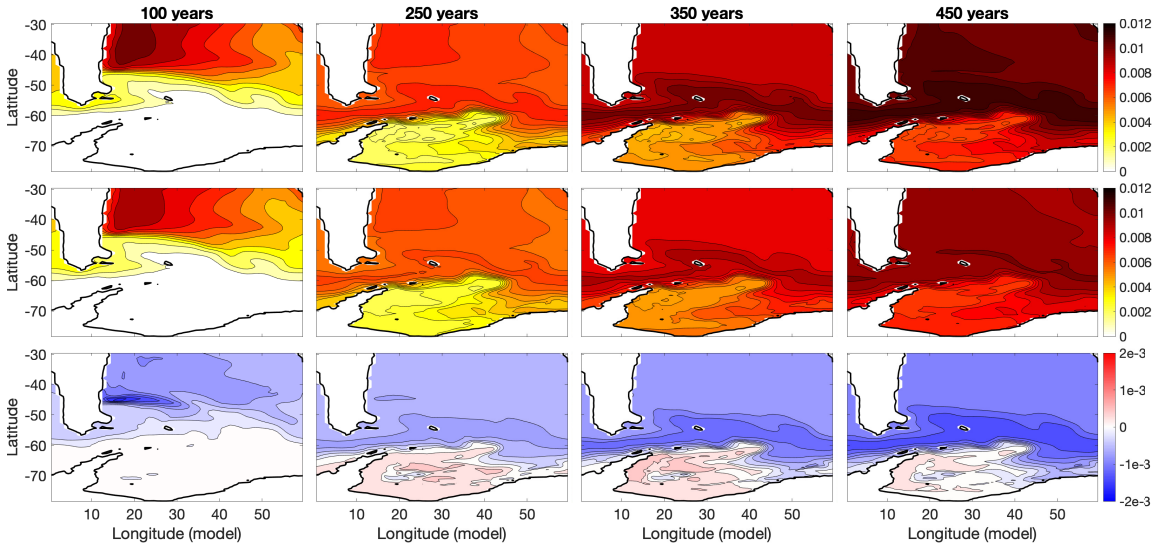


Figure 5.9: *Tracer concentration (decadal mean) in the Southern Ocean at 200 m for different time intervals (indicated in the title) after the tracer injection at the surface. Top and middle rows show the results for the low-mixing and high-mixing cases, respectively. Bottom row shows the difference between the two cases (high-mixing - low-mixing).*

Figures 5.9 shows the decadal mean concentration of the tracer in the low-mixing and high-mixing cases, as well as their difference, at 200 m for different times after the tracer has been injected at the surface of the ocean. The first column, 100 years after the injection, shows that the tracer is transported by the subtropical gyre in the South Atlantic and is diluted while zonally recirculating in the Atlantic Ocean. While the two experiments show a very similar pattern, the tracer concentration in the subtropical gyre is larger in the low-mixing case, as expected. However, after about 250 years the signal of the dense, tracer-enriched waters upwelling in the Southern Ocean becomes clearly visible. In particular, the two middle columns in figure 5.9 present the tracer concentration 250 and 350 years after the injection, showing the increase in tracer concentration mainly south of 50°S due to the upwelling of dense waters. Looking at the difference between the two cases (bottom row), it is possible to observe that a larger amount of tracer upwells further north, in a band approximately between 50-60°S, in the low-mixing case, while more of it upwells further south, in the Weddell Sea, in the high-mixing case. Comparing these upwelling patterns with the surface buoyancy flux, shown in figure 5.10, it becomes clear why a larger fraction of the tracer is entrained in the lower cell in the high-mixing case. In the high-mixing experiment, a larger fraction of the tracer (see figures 5.4 and 5.5) is carried by the southward flowing waters which upwell close to Antarctica, where the buoyancy flux is negative and such waters are transformed into AABW. On the contrary, in the low-mixing experiment a larger fraction of the tracer remains confined within the lighter southward flowing waters, which partially upwell in a region of positive buoyancy flux, where they are transformed into northward flowing intermediate waters.

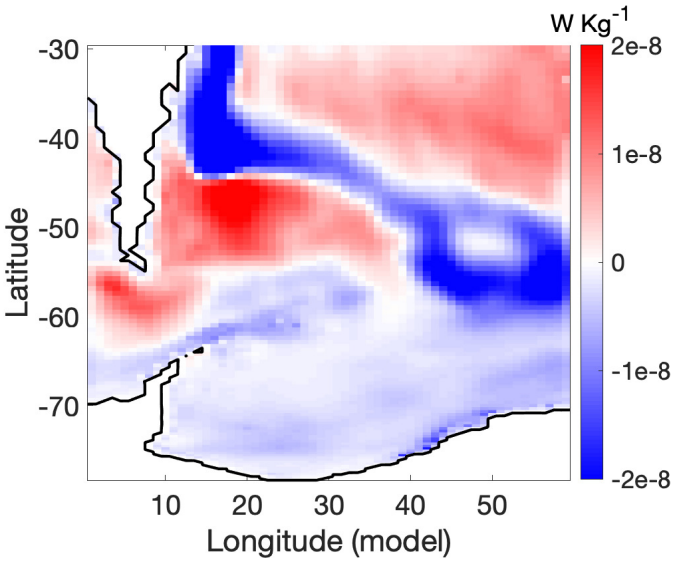


Figure 5.10: *Surface buoyancy flux in the Southern Ocean in the model. Positive values indicate a buoyancy flux into the ocean, i.e. waters are gaining buoyancy.*

5.4 Summary and conclusions

In this chapter, two numerical simulations with different diapycnal diffusivities have been used to show that diapycnal mixing has a significant impact on the distribution of tracers carried by the southward flowing waters of the upper MOC cell. It has been shown that diapycnal mixing does not significantly affect the dynamics of the upper overturning cell in the Atlantic Ocean (and moderatly increases the lower cell). However, it strongly affects how deep a tracer taken up in the North Atlantic can penetrate in the water column, and the extent to which it can be exchanged with different water masses. In particular, around 70% of a tracer injected at the surface of the ocean in the northern hemisphere remains confined within the upper cell waters in the case of weak mixing. In this scenario, most of the tracer remains within the lighter waters flowing to the Southern Ocean and only a small fraction upwells in the marginal seas around Antarctica to be entrained into the abyssal northward flowing waters of the lower cell. Only 8% of the total tracer concentration is mixed with the northward branch of the lower cell. On the contrary, in the case of stronger mixing, tracers within the upper cell are exchanged with the waters of the lower cell while carried

southward (figures 5.4 and 5.8). Up to 15% of the total tracer concentration is exchanged with the northward branch of the lower cell, both due to enhanced mixing on the way southward and because a larger amount of tracer upwells in the Weddell Sea, where the abyssal waters of the lower cell are formed, entraining the tracer upwelled here. It follows that the residence time of the tracer will be different in the above two scenarios. In the former case, most of the tracer will be brought back into contact with the atmosphere after being taken up by intermediate waters, hence with a much faster timescale than in the case of mixing with the lower cell. In the latter case, a good fraction of the tracer is sequestered in the lower cell, where it can be stored for several centuries.

These results indicate that a good representation of diapycnal mixing is crucial to capture the right tracer distribution and residence time, which can have important consequences for the understanding and prediction of global climate. Consider, for example, the transfer of a heat anomaly from the North Atlantic to the Southern Ocean in the current warming climate, which has been shown to be crucial in regulating how the Southern Ocean is going to warm in the coming decades. Indeed, while the Southern Ocean has shown a little temperature change in the last few decades, the Arctic Ocean has warmed much more than the global average, and it is currently a topic of intense research to understand where and when the heat carried by the upper cell is going to affect the Southern Ocean circulation and climate, with implications for the global MOC. In fact, while several processes contribute to the temperature differences between the two polar regions and to the regulation of their transient and long term responses to global warming, it has been shown that the Southern Ocean warming delay is largely driven by the ocean meridional overturning circulation (Marshall *et al.*, 2014; Armour *et al.*, 2016; Rintoul, 2018).

As atmospheric temperatures increase and heat the ocean surface, in the Southern Ocean the excess of heat is exported north by the wind-driven northward Ekman transport, and subsequently carried into the ocean interior by the formation of intermediate waters (Rintoul, 2018). Consequently, warming is delayed south of the ACC, from which heat is

removed, and enhanced north of the ACC, where heat is accumulated. The deep waters upwelling in the Southern Ocean have not been affected yet by the temperature increase in the North Atlantic, therefore the warming of the Southern Ocean surface is going to be set by the time it takes for the deep ocean waters to be warmed themselves (Armour *et al.*, 2016). Diapycnal mixing can affect such timescales by exchanging heat between different water masses, which upwell in the Southern Ocean with different timescales and at different locations. It is thus necessary to have a good representation of diapycnal mixing in climate models in order to correctly predict where and when the waters around Antarctica are going to get warmer.

As any numerical study, the simulations used here have some caveats that might affect our results and that challenge a quantitative comparison between the results obtained here and the real ocean. First of all, the diffusivity used here has a weaker vertical gradient than the diffusivity inferred from inverse estimates or observation-based estimates of the dissipation rate (figure 5.1). This pattern is a consequence of the choices made in the parameterisation of diapycnal mixing in the model, and it might overestimate the amount of mixing that a tracer experiences in the ocean interior. Secondly, the upper cell in this model is too shallow and too weak, which might affect the results in two opposing ways: (i) tracers are transported too slowly, allowing for more time to be exposed to mixing, but (ii) they might not experience enough of the bottom enhanced mixing. Due to the weaker overturning transport, it is also challenging to draw any conclusion on the transport time needed to carry a tracer from the North Atlantic to the Southern Ocean. In the simulations used here, it takes at least 200 years for the tracer to upwell to the Southern Ocean, while observations from CFCs (e.g. Rhein (1994); Fine (2011)) indicate a shorter timescale of about 100 years. Finally, the model used here is limited to the Atlantic Ocean only, which has clear computational advantages, but does not allow us to investigate the global fate of the tracer after its upwelling in the Southern Ocean. In particular, the tracer entrained in the abyssal waters could potentially be carried in all the ocean basins through the northward

flow of abyssal waters. Despite these caveats, the results shown here indicate that diapycnal mixing can play an important role in the Atlantic Ocean by vertically displacing tracers while they are carried southward, affecting their basin - and potentially global - distribution and residence time.

Chapter 6

Conclusions

The research presented in this thesis has explored the effect of diapycnal mixing on the global meridional overturning circulation, and especially on the upper cell in the Atlantic Ocean. It has examined the role of diapycnal mixing in the closure of the upper and lower overturning cells and in regulating the distribution of tracers carried southward from the North Atlantic to the Southern Ocean.

This thesis had three main questions, which we report below together with each respective answer, a discussion of the results found, and a short summary of the thesis altogether.

The different mechanisms that lead to the formation of internal waves, the breaking of which generates diapycnal mixing, were described in Chapter 2, along with the theoretical background describing diapycnal mixing. We also described how diapycnal mixing can be inferred from observed quantities, in particular from estimates of the turbulent kinetic energy dissipation rate.

Question 1 *Spatially variable versus constant parameterisations in mixing estimates: how do they shape the patterns of diapycnal upwelling/downwelling in the global ocean?* To infer mixing from the dissipation rate estimates requires knowledge of two parameters: (i) the local breaking efficiency (q_t), representing the fraction of internal tide energy spent

locally (i.e. close to where the waves have been generated) due to wave breaking, and (ii) the flux coefficient (Γ), representing the percentage of the turbulence generated by an internal wave breaking event that is converted into diapycnal mixing. As these parameters are often assumed to be constant in ocean and climate models, the work presented in Chapter 3 explored the sensitivity of diapycnal mixing and of the mixing-induced circulation to spatially variable q_t and Γ. We build on previous estimates of spatially variable q_t and Γ to investigate their effect on diapycnal mixing when these parameter are varied independently or *in tandem*. In particular, we used the estimate of spatially variable q_t from Vic *et al.* (2019), and combine it with the parameterisation of a variable flux coefficient following Mashayek *et al.* (2017*c*).

It was shown that the use of spatially variable coefficients has important consequences for both the spatial patterns of the diapycnal velocities and for the net water mass transformation. It is important to co-vary these parameter to not over-estimate the rates of water mass transformation. Also, spatially variable parameters alter the patterns of diapycnal mixing, increasing or decreasing the rates of diapycnal upwelling and downwelling in different locations. These spatial patterns are important in setting the exchange rates of water masses and tracers, affecting the tracer pathways and timescales in the deep ocean.

As we improve our knowledge on the different sources of internal waves and on how to parameterise their effects on the global circulation, the results presented here indicate that it is timely and needed to incorporate these spatially variable parameters in ocean and climate models in order to move towards a better representation of the patterns of diapycnal mixing and the rates at which dense waters are transformed in the deep ocean. For example, a more accurate representation of mixing in climate models can improve their skills to predict how heat and other climatically important tracers will upwell in the Southern Ocean around Antarctica.

Chapter 3 also investigated the contribution of different processes to the diapycnal mixing that regulates the strength of the lower overturning cell. We take into account two of

the dominant sources of internal waves in the deep ocean, i.e. internal tides and lee waves, but there are other important processes that have been left out due to the present insufficient knowledge. We found that internal tides contribute globally about 7 Sv, while the geothermal heat flux contributes an extra 4-5 Sv. Lee waves are particularly important in the Southern Ocean and their contribution is variable with density: they contribute to a net upwelling for the densest isopycnals ($\gamma^n = 28.2 - 28.3$), and to a net downwelling for lighter density surfaces. Together, internal tides, lee waves and geothermal heat flux contribute about 10-11 Sv, therefore explaining only about half of the global lower overturning cell (e.g. Talley *et al.* (2003); Lumpkin & Speer (2007); Cessi (2019)).

Among the processes not included in this calculation, we have not considered the contribution of the far-field breaking internal tides and near-inertial waves. The far-field internal tides have been subject of extensive research in the recent years, and recently de Lavergne *et al.* (2019) presented a two-dimensional estimate of the full (i.e. near-field and far-field) internal tide-driven dissipation rate. While research is still needed to investigate how the different modes of internal waves dissipate throughout the water column, we are moving forward towards a global picture of the internal tide energy sinks. The contribution of near-inertial waves in the deep ocean is still unknown, mainly due to lack of knowledge of how their energy decays downward from the ocean surface. Here, we showed that their contribution could be important if they decay slowly, as suggested from mooring observations (Alford & Whitmont, 2007; Alford *et al.*, 2016). While more observations are needed to fill such knowledge gaps, high-resolution models, combined with discrete observations, might be used to quantify the importance of near-inertial waves for the global overturning circulation.

The other two research questions investigated in this thesis are reported together below, given that the same sets of tools have been used to address them.

Question 2 *How much mixing is there in the Atlantic Ocean and how does it affect the circulation of the upper overturning cell?* **Question 3** *How does mixing affect the*

distribution of tracers carried by the upper overturning cell?

We used both a compilation of observation-based estimates of diapycnal mixing (Chapter 4) and numerical simulations (Chapter 5) to quantify the effect of turbulent mixing on the closure of the upper overturning cell and the distribution of the tracers carried by the dense southward flowing waters. Both approaches returned a consistent picture: (i) diapycnal mixing contribution to the closure of the upper cell is negligible, but (ii) it can affect the distribution of the tracers carried southward by exchanging them between different water masses.

While the point (i) had already been widely discussed in literature (e.g. Gnanadesikan (1999); Wolfe & Cessi (2011); Marshall & Speer (2012); Nikurashin & Vallis (2012) and the recent review paper by Johnson *et al.* (2019) and references therein), here we provided a quantitative estimate of the mixing-driven water mass transformation rate in the Atlantic Ocean based on observations. In particular, this thesis has made a first attempt at combining and comparing different available estimates to draw a more complete picture of mixing in the Atlantic Ocean. We showed that different mixing estimates returned consistent vertical structure of mixing-driven water mass transformation in the ocean interior, despite the differences between the methods and the host of assumptions behind the inference of mixing from different sources. This result gives us confidence that we are on the verge of drawing a more accurate picture of diapycnal mixing. All the mixing estimates returned the largest water mass transformation rates across density surfaces within the dense southward flowing waters formed in the North Atlantic, while only 1-2 Sv of waters are transformed into lighter waters from the deeper southward to the shallower northward branches of the upper overturning cell, i.e. contributing to the closure of the upper cell.

The consistency in the picture drawn by the different estimates used here does not exclude the need of more observations, especially in the deep ocean and in the proximity of the ocean boundaries. The expansion of the Deep Argo float program (Jayne *et al.*, 2017) will likely play an important role in our understanding of mixing between 2000 m and

4000 m. Measurements in the proximity of the boundary are challenging and expensive, and so rarely performed, but are needed to investigate the contribution of boundary turbulence to the along-boundary upwelling of water masses and tracers (De Lavergne *et al.*, 2016; Ferrari *et al.*, 2016; McDougall & Ferrari, 2017). Measurements in the proximity of the boundary could also explain why the bulk estimate of diapycnal mixing returned overall larger values of mixing-driven water mass transformation compared to the localised mixing estimates. In the absence of enough observations, diapycnal mixing along the boundaries could be estimated from high resolution numerical simulations, which could provide a useful tool for the validation of this hypothesis, as well as for interpreting the observations and filling in the gaps between them.

As for the latter point (ii), diapycnal mixing is known to play an important role in the Indian and Pacific Oceans (e.g. Talley *et al.* (2011); Talley (2013)), but has been largely neglected in the Atlantic Ocean due to the secondary role it plays in the dynamics of the Atlantic overturning circulation, as discussed above. However, we have shown here that even within the Atlantic basin there is enough diapycnal mixing to affect the density classes in which tracers will upwell in the Southern Ocean, therefore determining where they will be distributed around Antarctica, and from there which pathways they will follow in the global overturning circulation. The observation-based estimates have been used to calculate a bulk diffusive length scale, which indicates the extent to which a tracer can potentially be moved in the vertical by mixing-induced up/downwelling. The diffusive length scale we found is of the order of hundreds to thousands of metres, indicating that mixing can potentially exchange tracers between different water masses.

The spatial variability of mixing should also be investigated in more detail, given that the patterns of diapycnal upwelling and downwelling are key in setting how tracers can be exchanged between different densities and depths. Among the different regions where the spatial variability of mixing could be explored more extensively in the near future, the North Atlantic basin would be an excellent starting point, considering that it is rel-

atively well sampled thanks to the RAPID (https://www.rapid.ac.uk/, see Smeed *et al.* (2015)), Line W (www.whoi.edu/science/PO/linew/), OSNAP (www.o-snap.org) and Argo programs (http://www.argo.ucsd.edu/), as well as from a larger number of hydrographics casts than in the other basins (see Kunze (2017*b*)). This observations, in combinations with tracer observations, such as chrolofluorocarbons (CFCs), could potentially be used to address the spatial variability of mixing and its co-variance with tracer distributions.

The importance of mixing is setting the tracer distribution has been confirmed in the numerical simulations performed in a quasi-realistic Atlantic domain analysed here. A tracer injected at the surface in the North Atlantic was shown to get entrained into the dense waters of the upper cell and mixed in the water column while carried southward. A larger fraction of the tracer ultimately ended up in the deep and abyssal ocean in the presence of high-mixing. About 40% of the tracer left the upper cell, and about 15% entered the northward branch of the lower cell. In comparison, 30% of the tracer left the upper cell in a low-mixing scenario, and only 8% entered the northward branch of the lower cell. We showed that in the presence of enhanced mixing, a larger fraction of the tracer upwelled closer to Antarctica and entered the lower cell, while less upwelled further north where it was carried northward via the intermediate waters of the upper cell. These differences have particularly important implications for the inter-hemispheric heat transport by the upper cell: the southward transport of anthropogenic heat that has been taken up in the North Atlantic is strongly dependent on the amount of mixing that the dense waters experience along their route to the Southern Ocean. Therefore, the way mixing is represented in climate models is going to play a role in future climate predictions.

This thesis provides a quantification of the impact of diapycnal mixing on the overturning circulation and its implications for the distribution of tracers carried by the overturning circulation's cells. We believe its findings have contributed to our understanding of the role of the global overturning circulation in the climate system, and will help our understanding of how the system is going to respond to anthropogenic climate change.

References

Adcroft, A., Scott, J. R. & Marotzke, J. 2001 Impact of geothermal heating on the global ocean circulation. *Geophysical Research Letters*, **28**(9), 1735–1738.

Alford, M. 2001 Internal swell generation: The spatial distribution of energy flux from the wind to mixed layer near-inertial motions. *Journal of Physical Oceanography*, **31**(8), 2359–2368.

Alford, M. 2003 Improved global maps and 54-year history of wind-work on ocean inertial motions. *Geophysical Research Letters*, **30**(8).

Alford, M., Girton, J., Voet, G., Carter, G., Mickett, J. & Klymak, J. 2013 Turbulent mixing and hydraulic control of abyssal water in the Samoan Passage. *Geophysical Research Letters*, **40**(17), 4668–4674.

Alford, M., MacKinnon, J. A., Simmons, H. L. & Nash, J. D. 2016 Near-inertial internal gravity waves in the ocean. *Annual review of marine science*, **8**, 95–123.

Alford, M. & Whitmont, M. 2007 Seasonal and spatial variability of near-inertial kinetic energy from historical moored velocity records. *Journal of Physical Oceanography*, **37**(8), 2022–2037.

Andrews, D. & McIntyre, M. E. 1976 Planetary waves in horizontal and vertical shear: The generalized Eliassen-Palm relation and the mean zonal acceleration. *Journal of the Atmospheric Sciences*, **33**(11), 2031–2048.

Armour, K. C., Marshall, J., Scott, J. R., Donohoe, A. & Newsom, E. R. 2016 Southern Ocean warming delayed by circumpolar upwelling and equatorward transport. *Nature Geoscience*, **9**(7), 549.

Bell, T. 1975 Lee waves in stratified flows with simple harmonic time dependence. *Journal of Fluid Mechanics*, **67**(4), 705–722.

Bouffard, D. & Boegman, L. 2013 A diapycnal diffusivity model for stratified environmental flows. *Dynamics of Atmospheres and Oceans*, **61**, 14–34.

Bower, A. S., Lozier, M. S., Gary, S. F. & Böning, C. W. 2009 Interior pathways of the North Atlantic Meridional Overturning Circulation. *Nature*, **459**(7244), 243.

Bryan, F. 1987 Parameter sensitivity of primitive equation ocean general circulation models. *Journal of Physical Oceanography*, **17**(7), 970–985.

Bryan, K. & Lewis, L. 1979 A water mass model of the world ocean. *Journal of Geophysical Research: Oceans*, **84**(C5), 2503–2517.

Bühler, O. & Holmes-Cerfon, M. 2011 Decay of an internal tide due to random topography in the ocean. *Journal of Fluid Mechanics*, **678**, 271–293.

Bullister, J., Rhein, M. & Mauritzen, C. 2013 *Ocean circulation and climate - a 21st century perspective, chapter 1*. Academic Press, Kidlington, U.K. Http://dx.doi.org/10.1016/B978-0-12-391851-2.00001-5.

Caulfield, C. & Peltier, W. 2000 The anatomy of the mixing transition in homogeneous and stratified free shear layers. *Journal of Fluid Mechanics*, **413**, 1–47.

Cessi, P. 2019 The global overturning circulation. *Annual review of marine science*, **11**, 249–270.

Crawford, G. & Large, W. 1996 A numerical investigation of resonant inertial response of the ocean to wind forcing. *Journal of Physical Oceanography*, **26**(6), 873–891.

D'Asaro, E. 1985 The energy flux from the wind to near-inertial motions in the mixed layer. *Journal of Physical Oceanography*, **15**, 943–959.

Davies, J. & Davies, D. 2010 Earth's surface heat flux. *Solid Earth*, **1**, 5–24.

de Boyer Montégut, C., Madec, G., Fischer, A. S., Lazar, A. & Iudicone, D. 2004 Mixed layer depth over the global ocean: An examination of profile data and a profile-based climatology. *Journal of Geophysical Research: Oceans*, **109**(C12).

de Lavergne, C., Falahat, S., Madec, G., Roquet, F., Nycander, J. & Vic, C. 2019 Toward global maps of internal tide energy sinks. *Ocean Modelling*, **137**, 52–75.

de Lavergne, C., Madec, G., Le Sommer, J., Nurser, G. & Naveira-Garabato, A. 2016 The impact of a variable mixing efficiency on the abyssal overturning. *Journal of Physical Oceanography*, **46**, 663–681.

De Lavergne, C., Madec, G., Le Sommer, J., Nurser, G. & Naveira Garabato, A. C. 2016 On the consumption of Antarctic Bottom water in the abyssal ocean. *Journal of Physical Oceanography*, **46**(2), 635–661.

Drazin, P. G. & Reid, W. H. 2004 *Hydrodynamic stability*. Cambridge University Press.

Egbert, G. & Ray, R. 2000 Significant dissipation of tidal energy in the deep ocean inferred from satellite altimeter data. *Nature*, **405**(6788), 775.

Egbert, G. D. & Ray, R. D. 2003 Semi-diurnal and diurnal tidal dissipation from TOPEX/-Poseidon altimetry. *Geophysical Research Letters*, **30**(17).

Emile-Geay, J. & Madec, G. 2009 Geothermal heating, diapycnal mixing and the abyssal circulation. *Ocean Science*, **5**(2), 203–217.

Ferrari, R., Mashayek, A., McDougall, T., Nikurashin, M. & Champin, J.-M. 2016 Turning ocean mixing upside down. *Journal of Physical Oceanography*, **46**, 2239–2261.

Fine, R. A. 2011 Observations of CFCs and SF6 as ocean tracers. *Annual Review of Marine Science*, **3**, 173–195.

Fox-Kemper, B., Ferrari, R. & Hallberg, R. 2008 Parameterization of mixed layer eddies. Part i: Theory and diagnosis. *Journal of Physical Oceanography*, **38**(6), 1145–1165.

Furuichi, N., Hibiya, T. & Niwa, Y. 2008 Model-predicted distribution of wind-induced internal wave energy in the world's oceans. *Journal of Geophysical Research: Oceans*, **113**(C9).

Ganachaud, A. 2003 Large-scale mass transport, water mass formation and diffusivities estimated from World Ocean Circulation Experiment (WOCE) hydrographic data. *Journal of Geophysical Research*, **108**, 3213.

Ganachaud, A. & Wunsch, C. 2000 Improved estimates of global ocean circulation, heat transport and mixing from hydrographic data. *Nature*, **408**, 453.

Garrett, C. & Kunze, E. 2007 Internal tide generation in the deep ocean. *Annual Review of Fluid Mechanics*, **39**, 57–87.

Garrett, C. & Munk, W. 1979 Internal waves in the ocean. *Annual review of Fluid Mechanics*, **11**(1), 339–369.

Gent, P. R. & McWilliams, J. C. 1990 Isopycnal mixing in ocean circulation models. *Journal of Physical Oceanography*, **20**(1), 150–155.

Gent, P. R., Willebrand, J., McDougall, T. J. & McWilliams, J. C. 1995 Parameterizing eddy-induced tracer transports in ocean circulation models. *Journal of Physical Oceanography*, **25**(4), 463–474.

Gnanadesikan, A. 1999 A simple predictive model for the structure of the oceanic pycnocline. *Science*, **208**, 2077–2079.

Green, J. & Nycander, J. 2013 A comparison of tidal conversion parameterizations for tidal models. *Journal of Physical Oceanography*, **43**, 104–119.

Gregg, M., D'Asaro, E., Riley, J. & Kunze, E. 2018 Mixing efficiency in the ocean. *Annual Review of Marine Science*, **10**, 443–473.

Griffies, S. M. 2012 Elements of the modular ocean model (MOM). *GFDL Ocean Group Technical Report*, **7**, 620.

Henyey, F., Wright, J. & Flatte, S. 1986 Energy and action flow through the internal wave field: An eikonal approach. *Journal of Geophysical Research*, **91**, 8487–8495.

Henyey, F. S. 1991 Scaling of internal wave model predictions for ϵ. In *Dynamics of oceanic internal gravity waves: Proc.'aha huliko'a hawaiian winter workshop*, pp. 233–236.

Hood, E., Sabine, C. & Sloyan, B. 2010 The GO-SHIP repeat hydrography manual: A collection of expert reports and guidelines. *IOCCP Report Number 14, ICPO Publication Series Number 134.* Available online at http://www.go-ship.org/HydroMan.html.

Huussen, T., Naveira-Garabato, A., Bryden, H. & McDonagh, E. 2012 Is the deep Indian Ocean MOC sustained by breaking internal waves? *Journal of Geophysical Research: Oceans*, **117**.

Ito, T. & Marshall, J. 2008 Control of lower-limb overturning circulation in the Southern Ocean by diapycnal mixing and mesoscale eddy transfer. *Journal of Physical Oceanography*, **38**(12), 2832–2845.

Jayne, S. & St Laurent, L. 2001 Parameterizing tidal dissipation over rough topography. *Geophysical Research Letters*, **28**, 811–814.

Jayne, S. R. 2009 The impact of abyssal mixing parameterizations in an ocean general circulation model. *Journal of Physical Oceanography*, **39**(7), 1756–1775.

Jayne, S. R., Roemmich, D., Zilberman, N., Riser, S. C., Johnson, K. S., Johnson, G. C. & Piotrowicz, S. R. 2017 The Argo program: present and future. *Oceanography*, **30**(2), 18–28.

Jochum, M., Briegleb, B. P., Danabasoglu, G., Large, W. G., Norton, N. J., Jayne, S. R., Alford, M. H. & Bryan, F. O. 2013 The impact of oceanic near-inertial waves on climate. *Journal of Climate*, **26**(9), 2833–2844.

Johns, W., Baringer, M., Beal, L., Cunningham, S., Kanzow, T., Bryden, H., Hirschi, J., Marotzke, J., Meinen, C. *et al.* 2011 Continuous, array-based estimates of Atlantic Ocean heat transport at 26.5°N. *Journal of Climate*, **24**, 2429–2449.

Johnson, H. L., Cessi, P., Marshall, D. P., Schloesser, F. & Spall, M. A. 2019 Recent contributions of theory to our understanding of the Atlantic Meridional Overturning Circulation. *Journal of Geophysical Research: Oceans*, **124**(8), 5376–5399.

Klaassen, G. & Peltier, W. 1985 The onset of turbulence in finite-amplitude Kelvin–Helmholtz billows. *Journal of Fluid Mechanics*, **155**, 1–35.

Kohler, J., Mertens, C., Walter, M., Stober, U., Rhein, M. & Kanzow, T. 2014 Variability in the internal wave field induced by the Atlantic Deep Western Boundary Current at 16°N. *Journal of Physical Oceanography*, **44**.

Koltermann, K. P., Gouretski, V. & Jancke, K. 2011 *Hydrographic atlas of the world ocean circulation experiment (WOCE). Volume 3: Atlantic Ocean*. National Oceanography Centre.

Kuhlbrodt, T., Griesel, A., Montoya, M., Levermann, A., Hofmann, M. & Rahmstorf, S. 2007 On the driving processes of the atlantic meridional overturning circulation. *Review of Geophysics*, **45**. Doi:10.1029/2004RG000166.

Kunze, E. 2017*a* The internal-wave-driven meridional overturning circulation. *Journal of Physical Oceanography*, **47**, 2673–2689.

Kunze, E. 2017*b* Internal-wave-driven mixing: Global geography and budgets. *Journal of Physical Oceanography*, **47**(6), 1325–1345.

Kunze, E., Firing, E., Hummon, J., Chereskin, T. & Thurnherr, A. 2006 Global abyssal mixing inferred from lowered ADCP shear and CTD strain profiles. *Journal of Physical Oceanography*, **36**, 1553–1576.

Large, W. G., McWilliams, J. C. & Doney, S. C. 1994 Oceanic vertical mixing: A review and a model with a non-local boundary layer parameterization. *Reviews of Geophysics*, **32**(4), 363–403.

Large, W. G. & Yeager, S. 2009 The global climatology of an inter-annually varying air-sea flux data set. *Climate dynamics*, **33**(2-3), 341–364.

Ledwell, J., Montgomery, E., Polzin, K., Laurent, L. S., Schmitt, R. & Toole, J. 2000 Evidence for enhanced mixing over rough topography in the abyssal ocean. *Nature*, **403**(6766), 179.

Ledwell, J. R., Watson, A. J. & Law, C. S. 1993 Evidence for slow mixing across the pycnocline from an open-ocean tracer-release experiment. *Nature*, **364**(6439), 701.

Lee, H.-C., Rosati, A. & Spelman, M. J. 2006 Barotropic tidal mixing effects in a coupled climate model: Oceanic conditions in the Northern Atlantic. *Ocean Modelling*, **11**(3-4), 464–477.

Lefauve, A., Muller, C. & Melet, A. 2015 A three-dimensional map of tidal dissipation over abyssal hills. *Journal of Geophysical Research: Oceans*, **120**(7), 4760–4777.

Lozier, M. S. 1997 Evidence for large-scale eddy-driven gyres in the North Atlantic. *Science*, **277**(5324), 361–364.

Lucas, D. & Caulfield, C.-c. P. 2017 Irreversible mixing by unstable periodic orbits in buoyancy dominated stratified turbulence. *Journal of Fluid Mechanics*, **832**.

Lumpkin, R. & Speer, K. 2007 Global ocean meridional overturning. *Journal of Physical Oceanography.*, **37**, 2550–2562.

MacKinnon, J. A., Zhao, Z., Whalen, C. B., Waterhouse, A. F., Trossman, D. S., Sun, O. M., St. Laurent, L. C., Simmons, H. L., Polzin, K. *et al.* 2017 Climate process team on internal wave–driven ocean mixing. *Bulletin of the American Meteorological Society*, **98**(11), 2429–2454.

Marotzke, J. 1997 Boundary mixing and the dynamics of three-dimensional thermohaline circulations. *Journal of Physical Oceanography*, **27**(8), 1713–1728.

Marshall, D. 1997 Subduction of water masses in an eddying ocean. *Journal of Marine Research*, **55**(2), 201–222.

Marshall, J., Armour, K. C., Scott, J. R., Kostov, Y., Hausmann, U., Ferreira, D., Shepherd, T. G. & Bitz, C. M. 2014 The ocean's role in polar climate change: asymmetric Arctic and Antarctic responses to greenhouse gas and ozone forcing. *Philosophical Transactions of the Royal Society A: Mathematical, Physical and Engineering Sciences*, **372**(2019), 20130 040.

Marshall, J. & Radko, T. 2003 Residual-mean solutions for the Antarctic Circumpolar Current and its associated overturning circulation. *Journal of Physical Oceanography*, **33**(11), 2341–2354.

Marshall, J. & Schott, F. 1999 Open-ocean convection: Observations, theory, and models. *Reviews of Geophysics*, **37**(1), 1–64.

Marshall, J. & Speer, K. 2012 Closure of the meridional overturning circulation through Southern Ocean upwelling. *Nature geoscience*, **5**, 171–180.

Mashayek, A., Caulfield, C. & Peltier, W. 2013*a* Time dependent, non-monotonic mixing in stratified turbulent shear flows: implications for oceanographic estimates of buoyancy flux. *Journal of Fluid Mechanics*, **736**, 570–593.

Mashayek, A., Caulfield, C. & Peltier, W. 2017*a* Role of overturns in optimal mixing in stratified mixing layers. *Journal of Fluid Mechanics*, **826**, 522–552.

Mashayek, A., Ferrari, R., Merrifield, S., Ledwell, J., St Laurent, L. & Naveira-Garabato, A. 2017*b* Topographic enhancement of vertical turbulent mixing in the Southern Ocean. *Nature Communications*, **8**.

Mashayek, A., Ferrari, R., Nikurashin, M. & Peltier, W. 2015 Influence of enhanced abyssal diapycnal mixing on stratification and the ocean overturning circulation. *Journal of Physical Oceanography*, **45**, 2580–2597.

Mashayek, A., Ferrari, R., Vettoretti, G. & Peltier, W. 2013*b* The role of the geothermal heat flux in driving the abyssal ocean circulation. *Geophysical Research Letters*, **40**(12), 3144–3149.

Mashayek, A. & Peltier, W. 2013 Shear induced mixing in geophysical flows: Does the route to turbulence matter to its efficiency? *Journal of Fluid Mechanics*, **725**, 216–261.

Mashayek, A., Salehipour, H., Bouffard, D., Caulfield, C., Ferrari, R., Nikurashin, M., Peltier, W. & Smyth, W. 2017*c* Efficiency of turbulent mixing in the abyssal ocean circulation. *Geophysical Research Letters*, **44**, 6296–6306.

McCarthy, G., Smeed, D., Johns, W. E., Frajka-Williams, E., Moat, B., Rayner, D., Baringer, M., Meinen, C., Collins, J. *et al.* 2015 Measuring the Atlantic Meridional Overturning Circulation at 26°N. *Progress in Oceanography*, **130**, 91–111.

McComas, C. H. & Müller, P. 1981 The dynamic balance of internal waves. *Journal of Physical Oceanography*, **11**(7), 970–986.

McDougall, T. & Ferrari, R. 2017 Abyssal upwelling and downwelling driven by near-boundary mixing. *Journal of Physical Oceanography*, **47**, 261–283. (doi:10.1175/JPO-D-16-0082.1)

Melet, A., Hallberg, R., Legg, S. & Polzin, K. 2013 Sensitivity of the ocean state to the vertical distribution of internal-tide-driven mixing. *Journal of Physical Oceanography*, **43**(3), 602–615.

Melet, A., Legg, S. & Hallberg, R. 2016 Climatic impacts of parameterized local and remote tidal mixing. *Journal of Climate*, **29**(10), 3473–3500.

Meredith, M. P., Woodworth, P. L., Chereskin, T. K., Marshall, D. P., Allison, L. C., Bigg, G. R., Donohue, K., Heywood, K. J., Hughes, C. W. *et al.* 2011 Sustained monitoring of the Southern Ocean at Drake Passage: Past achievements and future priorities. *Reviews of Geophysics*, **49**(4).

Monismith, S. G., Koseff, J. R. & White, B. L. 2018 Mixing efficiency in the presence of stratification: when is it constant? *Geophysical Research Letters*, **45**(11), 5627–5634.

Moum, J. N. 1996 Efficiency of mixing in the main thermocline. *Journal of Geophysical Research: Oceans*, **101**(C5), 12 057–12 069.

Munk, W. 1966 Abyssal recipes. *Deep-Sea Research*, **13**, 707–730.

Munk, W. & Wunsch, C. 1998 Abyssal recipes ii: energetics of tidal and wind mixing. *Deep Sea Research Part I: Oceanographic Research Papers*, **45**(12), 1977 – 2010.

Naveira-Garabato, A., Williams, A. & Bacon, S. 2014 The three-dimensional overturning circulation of the Southern Ocean during the WOCE era. *Progress in Oceanography*, **120**, 41–78.

Nikurashin, M. & Ferrari, R. 2010*a* Radiation and dissipation of internal waves generated

by geostrophic motions impinging on small-scale topography: Application to the Southern ocean. *Journal of Physical Oceanography*, **40**(9), 2025–2042.

Nikurashin, M. & Ferrari, R. 2010*b* Radiation and dissipation of internal waves generated by geostrophic motions impinging on small-scale topography: Theory. *Journal of Physical Oceanography*, **40**(5), 1055–1074.

Nikurashin, M. & Ferrari, R. 2011 Global energy conversion rate from geostrophic flows into internal lee waves in the deep ocean. *Geophysical Research Letters*, **38**(8).

Nikurashin, M. & Ferrari, R. 2013 Overturning circulation driven by breaking internal waves in the deep ocean. *Geophysical Research Letters*, **40**, 3133–3137.

Nikurashin, M. & Legg, S. 2011 A mechanism for local dissipation of internal tides generated at rough topography. *Journal of Physical Oceanography*, **41**(2), 378–395.

Nikurashin, M. & Vallis, G. 2011 A theory of deep stratification and overturning circulation in the ocean. *Journal of Physical Oceanography*, **41**(3), 485–502.

Nikurashin, M. & Vallis, G. 2012 A theory of the interhemispheric meridional overturning circulation and associated stratification. *Journal of Physical Oceanography*, **42**(10), 1652–1667.

Nycander, J. 2005 Generation of internal waves in the deep ocean by tides. *Journal of Geophysical Research: Oceans*, **110**(C10).

Osborn, T. 1980 Estimates of the local-rate of vertical diffusion from dissipation measurements. *Journal of Physical Oceanography*, **10**, 83–89.

Peltier, W. & Caulfield, C. 2003 Mixing efficiency in stratified shear flows. *Annual review of fluid mechanics*, **35**(1), 135–167.

Polzin, K., Naveira-Garabato, A., Huussen, T., Sloyan, B. & Waterman, S. 2014 Finescale parameterizations of turbulent dissipation. *Journal of Geophysical Research*, **119**, 1383–1419.

Polzin, K., Toole, J., Ledwell, J. & Schmitt, R. 1997 Spatial variability of turbulent mixing in the abyssal ocean. *Science*, **276**(5309), 93–96.

Polzin, K. L., Toole, J. M. & Schmitt, R. W. 1995 Finescale parameterizations of turbulent dissipation. *Journal of physical oceanography*, **25**(3), 306–328.

Reid, J. L. 1994 On the total geostrophic circulation of the North Atlantic ocean: Flow patterns, tracers, and transports. *Progress in Oceanography*, **33**(1), 1–92.

Rhein, M. 1994 The deep western boundary current: tracers and velocities. *Deep Sea Research Part I: Oceanographic Research Papers*, **41**(2), 263–281.

Rintoul, S. R. 2018 The global influence of localized dynamics in the Southern Ocean. *Nature*, **558**(7709), 209–218.

Ruddick, B., Walsh, D. & Oakey, N. 1997 Variations in apparent mixing efficiency in the North Atlantic central water. *Journal of Physical Oceanography*, **27**(12), 2589–2605.

Salehipour, H. & Peltier, W. 2015 Diapycnal diffusivity, turbulent Prandtl number and mixing efficiency in Boussinesq stratified turbulence. *Journal of Fluid Mechanics*, **775**, 464–500.

Salehipour, H., Peltier, W. & Mashayek, A. 2015 Turbulent diapycnal mixing in stratified shear flows: the influence of Prandtl number on mixing efficiency and transition at high Reynolds number. *Journal of Fluid Mechanics*, **773**, 178–223.

Salehipour, H., Peltier, W., Whalen, C. & MacKinnon, J. 2016 A new characterization of the turbulent diapycnal diffusivities of mass and momentum in the ocean. *Geophysical Research Letters*, **43**(7), 3370–3379.

Sandstrom, H. & Elliott, J. 1984 Internal tide and solitons on the Scotian Shelf: A nutrient pump at work. *Journal of Geophysical Research: Oceans*, **89**(C4), 6415–6426.

Santoso, A., England, M. & Hirst, A. 2006 Circumpolar deep water circulation and variability in a coupled climate model. *Journal of Physical Oceanography*, **36**, 1523–1552.

Scott, J. R. & Marotzke, J. 2002 The location of diapycnal mixing and the meridional overturning circulation. *Journal of Physical Oceanography*, **32**(12), 3578–3595.

Scott, J. R., Marotzke, J. & Adcroft, A. 2001 Geothermal heating and its influence on the meridional overturning circulation. *Journal of Geophysical Research: Oceans*, **106**(C12), 31 141–31 154.

Scott, R. B., Goff, J. A., Naveira Garabato, A. & Nurser, A. 2011 Global rate and spectral characteristics of internal gravity wave generation by geostrophic flow over topography. *Journal of Geophysical Research: Oceans*, **116**(C9).

Sheen, K. L., Brearley, J. A., Naveira Garabato, A. C., Smeed, D. A., Waterman, S., Ledwell, J. R., Meredith, M. P., St. Laurent, L., Thurnherr, A. M. *et al.* 2013 Rates and mechanisms of turbulent dissipation and mixing in the Southern Ocean: Results from the Diapycnal and Isopycnal Mixing Experiment in the Southern Ocean (DIMES). *Journal of Geophysical Research: Oceans*, **118**(6), 2774–2792.

Shih, L. H., Koseff, J. R., Ivey, G. N. & Ferziger, J. H. 2005 Parameterization of turbulent fluxes and scales using homogeneous sheared stably stratified turbulence simulations. *Journal of Fluid Mechanics*, **525**, 193–214.

Simmons, H. L., Jayne, S. R., St Laurent, L. C. & Weaver, A. J. 2004 Tidally driven mixing in a numerical model of the ocean general circulation. *Ocean Modelling*, **6**(3-4), 245–263.

Sloyan, B. & Rintoul, S. 2001 The southern ocean limb of the global deep overturning circulation. *Journal of Physical Oceanography*, **31**, 143–173.

Smeed, D., McCarthy, G., Cunningham, S., Frajka-Williams, E., Rayner, D., Johns, W., Meinen, C., Baringer, M., Moat, B. *et al.* 2014 Observed decline of the Atlantic meridional overturning circulation 2004-2012. *Ocean Science*, **10**(1), 29–38.

Smeed, D., McCarthy, G., Rayner, D., Moat, B., Johns, W., Baringer, M. & Meinen, C. 2015 Atlantic meridional overturning circulation observed by the RAPID-MOCHA-WBTS (RAPID-Meridional Overturning Circulation and heatflux array-western boundary time series) array at 26°N from 2004 to 2015. *British Oceanographic Data Centre - Natural Environment Research Council, UK.*

Smith, K. S. 2007 The geography of linear baroclinic instability in Earth's oceans. *Journal of Marine Research*, **65**(5), 655–683.

Smyth, W. & Caldwell, D. 2001 The efficiency of mixing in turbulent patches: Inferences from direct simulations and microstructure observations. *Journal of Physical Oceanography*, **31**, 1969–1992.

Snow, K., Hogg, A. M., Downes, S. M., Sloyan, B. M., Bates, M. L. & Griffies, S. M. 2015 Sensitivity of abyssal water masses to overflow parameterisations. *Ocean Modelling*, **89**, 84–103.

Snow, K., Hogg, A. M., Sloyan, B. M. & Downes, S. M. 2016 Sensitivity of Antarctic Bottom Water to changes in surface buoyancy fluxes. *Journal of Climate*, **29**(1), 313–330.

St Laurent, L. C. & Garrett, C. 2002 The role of internal tides in mixing the deep ocean. *Journal of Physical Oceanography*, **32**(10), 2882–2899.

St Laurent, L. C. & Schmitt, R. W. 1999 The contribution of salt fingers to vertical mixing in the North Atlantic tracer release experiment. *Journal of Physical Oceanography*, **29**(7), 1404–1424.

St Laurent, L. C. & Simmons, H. 2006 Estimates of power consumed by mixing in the ocean interior. *Journal of climate*, **19**(19), 4877–4890.

St Laurent, L. C., Simmons, H. & Jayne, S. 2002 Estimating tidally driven mixing in the deep ocean. *Geophysical Research Letters*, **29**.

St Laurent, L. C., Toole, J. M. & Schmitt, R. W. 2001 Buoyancy forcing by turbulence above rough topography in the abyssal Brazil Basin. *Journal of Physical Oceanography*, **31**(12), 3476–3495.

St Laurent, L. C. S. & Nash, J. D. 2004 An examination of the radiative and dissipative properties of deep ocean internal tides. *Deep Sea Research Part II: Topical Studies in Oceanography*, **51**(25-26), 3029–3042.

Stephens, J. C. & Marshall, D. P. 2000 Dynamical pathways of Antarctic Bottom Water in the Atlantic. *Journal of Physical Oceanography*, **30**(3), 622–640.

Stevens, D. P. & Killworth, P. D. 1992 The distribution of kinetic energy in the Southern Ocean: a comparison between observations and an eddy resolving general circulation model. *Philosophical Transactions of the Royal Society of London. Series B: Biological Sciences*, **338**(1285), 251–257.

Stober, U., Walter, M., Mertens, C. & Rhein, M. 2008 Mixing estimates from hydrographic measurements in the deep western boundary current of the North Atlantic. *Deep Sea Research Part I: Oceanographic Research Papers*, **55**, 721–736.

Stocker, T. 2013 *Ocean circulation and climate - a 21st century perspective, chapter*

1. Academic Press, Kidlington, U.K. Http://dx.doi.org/10.1016/B978-0-12-391851-2.00001-5.

Talley, L. D. 2003 Shallow, intermediate, and deep overturning components of the global heat budget. *Journal of Physical Oceanography*, **33**, 530–560.

Talley, L. D. 2013 Closure of the Global Overturning Circulation trough the Indian, Pacific, and Southern Oceans. *Oceanography*, **26**, 80–97.

Talley, L. D., Pickard, G. L., Emery, W. J. & Swift, J. H. 2011 *Descriptive physical oceanography*. Kidlington, U.K.: Academic Press.

Talley, L. D., Reid, J. L. & Robbins, P. E. 2003 Data-based meridional overturning streamfunctions for the global ocean. *Journal of Climate*, **16**(19), 3213–3226.

Thorpe, S. 2007 *An introduction to ocean turbulence*. Cambridge University Press.

Toggweiler, J. & Samuels, B. 1998 On the ocean's large-scale circulation near the limit of no vertical mixing. *Journal of Physical Oceanography*, **28**, 1832–1852.

Toole, J. M., Schmitt, R. W. & Polzin, K. L. 1994 Estimates of diapycnal mixing in the abyssal ocean. *Science*, **264**(5162), 1120–1123.

Van Haren, H. 2018 *High-resolution observations of internal wave turbulence in the deep ocean*. Springer Oceanography. Springer, Cham. In: Velarde M., Tarakanov R., Marchenko A. (eds) The Ocean in Motion.

Van Haren, H., Berndt, C. & Klaucke, I. 2017 Ocean mixing in deep-sea trenches: New insights from the challenger deep, mariana trench. *Deep-Sea Research*, **129**, 1–9.

Vic, C., Garabato, Naveira-Garabato, A., Green, M., Waterhouse, A. F., Zhao, Z., Melet, A., de Lavergne, C., Buijsman, M. C. & Stephenson, G. R. 2019 Deep-ocean mixing driven by small-scale internal tides. *Nature communications*, **10**.

Vic, C., Naveira Garabato, A. C., Green, J. M., Spingys, C., Forryan, A., Zhao, Z. & Sharples, J. 2018 The lifecycle of semidiurnal internal tides over the northern Mid-Atlantic Ridge. *Journal of Physical Oceanography*, **48**(1), 61–80.

Voet, G., Girton, G., Alford, M., Carter, G., Klymak, J. & Mickett, J. 2015 Pathways, volume transport, and mixing of abyssal water in the Samoan Passage. *Journal of Physical Oceanography*, **45**, 562–588.

Waterhouse, A., MacKinnon, J., Nash, J., Alford, M., Kunze, E., Simmons, H., Polzin, K., St Laurent, L., Sun, O. *et al.* 2014 Global patterns of diapycnal mixing from measurements of the turbulent dissipation rate. *Journal of Physical Oceanography*, **44**, 1854–1872.

Welander, P. 1971 A discussion on ocean currents and their dynamics-the thermocline problem. *Philosophical Transactions of the Royal Society of London. Series A, Mathematical and Physical Sciences*, **270**(1206), 415–421.

Whalen, C., MacKinnon, J. & Talley, L. 2018 Large-scale impacts of the mesoscale environment on mixing from wind-driven internal waves. *Nature Geoscience*, **11**(11), 842.

Whalen, C., MacKinnon, J., Talley, L. & Waterhouse, A. 2015 Estimating the mean diapycnal mixing using a finescale strain parameterization. *Journal of Physical Oceanography*, **45**, 1174–1188.

Whalen, C., Talley, L. & MacKinnon, J. 2012 Spatial and temporal variability of global ocean mixing inferred from Argo profiles. *Geophysical Research Letters*, **39**. L18612, doi:10.1029/2012GL053196.

Williams, R. & Follows, M. 2011 *Ocean dynamics and the carbon cycle*. Cambridge University Press, Cambridge, U.K.

Winters, K. B., Lombard, P. N., Riley, J. J. & D'Asaro, E. A. 1995 Available potential energy and mixing in density-stratified fluids. *Journal of Fluid Mechanics*, **289**, 115–128.

Winton, M. 2000 A reformulated three-layer sea ice model. *Journal of atmospheric and oceanic technology*, **17**(4), 525–531.

Wolfe, C. & Cessi, P. 2011 The adiabatic pole-to-pole overturning circulation. *Journal of Physical Oceanography*, **41**, 1795–1810.

Wolfe, C. L. & Cessi, P. 2010 What sets the strength of the mid-depth stratification and overturning circulation in eddying ocean models? *Journal of Physical Oceanography*, **40**(7), 1520–1538.

Wunsch, C. & Ferrari, R. 2004 Vertical mixing, energy, and the general circulation of the oceans. *Annual Review of Fluid Mechanics*, **36**, 281–314.

Zhao, Z., Alford, M. H., Girton, J. B., Rainville, L. & Simmons, H. L. 2016 Global observations of open-ocean mode-1 M2 internal tides. *Journal of Physical Oceanography*, **46**(6), 1657–1684.

Zheng, K. & Nikurashin, M. 2019 Downstream propagation and remote dissipation of internal waves in the Southern Ocean. *Journal of Physical Oceanography*, **49**(7), 1873–1887.